EPFL

Infrared nanoplasmonic metasurfaces augmented by artificial intelligence for universal biosensing

Aurélian Michel JOHN-HERPIN

■ École
polytechnique
fédérale
de Lausanne

2022

Acknowledgments

Abstract

Nanoplasmonic metasurfaces have shown outstanding light-matter interaction enhancement capabilities, leading to their emergence as powerful platforms for highly sensitive biospectroscopy. Metasurface-enhanced biospectroscopy offers unprecedented opportunities for biological studies, and its full potential remains to be unleashed. Mid-IR metasurfaces, in particular, are very promising because they can act as amplifiers of fingerprint-like molecule vibrations, which are plentiful in this rich spectral range. In this thesis, we develop novel nanoplasmonic designs coupled with custom microfluidics and artificial intelligence-based data analysis models to demonstrate real-time, label-free, chemically specific, and non-destructive monitoring of biomolecules and their interactions in aqueous media. Our first nanoplasmonic design combines optimized grating order-coupled nanoantenna arrays with protein-accessible nanogaps to enable the high sensitivity monitoring of proteins and their three-dimensional structures in aqueous media. The engineered nanoantennas reach electric field intensity enhancements of up to five orders of magnitude and provide chemically specific detection of proteins and their secondary structures down to picograms and nanograms per milliliter, respectively.

In the next part of the thesis, we develop multiresonant metasurfaces to monitor interactions between biomolecules with vibrational fingerprints in different parts of the mid-IR range. Our first effort focuses on developing a nanoplasmonic design for simultaneous monitoring of both proteins and lipid molecules. Lipids are another important class of biomolecules as they are the building blocks of biological membranes, and lipid-protein interactions are at the core of many cellular processes. New analytical tools for their study in water and at the monolayer level are of fundamental importance. Therefore, we introduce a dual-resonant nanoplasmonic design coupled to machine learning-based data analysis to overcome current sensor challenges. We apply our technology to a dynamic system involving synaptic vesicle mimics and demonstrate that we can resolve complex mass-preserving biological interactions in real-time. This is a remarkable feat that traditional non-chemically specific analytical measurement tools such as surface plasmon resonance or quartz crystal microbalance spectroscopy could not achieve. In the final part of the thesis, we develop yet another multiresonant design for broadband coverage of the whole mid-IR range. We couple our sensor to a deep learning model to resolve a dynamic biological system including all major classes of biomolecules simultaneously. Specifically, we resolve the toxic peptide-induced release of carbohydrates and nucleotides from exosome-like bionanoparticles.

Keywords

Résumé

Les métasurfaces nanoplasmoniques ont montré des capacités exceptionnelles d'exaltation des interactions rayonnement-matière, conduisant à leur émergence en tant que plateformes puissantes pour la biospectroscopie hautement sensible. La biospectroscopie exaltée par métasurface offre des opportunités sans précédent pour les études biologiques, et son plein potentiel reste à être exploité. Les métasurfaces infrarouge moyen, en particulier, sont très prometteuses car elles peuvent agir comme des amplificateurs de vibrations moléculaires qui sont semblables à des empreintes digitales et abondantes dans cette riche gamme spectrale. Dans cette thèse, nous développons de nouvelles métasurfaces nanoplasmoniques que nous intégrons dans des dispositifs microfluidiques conçus sur mesure et que nous couplons à des modèles d'analyse de données, basés sur l'intelligence artificielle. Cela nous permet de démontrer la capacité de nos capteurs à faire des mesures en temps réel, sans étiquette, chimiquement spécifiques et non destructrices des biomolécules et de leurs interactions en milieux aqueux. Notre première conception de métasurface nanoplasmonique est basée sur des réseaux optimisés de nanoantennes couplées par ordre de réseau et ayant des intervalles nanométriques accessibles aux protéines pour permettre la mesure de leur présence ainsi que de leurs structures tridimensionnelles avec haute sensibilité en milieux aqueux. Les nanoantennes conçues atteignent des exaltations d'intensité de champ électrique allant jusqu'à cinq ordres de grandeur et permettent une détection chimiquement spécifique des protéines et de leurs structures secondaires à des concentrations faibles de l'ordre de picogrammes et de nanogrammes par millilitre.

Dans la seconde partie de la thèse, nous développons des métasurfaces multirésonnantes pour suivre les interactions entre les biomolécules avec des empreintes vibratoires dans différentes bandes de la gamme de l'infrarouge moyen. Notre premier effort se concentre sur le développement d'une métasurface nanoplasmonique pour la mesure simultanée des protéines et des molécules lipidiques. Les lipides sont une autre classe importante de biomolécules qui sont les éléments constitutifs des membranes biologiques, et les interactions lipides-protéines sont au cœur de nombreux processus cellulaires. De nouveaux outils analytiques pour leur étude en milieux aqueux et de l'ordre de monocouches sont d'une importance fondamentale. Par conséquent, nous introduisons une métasurface nanoplasmonique à double résonance couplée à une analyse de données basée sur l'apprentissage automatique pour surmonter certaines limitations des capteurs actuels. Nous appliquons notre technologie à un système biomoléculaire dynamique composé de bionanoparticules similaires à des vésicules synaptiques, et démontrons que nous pouvons résoudre en temps réel des interactions biologiques complexes préservant la masse. Il s'agit, de fait, d'un exploit remarquable que les outils de mesure analytiques traditionnels

chimiquement non spécifiques, tels que la spectroscopie par résonance plasmonique de surface ou par microbalance à quartz, ne sont pas en mesure de réaliser. Dans la dernière partie de la thèse, nous développons un autre type de métasurface multirésonnantes pour la couverture à large bande de toute la gamme de l'infrarouge moyen. Nous couplons notre capteur à un modèle de l'intelligence artificielle basé sur l'apprentissage profond pour résoudre un système biologique dynamique incluant simultanément toutes les grandes classes de biomolécules. Plus précisément, nous résolvons la fuite de glucides et de nucléotides de bionanoparticules similaires à des exosomes perforées par des peptides toxiques.

Mots-clés

biocapteurs, apprentissage profond, spectroscopie infrarouge, métasurfaces, plasmonique, intelligence artificielle, photonique, nanotechnologies

Zusammenfassung

Nanoplasmonische Metaoberflächen zeigen herausragende Fähigkeiten zur Verstärkung von Licht-Materie-Wechselwirkung, weshalb sie sich als leistungsstarke Plattformen für hochempfindliche Biospektroskopie erweisen. Die Metaoberflächen-verstärkte Biospektroskopie bietet beispiellose Möglichkeiten für biologische Studien, wobei ihr volles Potenzial noch ausgeschöpft werden muss. Metaoberflächen im Mittelinfraroten sind besonders vielversprechend, da sie als Verstärker von fingerabdruckähnlichen molekularen Vibrationsbanden fungieren können, die in diesem Spektralbereich reichlich vorhanden sind. In dieser Doktorarbeit entwickeln wir neuartige nanoplasmonische Designs in Verbindung mit speziell angefertigten mikrofluidichen Zellen und auf künstlicher Intelligenz basierenden Datenanalysemodellen. Damit können markierungsfreie, chemisch-spezifische und zerstörungsfreie Echtzeitmessungen von Biomolekülen und ihren Wechselwirkungen in wässrigen Medien durchgeführt werden. Das erste nanoplasmonische Design kombiniert Verstärkungseffekte aus optimierter Gitterkopplung von Nanoantennen-Arrays mit nanometergroßen Antennenzwischenräume, die für Proteine zugänglich sind. Damit werden hochempfindliche Messungen von Proteinen und ihrer dreidimensionalen Strukturen in wässrigen Medien ermöglicht. Die nanofabrizierten Antennen erreichen dabei eine Verstärkung der elektrischen Feldstärke von bis zu fünf Größenordnungen und erlauben eine chemisch-spezifische Detektion von Proteinen und ihren Sekundärstrukturen bis zu Konzentrationen im Pikogramm bzw. Nanogramm pro Milliliter Bereich.

Im nächsten Teil der Doktorarbeit entwickeln wir multiresonante Metaoberflächen, um Wechselwirkungen zwischen Biomolekülen mit charakteristischen molekularen Vibrationsbanden in verschiedenen Teilen des Mittelinfraroten zu überwachen. In erster Linie konzentrieren wir uns auf die Entwicklung eines nanoplasmonischen Designs zur gleichzeitigen Überwachung von Proteinen und Lipidmolekülen. Lipide sind eine weitere wichtige Klasse von Biomolekülen, da sie die Bausteine biologischer Membranen sind und Lipid-Protein-Wechselwirkungen den Kern vieler zellulärer Prozesse bilden. Neue analytische Messmethoden für solche Wechselwirkungen in Wasser und auf Monolagen-Größenordnung sind von grundlegender Bedeutung. Daher stellen wir ein dual-resonantes nanoplasmonisches Design in Verbindung mit einer auf maschinellem Lernen basierenden Datenanalyse vor, um aktuelle Herausforderungen von biomolekularen Sensoren zu überwinden. Als Demonstration wenden wir unsere Technologie auf ein dynamisches biologisches System mit synaptischen Vesikel-ähnlichen Bionanopartikeln an und zeigen, dass wir komplexe masseerhaltende biologische Wechselwirkungen in Echtzeit auflösen können. Dies ist eine bemerkenswerte Leistung, die für herkömmliche, nicht chemisch-spezifische analytische Messinstrumente wie Oberflächenplasmonenresonanz- oder Quarzkristall-Mikrowaagenspektroskopie nicht möglich ist. Im letzten Teil der Arbeit entwickeln wir ein weiteres multiresonantes Design für die breitbandige Abdeckung des Mittelinfraroten. Wir koppeln unseren Sensor an ein Deep-Learning-Modell, um ein dynamisches biologisches System zu detektieren, das alle wichtigen Klassen von Biomolekülen gleichzeitig umfasst. Insbesondere detektieren wir die Freisetzung von Kohlenhydraten und Nukleotiden aus exosomartigen Bionanopartikeln durch die Wirkung eines toxischen Peptides.

Schlagwörter

Biosensorik, Deep Learning, Infrarotspektroskopie, Metaoberflächen, Plasmonik, Künstliche Intelligenz, Photonik, Nanotechnologie

Contents

List of Figures

List of Tables

List of Equations

Thesis Overview

Our understanding of health and disease is still very limited due to the incredible complexity of biology involving a myriad of biomolecules and interactions. The ability to expand our understanding crucially depends on the availability and capability of analytical measurement tools. This thesis introduces a new and universal nanophotonic platform for resolving complex biomolecular processes in a real-time, non-destructive, label-free, and chemically specific way using infrared spectroscopy.

Chapters 1 to 3 are introductory chapters providing the basics of the fields from the multiple scientific domains featured in this thesis, including biochemistry, data science, biotechnology, physics, spectroscopy, plasmonics, and photonics. In chapter 1, we give an overview of the biomolecular world and its building blocks. In chapter 2, we discuss the importance of biomolecule sensing and the principles and methods for doing so. Chapter 3 focuses on mid-IR spectroscopy methods and, in particular, surface-enhanced IR absorption (SEIRA) spectroscopy with plasmonic metasurfaces.

After discussing the outstanding potential of SEIRA with plasmonic metasurfaces for biomolecule sensing in the introduction, in chapter 4, we focus on developing a plasmonic design with optimized sensing performance to target proteins. We introduce novel plasmonic sensors based on grating order-coupled nanogap (GONG) arrays that combine design principles from the state-of-the-art of the SEIRA field to achieve an optimized sensing performance. The sensors are incorporated into custom microfluidic devices to quantify their excellent sensitivity to proteins and their three-dimensional structures in real-time. Furthermore, we show that the GONG design is flexible and can easily be adapted for monitoring other biologically relevant analytes such as liposomes.

Sensors optimized for detecting a single analyte type, such as proteins or lipids, are not optimal to study biological interactions between different classes of biomolecules. It is therefore also helpful to develop sensors able to detect different analyte types simultaneously. Consequently, in chapter 5, we present a new plasmonic sensor design based on self-similar nanoantenna arrays to enable the simultaneous detection of proteins and lipids. We demonstrate its capability to resolve mass-preserving biological processes in real-time between cytolytic peptides and lipid vesicles such as synaptic vesicle mimics. This achievement represents a significant milestone for studying interactions between proteins and biological membranes and is realized by coupling the multiresonant metasurface with machine learning-based data analysis.

Biomolecular interactions featured in physiology and pathology are, of course, not only limited to protein-lipid interactions, as complex processes often involve numerous other biomolecules at the same time. Consequently, in chapter 6, we further push the number of bio-analytes that can be detected simultaneously to include all major biomolecule classes by upgrading from a dual-resonant infrared metasurface to a triple-resonant one, and by incorporating deep learning into our data analysis approach. The metasurface we introduce in this chapter is a multiresonant version of the highly sensitive single-resonant design introduced in chapter 4. We use exosome-like vesicular bionanoparticles to demonstrate the ability of our sensor to resolve complex biological processes between all four major classes of biomolecules.

Finally, in chapter 7, a summary and discussion of the results of this work are given, pointing out limitations and how those could be addressed in the future. An outlook describes the potential applications of the technologies developed in this thesis.

Chapter 1   The Biomolecular World

1.1   The Biological Building Blocks

The realm of biomolecules is a fascinating world involving a myriad of agents interacting in various ways to define life, from health to disease. Despite the richness in diversity and complexity, the building blocks of life can be reduced to four major classes of biomolecules: proteins, nucleic acids, lipids, and carbohydrates.[1] These building blocks give rise to complex biological entities, e.g., glycoproteins, ribosomes, viruses, etc. Glycoproteins are proteins covalently linked to carbohydrates; these mixed agents can have various roles, such as recognition elements on the surface of cells to interact with other cells, e.g., T cells from the immune system.[2] Ribosomes are a more complex example of mixed biomolecule classes, they are bio-macromolecular nanomachines which perform protein synthesis in cells. Ribosomes are nucleoprotein complexes, i.e., proteins structurally associated with nucleic acids.[3] Viruses are another interesting example of complex biological entities. Glycoproteins are featured in their viral coats, and their cores are filled with nucleic acids containing the viral genome used for replication. Some viruses, such as SARS-CoV-2, have a viral envelope made from a lipid bilayer.[4] Viruses are thus complex biological entities, which can feature all four classes of biomolecules in their makeup. In the following subsections, a non-exhaustive overview of the four classes of biomolecules is given.

1.1.1   Proteins

Proteins are nanostructures and nanomachines that come in all sizes and shapes to carry out a plethora of functions. Proteins are constituted from twenty common amino acids, which are molecules each containing an amino and a carboxylate group, as well as a side chain unique to each of them (Figure 1:1a). The side chain can convey specific characteristics such as hydrophilicity, hydrophobicity, or electrical charge. The amino group of one amino acid and the carboxylate group of another are linked together to form a peptide bond, and together, the chain of linked amino acids forms a linear polypeptide (Figure 1:1a). Proteins acquire their functions once the linear polypeptide is folded into a specific three-dimensional shape called conformation. While proteins have unique conformations, they feature common structural elements called secondary structure motifs, including α-helices, β-sheets, turns, and loops (Figure 1:1b). Multiple distinct polypeptides can also be bound together to form a single protein with a complex functional structure.[1]
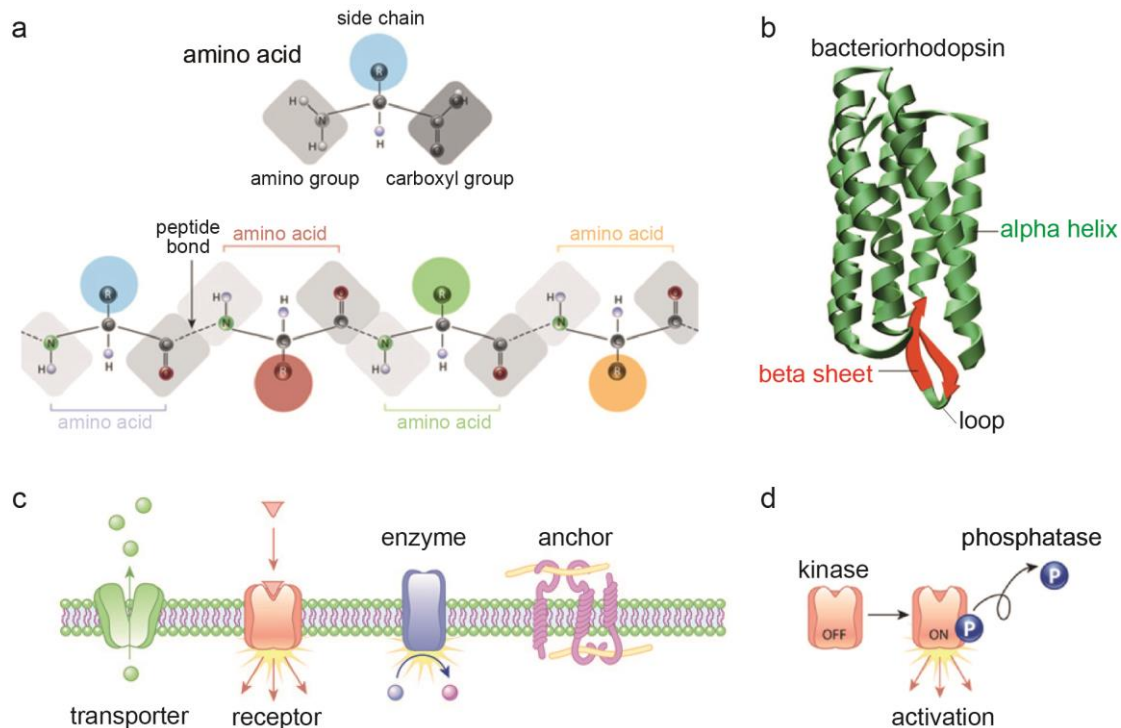
Figure 1:1 Proteins, polypeptides, and amino acids a) Schematic depiction of an amino acid and a polypeptide arising from the linking of amino acids via peptide bonds. b) Ribbon representation of the protein bacteriorhodopsin featuring alpha helices (green), beta-strands forming a beta-sheet (red), loops, and turns. c) Examples of transmembrane proteins with different functions. d) Kinase enzyme activated by phosphorylation via a phosphatase enzyme. Adapted from Ref.[5] Copyright 2010, Nature Education.

A common category of proteins are enzymes, i.e., biological catalysts, which accelerate the conversion of reaction substrates to product molecules (Figure 1:1c,d). Many of these enzymes feature a substrate-binding cleft, or groove, where the chemical reaction site, i.e., the active site of an enzyme, is located. Other proteins are structural components such as the cytoskeleton of cells, which are protein filaments interlinking to form a dynamic network.[6] Some proteins are hydrophilic and soluble in the cytosol of cells, while others have lipophilic parts to make them more soluble within the membrane of cells. Proteins spanning the entirety of a cell membrane are called transmembrane proteins, and they can be either alpha-helical or beta-barrel types.[7,8] Transmembrane proteins can form channels for molecules to be transported in and out of a cell, with the process usually involving conformational changes (Figure 1:1c).

Conformational changes are elemental to many physiological processes; however, they are also involved in pathological processes such as neurodegeneration, where proteins often become misfolded and aggregate to give rise to large inclusion bodies in the brain. Correct protein folding, as well as repairing and removal of misfolded proteins, is thus crucial for maintaining proper cellular and physiological function. These tasks are carried out by chaperones, which are proteins themselves. Chaperones assist with folding, unfolding, refolding, repairing, clearance, and prevention of aggregate formation.[9] The clearance process is initiated in the case of irreparable damage or excessive aggregate

accumulation, e.g., by tagging with ubiquitin for recognition and breakdown by proteasomes, i.e., large, multi-protein complexes which degrade proteins by breaking down their peptide bonds.[10,11]

The tagging with the small ubiquitin protein, i.e., ubiquitination, is only one of the multiple possible post-translational modifications (PTMs) of proteins used to regulate cellular processes.[12] For example, acetylation is the addition of an acetyl group, which has a considerable impact on gene expression and metabolism. It is also used in some pharmaceuticals like acetylsalicylic acid (aspirin) to enable the crossing of the blood-brain barrier.[13] Other examples of PTMs are methylation and phosphorylation, i.e., the addition of a methyl or phosphoryl group, respectively; these represent major biochemical processes for modifying protein function. The latter is considered the most abundant PTM in eukaryotes, with many enzymes' activity regulated by conformational change-inducing phosphorylation and dephosphorylation (Figure 1:1d).[14] Some PTMs like phosphorylation can also become dysregulated and lead to hyperphosphorylation of proteins such as Tau, which causes its misfolding and aggregation, which plays a role in Alzheimer's disease.[15]

1.1.2   Carbohydrates

From the perspective of mass, carbohydrates are the most abundant biomolecules on Earth. This group of biomolecules includes simple sugars and their polymers, i.e., mono- and polysaccharides, respectively (Figure 1:2a). All feature several hydroxyl groups, and most of them have either five or six carbon atoms forming their rings, with glucose being the most abundant six-carbon sugar.[1]

Carbohydrates act as energy carrier molecules, which can be ingested to release adenosine triphosphate (ATP) from the oxidation of glucose molecules. ATP is the energy currency of the cell and is used for metabolic processes. The main storage form of glucose in the body is glycogen, a multibranched polysaccharide of glucose.
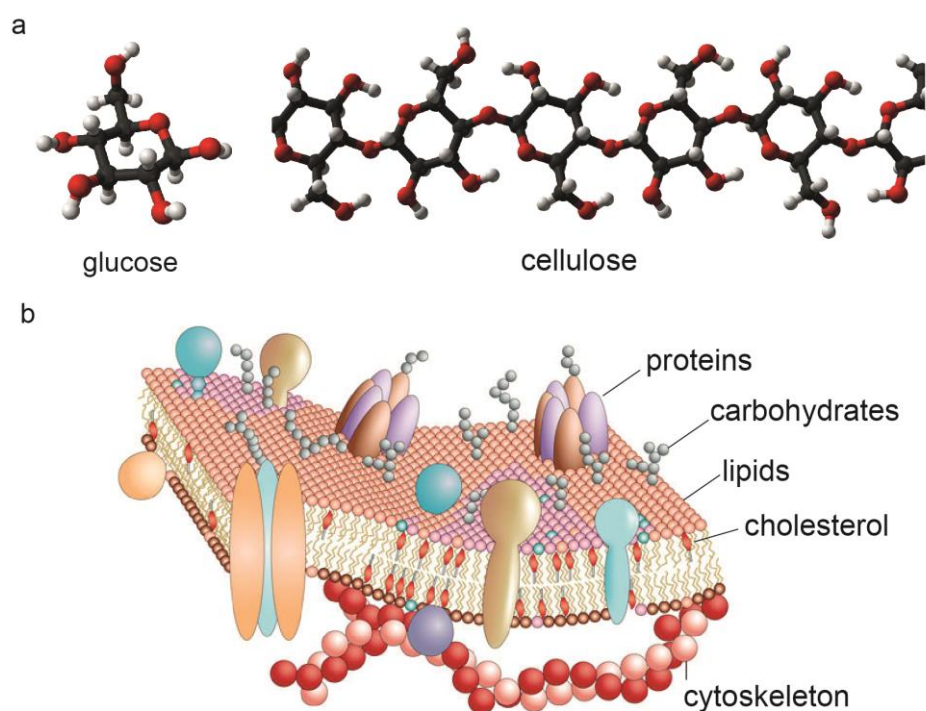
Figure 1:2 Carbohydrates and glycoconjugates. a) Three-dimensional representation of glucose and cellulose carbohydrates. b) Depiction of a cell membrane containing glycoconjugates. Adapted from Ref.[5] Copyright 2010, Nature Education.

In addition to acting as energy carrier molecules, carbohydrates are also essential in cell-cell interactions such as recognition and adhesion. Complex carbohydrates can be found on the surface of cells, and they can be recognized by protein receptors called lectins.[16,17] Carbohydrates can form glycoconjugates when covalently linked to polypeptides or lipids from the other biomolecule classes (Figure 1:2b).[18] These derivatives include glycolipids and glycoproteins, which play a role in cellular recognition and immune response.[2] Five-carbon sugars are also part of the next class of biomolecules discussed, i.e., nucleic acids.

1.1.3   Nucleic Acids

Similar to proteins/polypeptides and carbohydrates/polysaccharides being polymers of monomer subunits, i.e., amino acids and monosaccharides, respectively, nucleic acids / polynucleotides are polymers of monomers called nucleotides. Nucleotides consist of a five-carbon sugar and a nitrogenous base, as well as at least one phosphate group. For deoxyribonucleic acid (DNA), the sugar is deoxyribose, whereas for ribonucleic acid (RNA), the sugar is ribose. There are two families of nitrogenous bases, which are called purines and pyrimidines. Adenine (A) and guanine (G) are purines, whereas cytosine (C), thymine (T), and uracil (U) are pyrimidines. Polynucleotides are chains of nucleotides where the phosphate group of one nucleotide is linked with an oxygen atom from the sugar moiety of another nucleotide to form a phosphodiester linkage.[1]

Nucleobases have specific complementarities, i.e., A is complementary to T, and G is complementary to C. This complementarity leads to DNA adopting a double helix structure with two complementary polynucleotide chains coiling around each other. Unlike double-stranded DNA, RNA is a single-stranded molecule. However, it can still form three-dimensional structures from intrastrand double helices formed by complementary base pairing. In RNA strands, the T nucleobase equivalent is a U nucleobase (Figure 1:3).
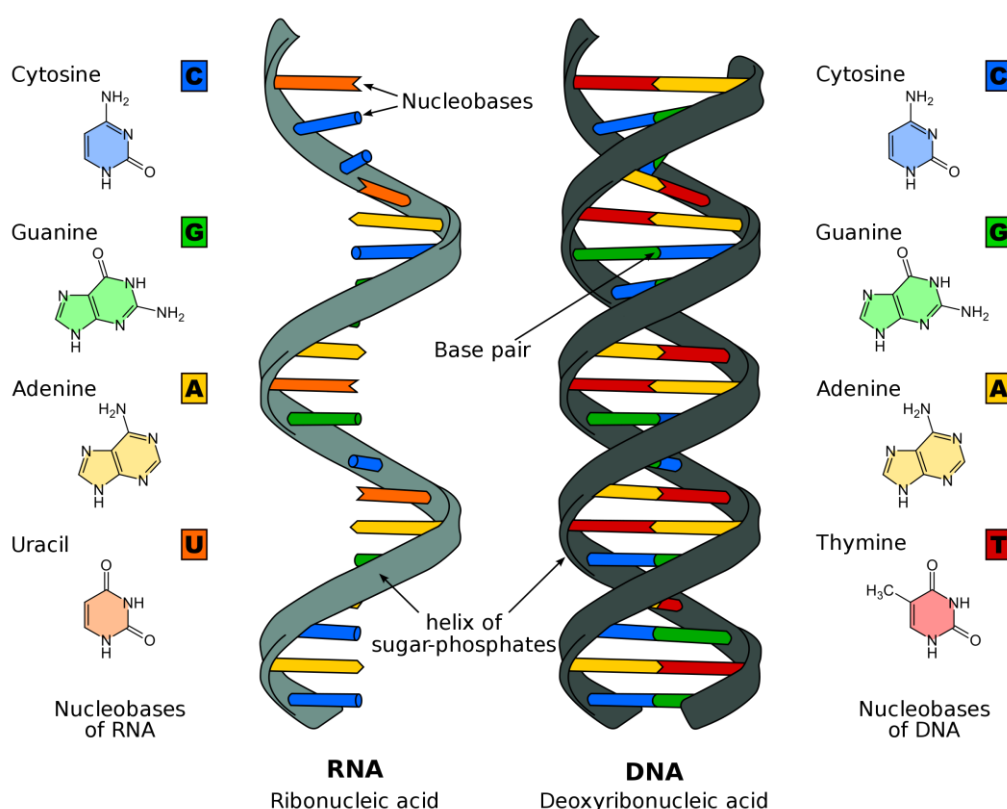
Figure 1:3 Nucleic acids and nucleotides. Schematic depiction of the structures of nucleotides, RNA, and DNA molecules. Image credit: Sponk, Wikimedia Commons.

The sequence of nucleobases A, G, C, and T/U in DNA/RNA strands encodes information that can be translated into proteins by dedicated cell machinery. The protein synthesis process from genetic code starts with the transcription of DNA genes in the cell's nucleus to messenger RNA (mRNA). The transcribed sequence is based on the complementarity of nucleobases. After transcription, the mRNA strand leaves the nucleus and is translated by ribosomes in the cell's cytoplasm. The genetic coding works in the way that each group of three nucleobases, called a codon, corresponds to a specific amino acid. Codons are recognized by transfer RNAs (tRNAs) which carry the corresponding amino acid and allow the ribosome machinery to synthesize the polypeptide chain from the polynucleotide chain. This process is enabled by yet another type of RNA called ribosomal RNA (rRNA), which mechanically enforces the processing of mRNA and tRNA to polypeptides.[19]

Similar to proteins, nucleic acids can also be modified such as through methylation to alter their activity. Methylation of DNA is essential for normal development, and when located in a gene promoter, its effect is usually to repress the transcription of that gene.[20] In many diseases, including

cancer, hypermethylation of gene promoters can occur, causing transcriptional silencing, which can have particularly adverse effects if DNA repair genes are touched.[21]

1.1.4 Lipids

Lipids are a diverse class of biomolecules that can form shape-shifting vessels for transport and compartmentalization. They are generally constituted of a hydrophilic head and a hydrophobic tail, which leads to the formation of lipid bilayers in aqueous environments, where the hydrophobic tails associate and hide from the water leaving only the hydrophilic heads exposed (Figure 1:4a,b). Lipid bilayers are of fundamental importance to all biological membranes as they provide a structural basis, which is flexible thanks to their noncovalent stabilizing forces. Membranes provide the delimitations of cells and separate them from one another, acting as impermeable barriers to most water-soluble compounds. The separation from the surrounding environment allows a cell to maintain the right conditions, such as ionic concentrations crucial for the proper function of the cell components.[22]
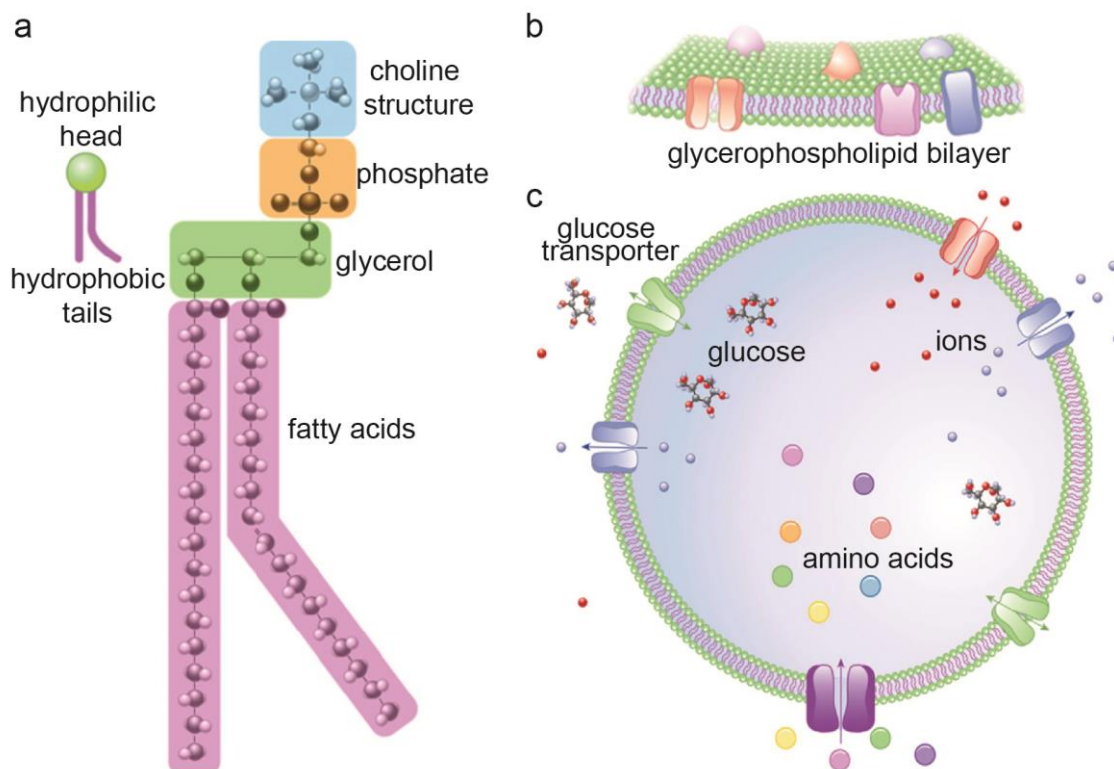
Figure 1:4 Lipids and membranes. a) Single glycerophospholipid molecule with hydrophobic fatty acid tails (purple) and a hydrophilic head comprising a glycerol moiety (green), a phosphate group (orange), and a choline structure (blue). b) Numerous glycerophospholipids forming a lipid bilayer with embedded proteins. c) Lipid bilayer shielding the inside of the cell from its surrounding environment, and transmembrane proteins regulating the transport of molecules and ions in and out of the cell. Adapted from Ref.[5] Copyright 2010, Nature Education.

Transport across cell membranes can be regulated by transmembrane proteins such as channel proteins or more selective carrier proteins to allow for osmosis and the influx of nutrients as well as the excretion of waste (Figure 1:4c). Aquaporin proteins are water channels that facilitate the diffusion

of water across lipid membranes to regulate osmotic pressure. Unlike water molecules, which can also slowly diffuse through lipid membranes without aquaporins, polar nutrient molecules such as glucose are too large to diffuse through lipid membranes and entirely rely on facilitated transport via carrier proteins such as the glucose transporter.[23] While facilitated diffusion is a passive process that does not require energy expenditure, i.e., energy molecules ATP, active transport does require the use of ATP. A critical mode of active transport involves using so-called pump proteins such as the sodium-potassium pump (Na^+/K^+-ATPase), which transports Na^+ out and K^+ into cells against their concentration gradients.[24] Thereby, electrical gradients across cell membranes are maintained, which is particularly important for the ability of nerve cells to respond to stimuli and transmit impulses.

Lipid bilayers are not only used for delimiting cells but also for compartmentalization within cells. For instance, the nuclear envelope consists of two lipid bilayers, an inner and an outer nuclear membrane, surrounding the genetic material. Similarly, mitochondria also have a double lipid membrane that encloses DNA. Mitochondria are organelles that generate the energy used by cells, i.e., ATP molecules. Lipid membranes also provide compartmental structures for lysosomes and the Golgi apparatus, which are also essential parts of eukaryotic cells. The Golgi apparatus packages proteins into lipid vesicles for transport to their destinations, and lysosomes are spherical lipid vesicles that encapsulate enzymes that can break down biomolecules. There are many more types of vesicles,[25,26] such as synaptic vesicles, exosomes, or artificial liposomes-based drugs, which are discussed in the following subsection.

1.2 Vesicular Bionanoparticles

Vesicular bionanoparticles are fascinating systems of biomolecule mixes from the different classes. Their localization, cargo, and membrane-bound docking biomolecules impart them with various functions. In the subsections below, three different types are briefly discussed as examples.

1.2.1 Synaptic Vesicles

Synaptic vesicles are intracellular vesicles that are essential for propagating signals between neuron cells. They are localized in presynaptic cells and filled with neurotransmitter molecules, which they release in the synaptic cleft to bind receptor molecules on the post-synaptic membrane and thereby transmit signals from one neuron to another (Figure 1:5a). Despite their small average diameter of 40 nm,[27] synaptic vesicles have several proteins in their membranes.

The loading of neurotransmitters as cargo molecules occurs via the action of transmembrane transporter pump proteins, which are ATP-dependent, such as the gamma-aminobutyric (GABA) transporter, which loads the vesicles with GABA neurotransmitters. The transport of synaptic vesicles to the synapse is enabled by protein nanomotors from the kinesin family, while the docking to the presynaptic membrane and subsequent priming occurs via proteins such as the SNARE proteins. The primed vesicles quickly fuse with the presynaptic membrane to release the neurotransmitters in the synaptic cleft in response to elevated Ca^+ concentrations and transmit electrochemical signals from one neuron to another.[28]

1.2.2   Exosomes

Exosomes are extracellular vesicles with an average diameter of 100 nm,[29] and are thus larger bionaoparticles than synaptic vesicles, which have an average diameter of 40 nm. Consequently, they have room for more cargo molecules such as DNA, RNA, proteins, and amino acids, as well as membrane proteins and glycoproteins for adhesion, motility, transport, membrane fusion, signaling, and protein trafficking. Exosomes are generated by all cells, and their compositions reflect their origins (Figure 1:5b). They are involved in near and long-distance intercellular communication, but there are many open questions regarding their exact roles in health and disease.[30]

Understanding exosomes can also be translated into new methods for disease diagnosis and novel therapeutics based on engineered exosomes. Exosomes have been reported in all biological fluids so that liquid biopsies and the profiling of exosomes can be useful for disease diagnosis and patient prognosis. Exosome characteristics and properties inspire ways to regulate complex cellular pathways, direct therapeutic payloads to the desired target, enhance pharmacokinetics and bioavailability, and reduce adverse reactions. Liposome-based drugs will be further discussed in the following subsection.
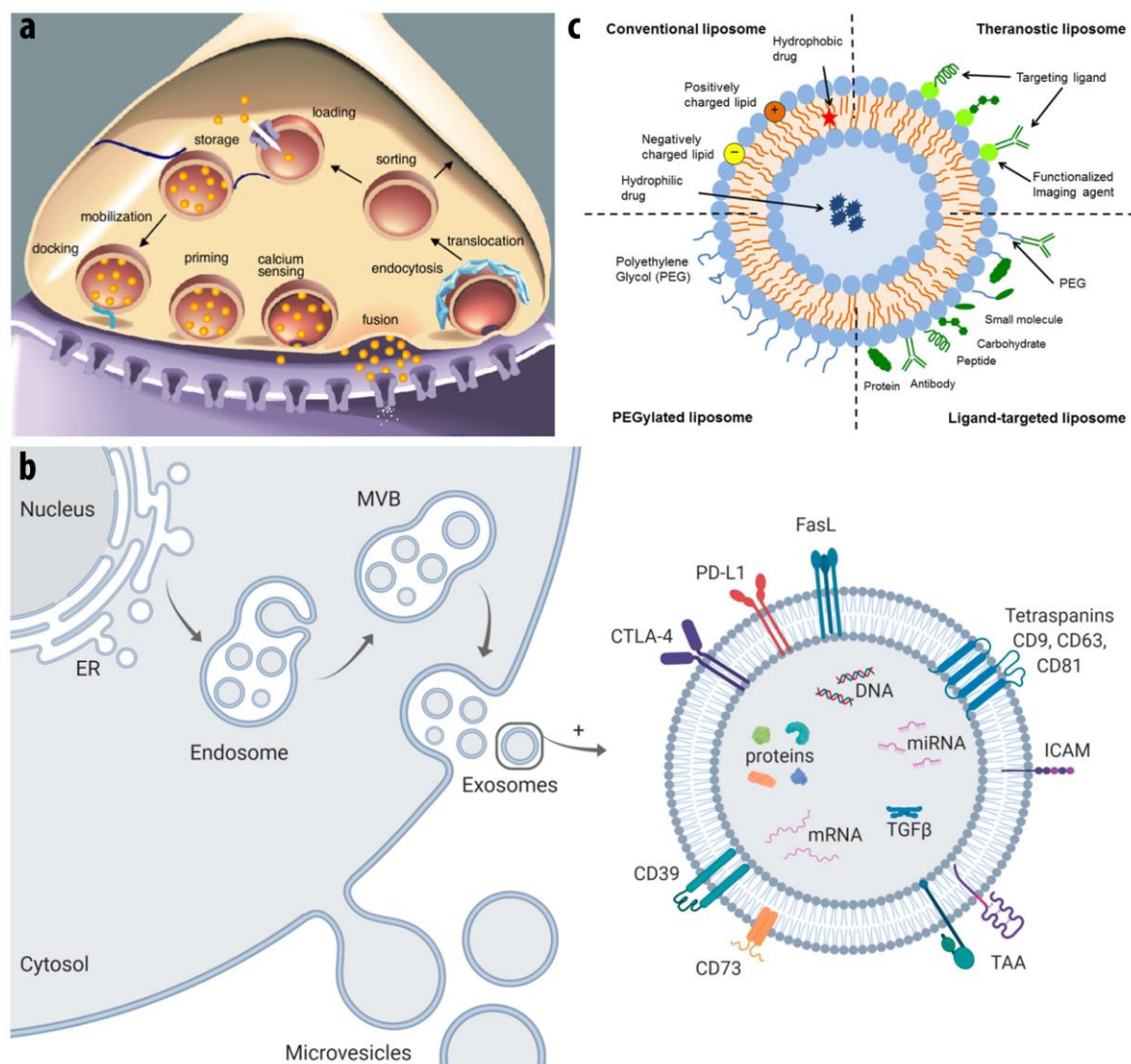
Figure 1:5 Synaptic vesicles, exosomes, and liposomal therapeutics. a) The synaptic vesicle cycle. Copyright 2005, WormBook Research Community. b) Exosomes excreted from a parent cell. Adapted from Ref.[31] Copyright 2020, MDPI. c) Different types of liposomal drug delivery systems. Adapted from Ref.[32] Copyright 2015, Frontiers Media SA.

1.2.3   Liposome-Based Drugs

Liposomes, spherical lipid vesicles, can be used as drug delivery systems for enhanced efficacy and reduced toxicity. They are the first nano-drug delivery systems that have been successfully adopted in clinical applications. There are many liposome-based drugs currently available on the market for the treatment of various diseases and conditions, including cancers, meningitis, leukemia, fungal infections, hepatitis A and influenza.[33]

The success of liposomes as drug delivery systems stems from the fact that they have high biocompatibility and flexible properties. Hydrophobic compounds can be loaded in the membranes, while hydrophilic compounds can be encapsulated in their aqueous core (Figure 1:5c). Liposome carriers have been shown to stabilize therapeutic compounds. Furthermore, the surface of vesicles

can easily be functionalized with ligands and receptors to enhance biodistribution and achieve targeted cellular uptake while minimizing toxicity.[34]

Nucleic acid therapeutics delivered by liposomes are expected to be unique drugs to treat intractable diseases. Among the promising nucleic acid therapeutics are mRNA, small activating RNA (saRNA), silencing RNA (siRNA), or antisense oligonucleotides (ASOs). They hold great potential to fulfill unmet medical needs, as they can directly act on target genes in a sequence-dependent way, and they can be easily chemically synthesized. Liposome carriers could be a solution to address the challenges linked to the delivery of RNA molecules, such as easy degradation in vivo and repelling negative charge density. Liposomes can provide shelter from degrading enzymes and positively charged lipids to screen the negative charges from RNA molecules.[35,36]

Chapter 2   Molecule Sensing and Health

The field of molecule sensing, and particularly biosensing, is expanding, as can be seen from the rapidly growing number of publications, startup companies, and funds. There are several driving factors for this phenomenon, including the introduction of radically new detection schemes and sensor functions resulting from the intertwining of scientific fields such as physics, engineering, chemistry, biology, and data science.

To encompass the exciting wealth of emerging technologies, we use the inclusive terms "molecule sensing" or "chemical sensing" to refer to sensor technologies developed for sensing all kinds of molecules/chemicals, using various non-restrictive operation principles (Figure 2:1). Biosensors are a subcategory of sensors, which specifically use receptors made from biological materials, i.e., bio-receptors, to bind target analytes, which are usually biomolecules but can also be other chemicals.

2.1   Importance of Biomolecule Sensing for Healthcare

The importance and role of biosensors and other molecule sensors in the healthcare sector is growing, as such sensors are beneficial on multiple levels, including helping with the diagnosis of diseases, the characterization and development of drugs, as well as the understanding of both pathological and physiological processes.

A considerable part of research and investment focuses on developing diagnostic tools for point-of-care testing (POCT) to help tackle the severe health issues associated with diseases afflicting humans worldwide.[37] For instance, POCT devices for hepatitis B, malaria, tuberculosis, HIV, and Ebola have been developed.[38] Another timely example is the use of POCT for Covid-19, where SARS-CoV-2 rapid antigen tests were produced and distributed, thereby significantly contributing to reining in the pandemic.[39,40]

In addition to helping with the diagnosis of diseases, molecule sensors can also play a role in their treatment, e.g., by contributing to the development of pharmaceuticals or therapeutic drug monitoring for dosage adjustment.[41] Biosensors are used for drug discovery/characterization, and the analysis of protein stability as well as activity in biopharmaceutical production.[42] For example, SPR biosensors give access to information such as the binding kinetics of a drug, which is very important for establishing its duration of action and clinical benefit, as well as differentiating between similar drug compounds.[43,44] The emergence of organ-on-a-chip biosensors is also noteworthy, as their ability to mimic in vivo microenvironments is of great interest for monitoring drug efficacy and toxicity of drugs.[45]

Beyond diagnosis and treatment, biosensors can also contribute on a more fundamental level by helping to acquire a better understanding of basic cellular processes and disease mechanisms. For instance, proximity-dependent biosensors have been used to measure protein-protein interactions in cell signaling pathways, which is vital for understanding fundamental cellular regulation and

developing therapeutics targeting interactions whose dysregulation is associated with disease.[46,47] Another example is biosensing based on mechanical trapping of molecular interactions to measure protein-DNA interactions, enabling the prediction of gene regulatory networks.[48] Electrochemical biosensors can also be great tools for studying the central nervous system, e.g., by quantifying neurotransmitter transport dynamics.[49,50]

It is thus clear that molecule sensing, and particularly biosensing, has already taken an important role in the healthcare sector, yet, there is still a lot of room for innovations and to demonstrate new sensor capabilities.

2.2   Working Principle of Biomolecule Sensing

The process of molecule/chemical sensing is composed of several elements that together enable to detect signals caused by the binding or mere presence of analytes (Figure 2:1). Samples containing the analytes can be complex such as saliva, blood, breath, exhaust, or other fluids containing many different molecules, but they can also be simple buffer solutions or gases containing a few or even just a single analyte.
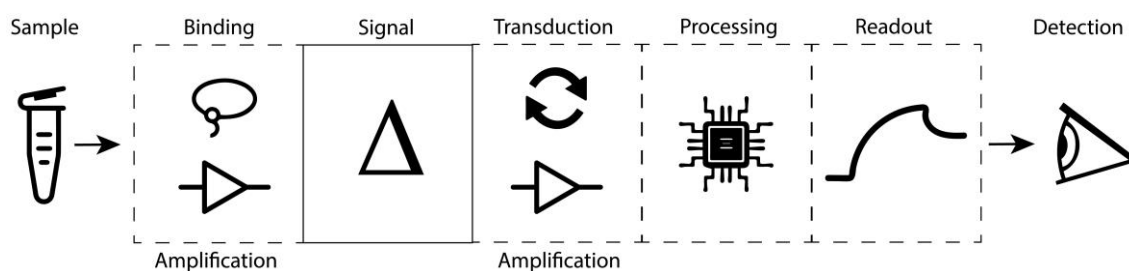
Figure 2:1 General schematic for the process of chemical/molecule sensing and its elements. The dotted line rectangles indicate the non-essentiality of an element, whereas the continuous line rectangle indicates the element which is a necessary part of the chemical/molecule sensing process. Sensors with a binding factor based on bio-receptors are categorized as biosensors.

Some sensors have an initial amplification step in which the targeted analyte, if present in a sample, is replicated to increase its concentration and thereby facilitate its detection. An example is biosensors specialized in detecting microRNA (miRNA), which are small biomolecules of high diagnostic value due to their essential roles in biological processes and their involvement in cancer. These biosensors often use polymerase chain reaction (PCR) methods to amplify the number of miRNA analytes.[51,52] PCR amplification is also having a prominent role in SARS-CoV-2 RNA detection.[53] Some sensors have a different type of amplification step, where the targeted analyte is augmented in a way to increase its signal impact. One example is the binding of large nanoparticles to the analyte, e.g., to increase its mass or optical signal for enhanced detection.[54]

A very common, albeit not strictly essential, step for all sensor types is binding the analyte before detection. The binding usually occurs via receptors specific to a particular target analyte, and sensors that use bio-receptors are called biosensors. Common bio-receptors are antibodies and DNA aptamers due to their specificity and affinity for target analytes.[55,56] In contrast, some sensors such as electronic

tongues and noses use a mix of non-specific receptors with varying degrees of affinity so that analytes generate a fingerprint-like binding pattern that enables detection.[57–59] Binding can also occur without receptors, e.g., by simple physisorption, such as in the case of supported lipid bilayer (SLB) formation on silica surfaces,[60,61] or the binding of DNA to graphene.[62] In fact, some sensors might not even strictly require the binding of analytes to detect them. For example, infrared optofluidic sensors can detect analytes merely flowing by thanks to the retrieval of characteristic infrared absorption bands, e.g., detecting the neurotransmitter GABA with the sensor which we will introduce in Chapter 5.
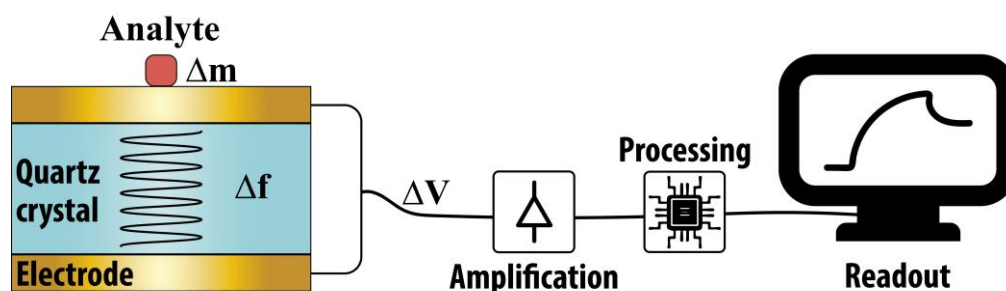
Figure 2:2 Schematic of QCM sensor operation. A quartz crystal is sandwiched between two electrodes which generate an acoustic resonance via the piezoelectric effect. As analytes bind to the surface, the mass change Δm leads to a change in acoustic resonance Δf, this acoustic signal is then further converted via piezoelectric transduction to an electric signal ΔV for amplification, processing and readout.

Molecule sensing requires at the very least the generation of a signal, i.e., a change in a physical quantity such as mass, light, heat, or electrical charge. Most molecule sensors also include a transducer, which converts one form of energy into another to generate a measurable signal.[63] Transducer elements can, for example, be of electrochemical, piezoelectric, or optoelectronic nature.[64] In the example of quartz crystal microbalance (QCM) sensors (Figure 2:2), the analyte will bind and thereby create a change in mass Δm, this signal will then be converted to a change in acoustic resonance Δf, and the acoustic signal will then further be converted to an electrical signal ΔV via a piezoelectric transducer.[65] Another example are sensors based on surface plasmon resonance (SPR),[66] where the binding of an analyte leads to an increase in electron density $\Delta \rho_e$, this signal is then converted to a change in optical resonance. This optical signal $\Delta \gamma$ is eventually converted to an electrical signal ΔV via a photodetector, which can be amplified before processing, e.g., to output a typical sensorgram for readout (Figure 2:3). It is noteworthy that while some sensors have one or more transduction steps, other sensors do not have any transducer element, e.g., the common lateral flow pregnancy or rapid SARS-CoV-2 antigen tests, where the optical signal generated upon binding can be directly seen by the user.[67]
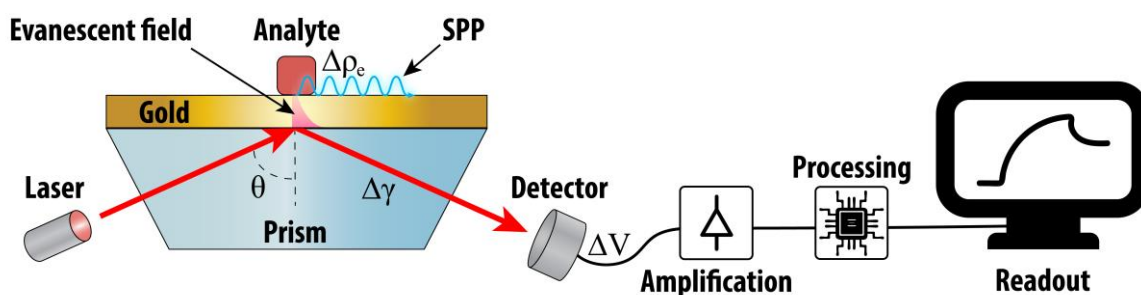
Figure 2:3 Schematic of SPR sensor operation. A laser beam shines through a prism and impinges on a thin nanolayer of gold at the resonance angle θ that will excite surface plasmon polaritons (SPPs) on the gold surface in contact with the sample medium. Analytes in the vicinity of the SPP will modify the electron density $\Delta\rho_e$ and thus the resonance angle. This resonance shift can be measured either as a change of light intensity at a fixed angle or as a change in resonance angle by angle scanning. This optical signal $\Delta\gamma$ is then converted by a photodetector to an electrical signal ΔV before amplification, processing and readout, which is typically in the form of a sensorgram representation.

2.3   Label-Free and Chemically Specific Sensing Techniques

It is advantageous to use a real-time and label-free monitoring setup to investigate physiological interactions between biomolecules because labels can interfere with the biological process under investigation, e.g., attaching fluorescent dyes to analytes can modify their native behavior (Figure 2:4a). Among the most prominent label-free technologies are SPR and QCM sensors.[66,68] These techniques are sensitive enough to detect monolayers of biomolecules in aqueous solutions and are thus widely used in biochemistry to determine affinities between different biomolecules.[69] However, they lack the intrinsic capability of giving information on the chemical identity of the biomolecules attached to the sensor surface and thus struggle to resolve mass-preserving biological processes (Figure 2:4b). Furthermore, they provide only minimal information on the conformation of the bound biomolecules, thereby making it challenging to investigate complex biological processes involving different chemical species in different conformations. These complex multi-component systems are typically studied using a combination of other methods such as nuclear magnetic resonance (NMR),[70] circular dichroism (CD),[71] electron spin resonance (ESR),[72] Raman,[73] or infrared (IR) spectroscopy.[74]
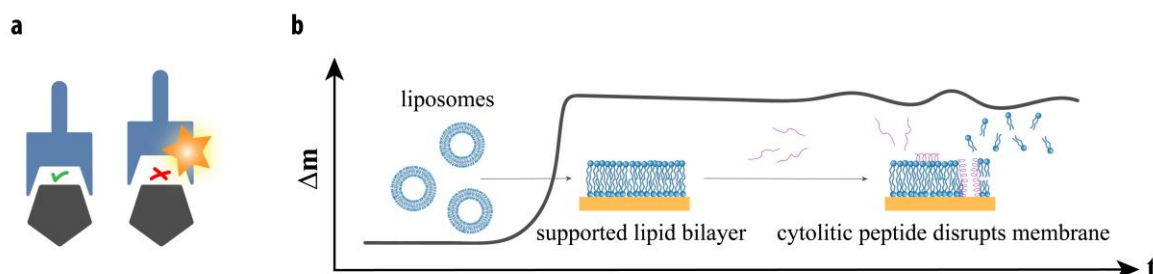
Figure 2:4 Labels and chemical specificity issues. Illustration of a) label interference in biomolecular binding processes b) and limitations of non-chemically specific sensing for resolving mass-preserving biological processes.

While NMR and ESR spectroscopy provide chemically specific and even conformation-sensitive detection, these techniques require significant sample preparation times and large sample quantities. Besides, NMR is not well-suited for the analysis of large proteins.[75] CD spectroscopy is label-free and can resolve the secondary structure of biomolecules, but it is not well-suited for analyzing complex mixtures. Raman and IR spectroscopy are methods that, in principle, allow label-free, chemically specific, and even conformation-sensitive monitoring of multi-analyte systems. However, each of these two techniques has its limitations. Raman spectroscopy uses high-power UV/visible light sources, which can be phototoxic to biological samples, thereby restricting the monitoring time during experiments.[76] Surface-enhanced Raman spectroscopy (SERS) is an extremely sensitive implementation of this type of spectroscopy. It makes it possible to detect conformational changes of single molecules, such as the flexing of lipids as reported by the Evans group.[77] However, this extreme sensitivity comes to the cost of exacerbated phototoxicity. In particular, the intense surface-enhanced near-fields enhance not only the detected signal but also a whole range of photochemical phenomena such as photofragmentation, photodesorption, photoisomerization, and photoreduction.[78] Furthermore, providing optimal enhancement for CH vibration modes around 3000 cm^{-1}, e.g., in lipids, can be challenging due to the spectral separation between the excitation wavelength and the absorption bands.[79,80] Nevertheless, many biological studies can be carried out with SERS under the right conditions.[81] Phototoxicity is generally not a problem in IR spectroscopy, but this technique, in its traditional implementations, is generally plagued by several other limiting aspects. The basics of IR spectroscopy and how its limitations can be overcome are discussed in the next chapter. Before focusing on IR spectroscopy in the next chapter, the need for chemometrics in vibrational spectroscopy is discussed in the following subsection.

2.4   Artificial Intelligence for Vibrational Spectroscopy

Vibrational spectroscopy techniques such as Raman and IR Spectroscopy generate spectra composed of hundreds or thousands of individual frequency data points. This wealth of data is not only ideal for exploitation with artificial intelligence (AI) methods, which are notoriously hungry for large data sets, but it is often necessary to resolve the composition of complex systems with partially overlapping signal contributions from the different biomolecules.[82] In addition to enabling vibrational fingerprint recognition with high accuracy, relationships and correlations between spectral features can be uncovered by AI methods.[83]

AI is a broad term that encompasses several methods from subfields and can be thought of like the outer layer of an onion, where the next layer is machine learning (ML), followed by neural networks (NNs), and eventually deep neural networks (DNNs) or deep learning at the core. One of the simplest but powerful and widely used ML methods is multiple linear regression (MLR). It can decompose spectra from samples with two or more analytes with partially overlapping signals to resolve the individual signal contributions.[84] MLR is part of the many ML methods based on supervised learning, i.e., using labeled training data for the algorithm to learn to map outputs to inputs to acquire the ability to predict input-output pairs from unseen data. Other ML methods based on supervised

learning include linear discriminant analysis (LDA), support vector machines (SVMs), k-nearest network (KNN), and random forest (RF) algorithms.[85]

These ML techniques typically require extensive data preprocessing steps,[86] including the removal of interference from artifacts. In contrast, DNNs can cope well with spectral artifacts, e.g., from environmental, instrumental, or method-specific origins. DNNs offer multiple processing layers, which can significantly improve fitting and informative spectral feature extraction capabilities and therefore provides a powerful method to deal with various analytical tasks and increasing numbers of analytes and sample sources.[87,88]

Chapter 3   Mid-IR Spectroscopy

Parts of this chapter have been adapted from a review published in Angewandte Chemie International Edition.

Authors: Andreas Tittl, Aurelian John-Herpin, Aleksandrs Leitis and Hatice Altug

Contribution: A. J.-H. co-wrote the manuscript.

Reference: Tittl, Andreas, Aurelian John-Herpin, Aleksandrs Leitis, Eduardo R. Arvelo, and Hatice Altug. "Metasurface-based molecular biosensing aided by artificial intelligence." Angewandte Chemie International Edition 58, no. 42 (2019): 14810-14822.

Permission to reproduce the article is granted by the American Chemical Society.

IR spectroscopy is a label-free and chemically specific technique that has enabled a wide range of sensing applications across diverse fields, such as chemical engineering, pharmaceutical research, materials science, environmental monitoring, and personal health.[89] It can be especially impactful for biomolecule sensing, in which the possibility of detecting and differentiating the absorption signatures of the basic building blocks of life, including lipids, proteins, and nucleic acids (Figure 3:1), is a great asset.

The mid-IR spectral range is ideally suited for detecting and identifying a multitude of different molecular species because it contains characteristic vibrational absorption bands directly correlated with the nature and configuration of the chemical bonds within the molecular structure. IR spectroscopy retrieves these molecular absorption fingerprints using Fourier-transform IR (FTIR) spectrometers or tunable laser sources. It can therefore provide chemically specific information on the constituent materials in single- or multi-analyte systems.[90–94]
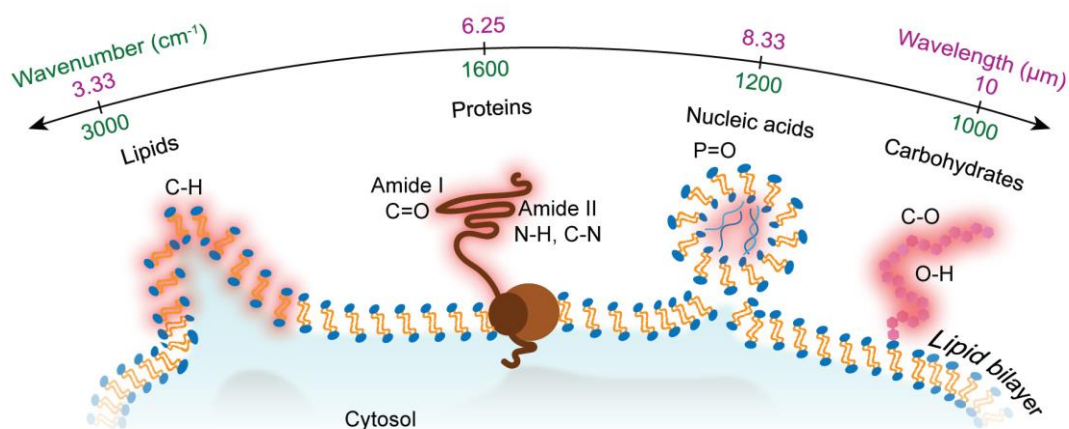
Figure 3:1 Mid-IR spectroscopy and biomolecules. Fundamental biological building blocks, i.e., lipids, proteins, sugars, and nucleic acids, have characteristic molecular bond vibration bands across the mid-IR range.

3.1   Traditional IR Spectroscopy Techniques

Most IR spectroscopy techniques measure absorption; however, it is also possible to measure emission or acoustic signals with IR emission spectroscopy (IRES) or photoacoustic IR spectroscopy (PA-IRS), respectively.[95,96] IRES requires the heating of samples to measure their radiation emission, with temperatures typically well above 37 °C, and consequently unsuitable for biological studies. As for PA-IRS, measurements are usually performed on bulk materials with thicknesses of at least several micrometers,[97,98] and thus not suitable for studying biological systems at the nanometric scale.

In IR absorption spectroscopy techniques, the absorbance A is calculated from the measured light intensity I, as shown in Equation 3:1.

$$\text{A} = -\log_{10}\left(\frac{I}{I_0}\right) = \varepsilon \cdot d \cdot C$$

Equation 3:1 – Spectroscopic absorbance and Beer-Lambert's law.

I_0 represents the reference light intensity before interacting with the sample of thickness d, concentration C, and absorptivity ε. Measurements can be carried out either in transmission or reflection so that $I = T$ or $I = R$, respectively. From Beer-Lambert's law in Equation 3:1 and Figure 3:2, one can see that in simple transmission measurements, minute quantities of analytes ($C \searrow$) and thin monolayers of molecules ($d \searrow$) are very challenging to detect.[99] This sensitivity limitation can be addressed with some IR absorption spectroscopy techniques based on a reflection configuration, e.g., attenuated total reflection (ATR) and infrared reflection-absorption spectroscopy (IRRAS).
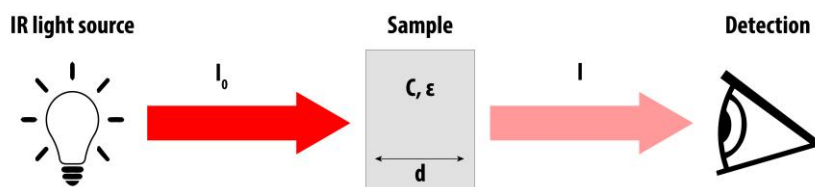
Figure 3:2 IR transmission spectroscopy.

In IRRAS, a reflecting substrate coated with analytes is illuminated at a grazing angle φ, which increases the pathlength d' of the light through the sample (Figure 3:3), leading to increased light-matter interaction to boost the absorbance signal. Additionally, the signal is increased by a factor of 2 due to the mirror-dipole effect thanks to the reflective substrate.[100] The signal dependence on the angle φ and the sample of thickness d and the perpendicular component of the dielectric function $\varepsilon_\perp$ can be seen in Equation 3:2, where ω and c represent the circular frequency and the velocity of light, respectively.[101,102]

$$\frac{I}{I_0} \approx 1 - 4 \cdot d \cdot \frac{\omega}{c} \cdot \frac{\sin^2 \varphi}{\cos \varphi} \cdot Im\left(\frac{-1}{\varepsilon_\perp(\omega)}\right)$$

Equation 3:2 – IRRAS formula
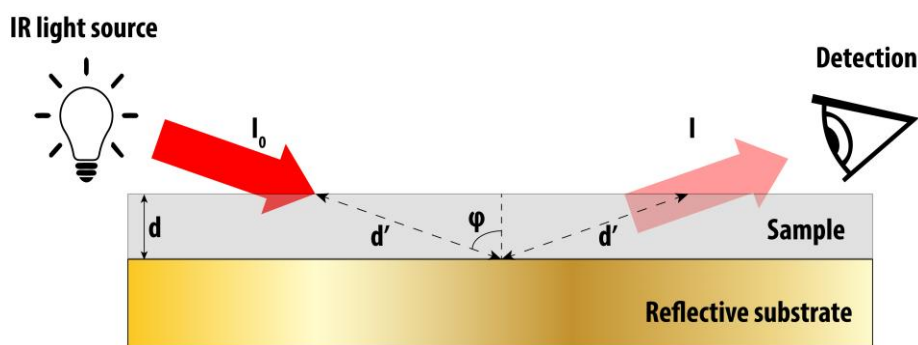
Figure 3:3 Schematic of IRRAS measurement configuration.

While IRRAS is compatible with measurements of molecule monolayers,[103] it is not well-suited for measurements in water due to the strong absorption of water molecules, which typically obscure the absorption signals of the molecules of interest. Figure 3:4 shows the absorbance spectrum of water in

the mid-IR range and its overlap with the two major absorption bands of proteins, i.e., the amide I and II bands.
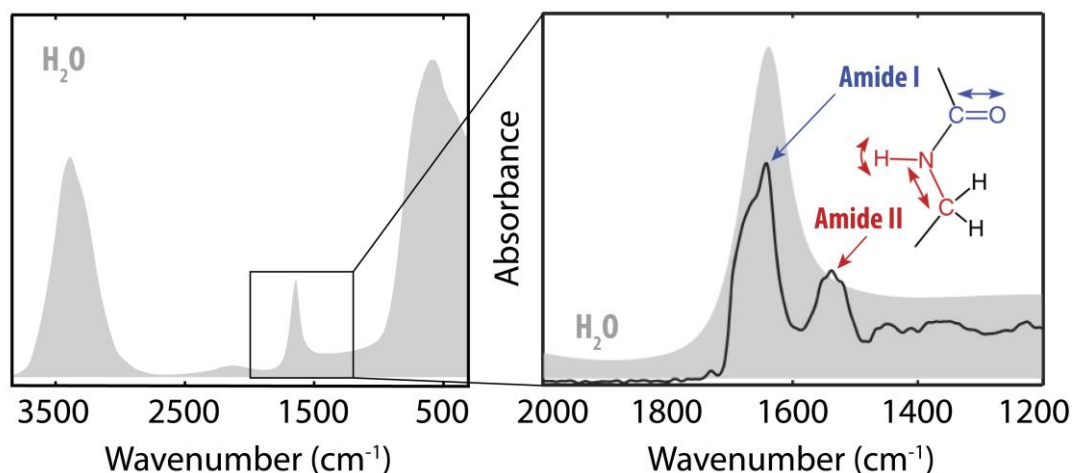
Figure 3:4 Absorbance spectrum of water and its overlap with the amide I and II absorption bands of proteins. Adapted from Ref.[104]. Copyright 2013, Nature Research.

Water interference is a general issue for IR absorption spectroscopy techniques, but it is especially limiting for measurement configurations where the IR light has to directly travel through water, as in simple transmission measurements (Figure 3:2) and for IRRAS (Figure 3:3). One reflection technique called attenuated total reflection (ATR) IR spectroscopy addresses this issue with a measurement configuration that circumvents the need for IR light to travel directly through the water.

In ATR IR spectroscopy, the sample is in contact with a prism of refractive index higher than that of the sample. The angle of incidence of the IR light into the prism is higher than the critical angle so that total internal reflection occurs.[105] Thereby, only the evanescent field penetrates the sample, which can thus be in an aqueous solution. The penetration depth of the evanescent field is generally around half a micron and can be tuned by adjusting the incidence angle and the prism refractive index. Using multiple reflections can increase the interaction of light with the sample and thereby improve sensitivity. However, at the same time, the longer the optical path length, the lower the intensity of the collected light. This limits the sensitivity that can be reached, and the geometrical constraints of this configuration restrain its applications.[104,106]
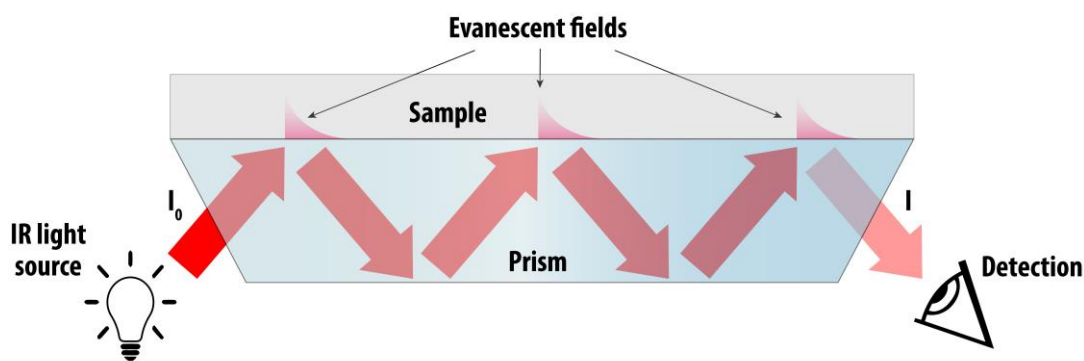
Figure 3:5 Schematic of ATR measurement configuration.

A more recent IR absorption spectroscopy technique overcomes sensitivity and water interference issues in a simple geometrical reflection configuration using near normal light reflection from plasmonic nanoantenna resonances.[104]

3.2   Plasmon-Enhanced Mid-IR Spectroscopy

Nanotechnology and, specifically, nanophotonics can bridge the gap in length scales between IR wavelengths (on the order of microns) and molecular analyte dimensions (on the order of nanometers) using resonant nanoantennas for surface-enhanced IR absorption spectroscopy (SEIRAS) (Figure 3:6, left).[107] Such antenna geometries focus the incident light into hot spots of the electromagnetic fields, providing strong light-matter interaction and enabling the detection of otherwise weak absorption signatures down to, e.g., monolayers of proteins (Figure 3:6, right).[108,109] SEIRAS techniques leverage an enhancement mechanism proportional to the near-field intensity around the nanostructures, in which spectrally and spatially colocalized vibrational dipoles of molecules are excited at an increased rate. The sensitivity and, consequently, the limit of detection of SEIRAS is crucially determined by the geometry, material choice, and spatial arrangement of the nanostructured antenna elements. The following sections highlight some of the central design paradigms for highly sensitive metasurface resonators, focusing on metal-based, plasmonic antenna elements.
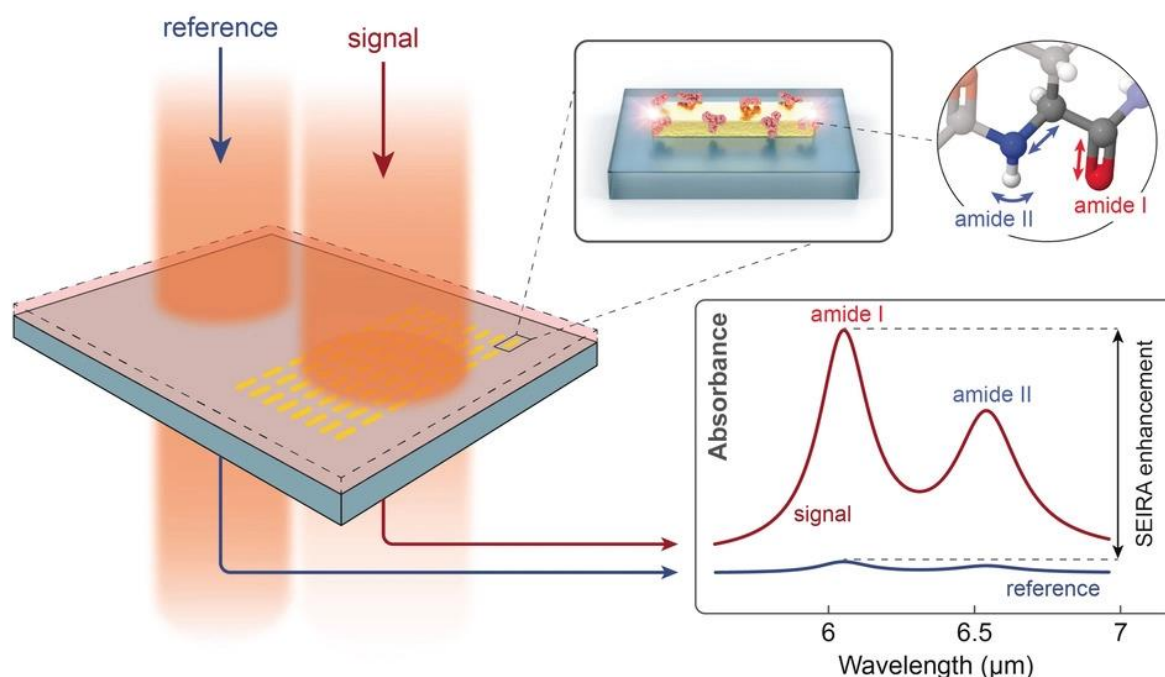
Figure 3:6 Surface-enhanced infrared absorption spectroscopy (SEIRAS). Infrared absorption spectroscopy optically detects the characteristic vibrational bands of molecules associated with their chemical bonds. Resonant nanoantennas can enhance these signatures and access chemical and compositional information from monolayers and few-molecule systems.

Metal-dielectric interfaces support propagating electromagnetic surface waves based on the collective oscillations of the conduction electrons in the metal, commonly referred to as surface plasmon resonances (SPR).[66,110] Because of their propagating nature, such SPR systems commonly confine electromagnetic energy only in the direction perpendicular to the interface. In contrast, specifically designed metal nanoparticles can provide localized surface plasmon resonances (LSPR), which can be resonantly driven by an external electromagnetic field and focus light into deeply subwavelength volumes, enabling a wide array of nanophotonic sensing schemes over broad wavelength ranges.[111–114]

3.2.1 Plasmonic Nanoantennas

In the context of plasmonic SEIRAS, rod-type nanoantennas constitute an ideal sensing platform due to their large dipole moments, comparatively simple resonant mode structure, and strong localization of the electric near-fields at the antenna tips.[115] In one of the earlier experimental studies on vibrational antenna coupling,[100] Neubrech et al. observed significant near-field intensity enhancement factors $|E|^2/|E_0|^2$ above 2000 in the mid-IR for rod-type gold nanoantennas with a length of around 1.5 µm (Figure 3:7a, top). When performing relative IR transmittance measurements of single nanoantennas before and after adding octadecanethiol (ODT) molecules, which exhibit a strong vibrational signature at around 2900 cm^{-1}, they found a distinct modulation of the resonance line shape associated with the respective absorption bands (Figure 3:7a, bottom). In particular, they described these often asymmetric line shapes in terms of a Fano-type interference between resonant

states with strongly dissimilar resonance widths, establishing a link to other fundamental coupling phenomena in nanophotonics.[116–118]
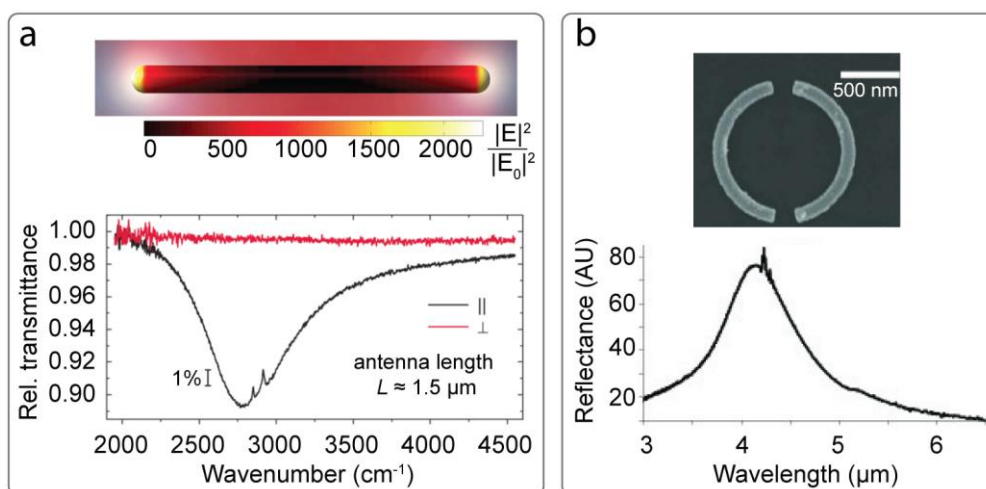
Figure 3:7 Mid-IR plasmonic nanoantennas. a) Electric near-field enhancement (top) and relative transmittance spectra (bottom) of a plasmonic rod-type nanoantenna after coating with a monolayer of ODT molecules. Adapted from Ref.[100] Copyright 2008, American Physical Society. b) SEM image of a split ring resonator (top) and experimental reflectance spectrum of an array of such resonators (bottom). Adapted from Ref.[119] Copyright 2009, American Physical Society.

Besides rods, nanoantennas of various shapes, including circular geometries, have been demonstrated (Figure 3:7b). Similarly to tuning the length of nanorods, the spectral position of the resonance can be adjusted by tuning the diameter of the circular resonators.[119,120] In Figure 3:7b, the far-field response of an array of resonators is measured instead of a single resonator as in Figure 3:7a. The benefits of using arrays of resonators are discussed in the following subsection.

3.2.2   Plasmonic Nanoantenna Arrays

The sensitivity of such antenna systems can be increased significantly by arranging them in periodic arrays to leverage the effects of radiative coupling between the individual resonant elements.[108,121,122] In general, strong enhancement is obtained when the antenna resonance frequency matches one of the collective excitations associated with the metallic array, which are often referred to as grating orders or Rayleigh anomalies.[123] Since the spectral positions of the grating orders are governed by the array periodicities,[124] this opens up new degrees of freedom for sensor design. Adato et al.[108] demonstrated the first use of engineered nanoantenna arrays to enhance the spectroscopic signatures of a nanometer-thick silk protein monolayer. The authors showed that collective coupling of the nanoantenna resonances with the proper grating condition could provide more than an order-of-magnitude signal amplification than the nanoantenna resonances in random arrangements. Bagheri et al.[125] later analyzed the influence of grating coupling on surface-enhanced sensing performance by investigating arrays of identical gold nanoantennas with a wide range of inter-element distances, both parallel (d_x) and perpendicular (d_y) to the long axis of the antennas (Figure 3:8a, top). Large-area antenna arrays with an antenna length of 2.6 µm were fabricated using femtosecond direct laser

writing and ion-beam etching, followed by evaporation of a thin layer of 4,40-bis(N-carbazolyl)-1,10-biphenyl (CBP), which provides strong and characteristic vibrational absorption bands at 1230, 1450, and 1504 cm^{-1}.[126] In mid-IR reflectance measurements, the authors found that both very dense ($d_x = d_y = 1$ µm) and very sparse arrays ($d_x = d_y = 8$ µm) produced low enhancement factors of the vibrational signals. In contrast, a much stronger enhancement was found when the perpendicular antenna spacing was adjusted in accordance with the grating coupling condition to $d_x = 1$ µm and $d_y = 2$ µm, highlighting the sensitivity impact of tailored array periodicities (Figure 3:8b, bottom). In addition to the importance of tuning array periodicities along both x- and y-directions, Maß et al.[127] demonstrated the influence of the incident angle of the exciting light on the grating coupling and how it can be used to tune the spectral resonance position without changing the geometrical parameters of the antennas Figure 3:8b. The authors experimentally leverage the effect of incident-angle tuning to maximize the signal enhancement from self-assembled monolayers of 16-Mercaptohexadecanoic acid (16-MHDA) on their antenna arrays.
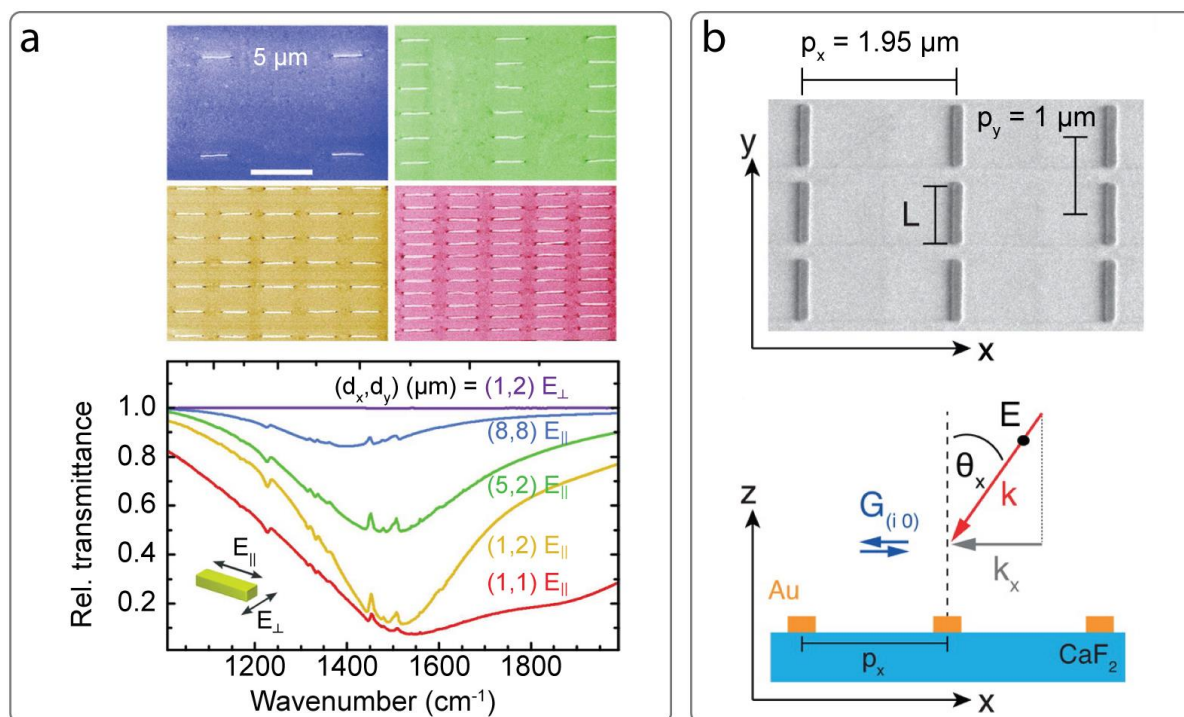
Figure 3:8 Nanoantenna arrays. a) SEM images (top) and relative transmittance spectra (bottom) of gold antennas in arrays of different inter-antenna distances d_x and d_y. Adapted from Ref.[125] Copyright 2015, American Chemical Society. b) SEM image of a rod-type antenna array with periodicities p_x and p_y (top) and schematic of perpendicular polarized light incident on the antenna array with incident angle θ_x, in-plane k component k_x, and reciprocal lattice vector $\overrightarrow{G_{(i,0)}}$.[127]

3.2.3 Multiresonant Plasmonic Metasurfaces

Going beyond simple rod-type shapes, antennas with more complex geometrical structures can provide increased sensing performance and additional functionalities such as the simultaneous enhancement of more than one vibrational band. In this context, Chen et al. have introduced a dual-band design for surface-enhanced spectroscopy,[128] which utilizes asymmetric cross-shaped gold

antennas placed above a dielectric spacer layer and a gold mirror in a "perfect absorber" configuration.[129–132] The authors observed two distinct modes M1 and M2, in this structure, which exhibited pronounced resonance line shapes in reflection together with strong near-field enhancements, even for large spectral mode separations (Figure 3:9a, left). Significantly, they also found that the resonance frequencies of both modes could be adjusted independently and over a broad range by modifying the dimensions of the cross-shaped antenna, allowing them to target different vibrational bands. This capability was demonstrated experimentally by simultaneously resolving widely separated absorption bands of a thin PMMA layer with high sensitivity (Figure 3:9a, right).

In IR spectroscopy and sensing, a single resonant nanoantenna cannot access the full set of molecular absorption fingerprints and therefore provides only a partial view of the complete chemical information available in the infrared spectrum.[116,117] Thus, there is an increasing need to conceptualize and develop novel nanostructures with wider bandwidth that can manipulate and enhance light over extended spectral ranges.

In the pursuit of broadband light enhancement, various multiresonant plasmonic nanoantenna structures are currently under study, including fractal geometries,[118,121–124] cross,[125,126] and U-T shapes,[128,129] superimposed Moiré,[130] and Fisher patterns,[131] concentric nanorings,[132] multigratings,[133,134] polarization-dependent antennas,[135,136] zigzag trapezoids,[137,138] and tapered multidipoles.[139,140] The common idea behind these methods is using multiscale geometries that allow the excitation of multiple resonances. For example, Wallace et al.[135] demonstrated dendritic structures with different shapes and numbers of branches to provide resonances from the near- to the mid-IR (Figure 3:9b). The authors demonstrate the suitability for SEIRA by performing measurements with 4-nitrothiophenol (4-NTP) functionalized dendritic fractals.
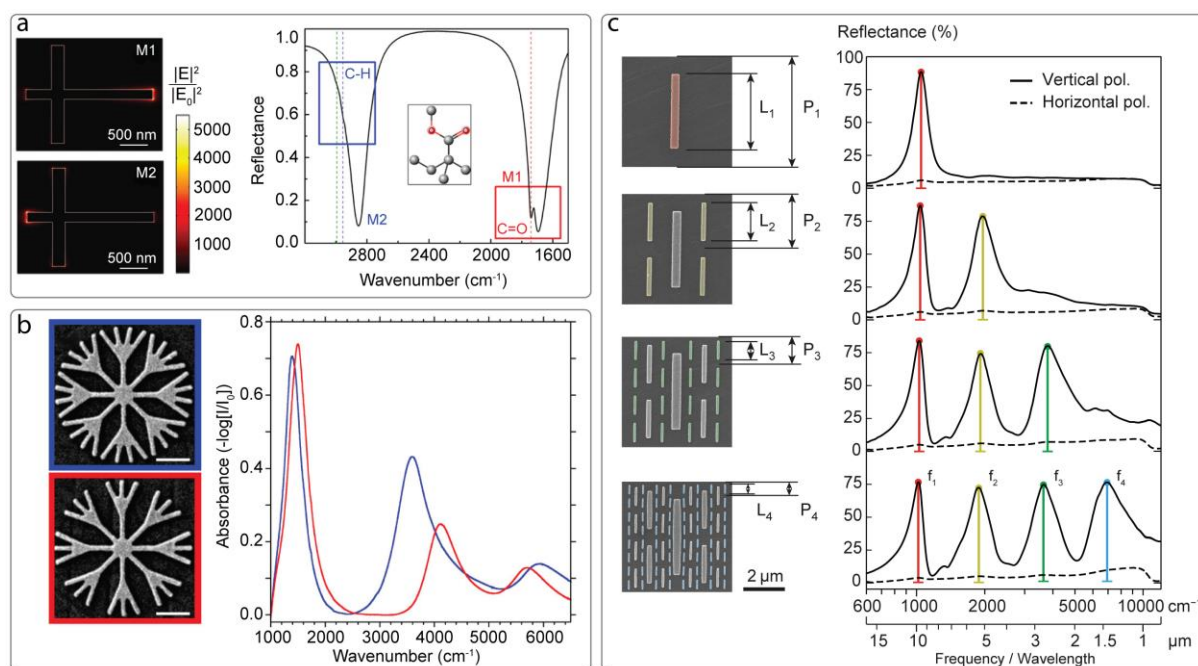
Figure 3:9 Multiresonant IR metasurfaces. a) Electric near-field enhancement (left) and reflectance spectrum (right) of a cross-type gold antenna placed above a dielectric spacer layer and a gold mirror, showing dual resonant SEIRAS operation. Adapted from Ref.[128] Copyright 2012, American Chemical Association. b) SEM images (scale bar: 400 nm) of dendritic fractals (left) and corresponding, color-coded absorption spectra.[135] c) SEM images (left) of self-similar rod arrays with one to four iterations in the fractal-like generation of subarrays, respectively leading to one to four resonance peaks as seen in the measured IR reflectance spectra (right).[134]

In the design of multiresonant antennas, it is fundamentally challenging to accommodate resonant modes with equally strong excitation efficiencies over a broad spectrum due to the large size mismatch between the antennas resonating at the far end points of the spectral operating range. In particular, the high-frequency modes are typically weak, strongly limiting their usability. Additionally, the large nanoantenna array periodicities needed to support long-wavelength operation can produce unwanted excitation of grating modes at shorter wavelengths. As a result, current multiresonant nanoantennas allow only a small number of resonant modes with nonuniform spectral coverage. Furthermore, some of the introduced plasmonic designs are based on complex unit cell geometries where scaling and nanofabrication are not straightforward. In such cases, the specific resonance wavelengths are mutually interdependent and often cannot be independently controlled in a simple manner. Rodrigo et al.[134] introduce self-similar nanorod antenna arrays capable of providing a number of resonances, depending on the number of iterations in the fractal-like generation procedure of this multiresonant nanorod design. Remarkably, the far-field amplitudes of the resonances are relatively homogeneous on an ultrabroad spectral range from near- to mid-IR (Figure 3:9c). Furthermore, each spectral resonance position can be fine-tuned independently with minimal influence on the neighboring resonances.

3.2.4   Plasmonic Nanogap Antennas

The lateral size and geometry of the gap between neighboring antenna elements is another crucial parameter for optimizing sensitivity since it determines the maximum enhancement and confinement of the electric near-fields based on the "lightning rod" effect (i.e., the concentration of field lines near highly curved surfaces or narrow gaps).[138,139] For example, Huck et al.[141] leverage the high field enhancement from the nanogaps formed by dimer rod antennas to sense nanocoatings of CBP molecules with high sensitivity. In Figure 3:10a, it is clearly visible that rod dimers with an 8 nm gap give stronger CBP absorption signals than dimers with a larger gap of 50 nm.

Compared to rod-type structures, bowtie antennas composed of opposing triangular resonators can provide stronger near-field localization,[140] but suffer from lower SEIRA enhancement factors because of additional losses in the wider part of the triangular structure.[142] To combine the advantages of these two geometries, Brown et al. have developed a fan-shaped antenna geometry,[143] consisting of a pair of closely spaced resonant rod-type elements with semicircular ends (Figure 3:10b, left). The authors were able to simultaneously realize strong field confinement and SEIRA enhancement at a resonance frequency of around 3000 cm^{-1} (Figure 3:10b, right), which they utilized for the sensitive detection of self-assembled monolayers of ODT molecules.
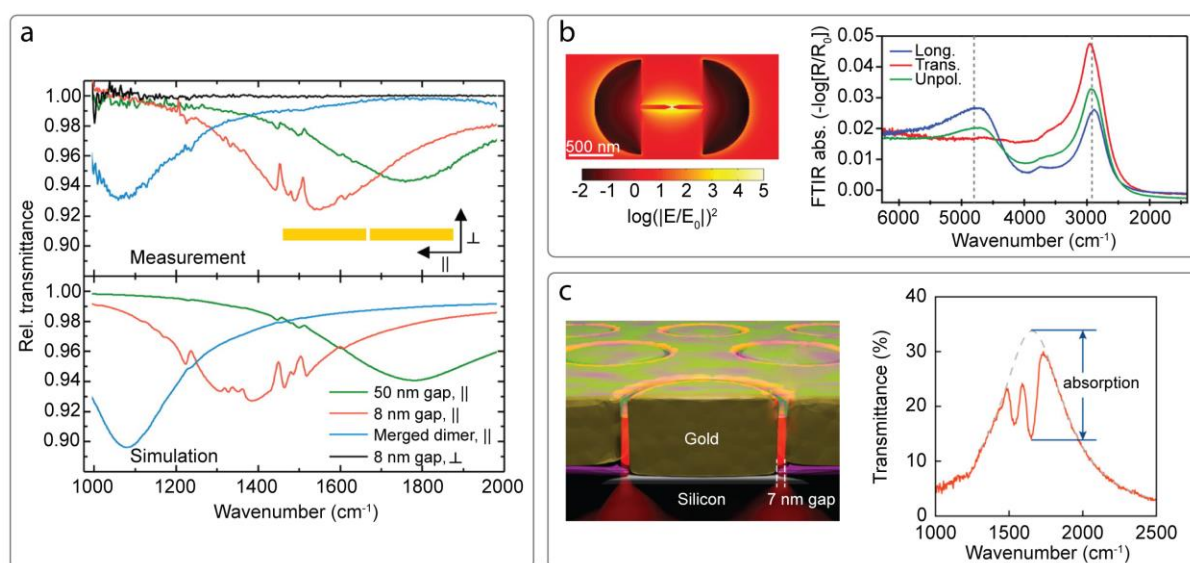
Figure 3:10 Nanogap antennas. a) Experimental (top) and simulated (bottom) transmittance spectra of rod dimers covered with 5 nm-thick CBP layers.[141] b) Electric near-field enhancement (left) and absorbance spectra (right) of Fan-shaped gold structures, which combine rod-type and bowtie antenna shapes for increased sensitivity. Adapted from Ref.[143] Copyright 2015, American Chemical Society. c) Sketch (left) and transmittance spectra (right) of coaxial resonators with sub-10 nm gaps for high-contrast SEIRAS. Adapted from Ref.[144] Copyright 2018, American Chemical Society.

Even higher sensitivities can be obtained by decreasing the distance between antenna elements towards the few-nanometer regime to realize so-called nanogap antennas.[145–147] In a recent example, Yoo et al. realized resonant coaxial nanoaperture structures (Figure 3:10c, left) using atomic layer lithography, which combines atomic layer deposition of a thin sacrificial Al$_2$O$_3$ layer with large-area

photolithography for the high-throughput fabrication of sub-10 nm gaps.[144] The authors found that the coaxial shape of the gaps produced strong and uniform electric near-fields along the side walls of the structure, enabling the detection of large vibrational signals originating from spin-coated silk fibroin molecules (Figure 3:10c, right). Focusing again on rod-type antenna systems, the enhancement effects associated with narrow inter-antenna gaps and the grating modes of the array can be combined in a single nanophotonic geometry as shown by the work of John-Herpin et al., which analyzed and implemented grating-order coupled nanogap (GONG) antenna geometries for high-sensitivity biomolecular detection and protein secondary structure analysis.[148]

Chapter 4   Quantifying the Limits of Detection of Surface-Enhanced Infrared Spectroscopy with Grating Order-Coupled Nanogap Antennas

This work has been published in ACS Photonics, 2018.

Authors: Aurelian John-Herpin, Andreas Tittl and Hatice Altug

Contribution: A. J.-H. designed and numerically simulated metasurfaces, micro-/nano-fabricated chips, designed and performed experiments, carried out data analysis, and wrote the manuscript.

Reference: John-Herpin, Aurelian, Andreas Tittl, and Hatice Altug. "Quantifying the limits of detection of surface-enhanced infrared spectroscopy with grating order-coupled nanogap antennas." ACS photonics 5, no. 10 (2018): 4117-4124.

4.1   Abstract

Infrared spectroscopy is widely used for biomolecular studies, but struggles when investigating minute quantities of analytes due to the mismatch between vibrational cross sections and IR wavelengths. It is therefore beneficial to enhance absorption signals by confining the infrared light to deeply subwavelength volumes comparable in size to the biomolecules of interest. This can be achieved with surface-enhanced infrared absorption spectroscopy, for which plasmonic nanorod antennas represent the predominant implementation. However, unifying design guidelines for such systems are still lacking. Here, we introduce an experimentally verified framework for designing antenna-based molecular IR spectroscopy sensors. Specifically, we find that in order to maximize the sensing performance, it is essential to combine the signal enhancement originating from nanoscale gaps between the antenna elements with the enhancement obtained from coupling to the grating order modes of the unit cell. Using an optimized grating order-coupled nanogap design, our experiments and numerical simulations show a hotspot limit of detection of two proteins per nanogap. Furthermore, we introduce and analyze additional limit of detection parameters, specifically for deposited surface mass, in-solution concentration, and secondary structure determination. These limits of detection provide valuable reference points for performance metrics of surface-enhanced infrared absorption spectroscopy in practical applications, such as the characterization of biological samples in aqueous solution.

4.2   Introduction

Infrared (IR) spectroscopy is a powerful analytical technique that provides remarkable insights into the molecular world. IR light can excite molecular vibrations whose resonance frequencies depend on the chemical nature of the bonds as well as their configuration and surroundings.[149] This technique is particularly useful for investigating the structure and behavior of biomolecules in their native environment, since it operates without the need for extrinsic labels. For instance, in proteins, amide bonds make up the backbone of their structure and can support IR active molecular vibrations such as the amide I and II bands at around 1650 and 1550 cm^{-1}, respectively.[74] These intrinsic labels can be targeted with IR sensors to provide chemically specific detection. Beyond the mere identification of analytes, the amide I absorbance signature can be analyzed to retrieve information about molecular secondary structure and conformation.[150] This information, which can be acquired in real-time, can be enhanced with precise three-dimensional structures of biomacromolecules obtained with complementary techniques such as X-ray crystallography and nuclear magnetic resonance (NMR) spectroscopy.[151]

In order to get relevant insights about biomolecular interactions, it is often crucial to probe them in physiological conditions, that is, at low concentrations in aqueous solution or at the submonolayer level.[152] High sensitivity and water-compatibility requirements can usually not be fulfilled by traditional IR spectroscopy techniques, in which large sample concentrations are necessitated, and strong vibrational bands of water mask much of the proteins' amide I absorption signature, which holds most of the information related to secondary structure.[153] Surface-enhanced IR absorption

spectroscopy (SEIRAS) can overcome these limitations by utilizing resonant nanoantennas, which can strongly enhance the light absorption of near-surface analytes.[107,124,143,154,155] In recent years, the interest in SEIRAS and its application for biological, chemical, and gas sensing has been increasing with the use of plasmonic excitations in metallic and graphene resonators as well as high-Q resonant modes of all-dielectric metasurfaces.[89,156–158] In metallic IR antennas, the incoming light can be coupled efficiently due to the large oscillator strength of localized surface plasmon resonances (LSPR). In contrast to traditional refractometric LSPR sensors, SEIRAS provides chemical and conformational specificity.

In this work, we introduce a plasmonic grating order-coupled nanogap (GONG) design to probe the limits of detection for protein sensing and find that we can detect as little as two proteins per nanogap. To provide reference points for performance metrics of SEIRAS in practical applications, we present additional sensitivity assessment criteria: limits of detection for (i) deposited surface mass, (ii) in-solution concentration, and (iii) secondary structure analysis. We demonstrate the chemically specific detection of proteins in aqueous solution with concentrations as low as 100 pg·mL^{-1} and resolve their secondary structure content with concentrations down to 500 ng·mL^{-1}. Conventionally, the analysis of protein secondary structure using IR absorbance spectroscopy in aqueous solution is very challenging due to interfering water absorbance and requires orders of magnitude higher concentrations with traditional methods.[153] The presented quantitative study of proteins using optimized resonant antennas shows that SEIRAS can achieve limits of detection that are highly competitive with other optical label-free biosensors,[159] with the additional benefits of chemical and conformational specificity.

In our study, gold antennas on an IR-transparent calcium difluoride (CaF$_2$) substrate are implemented, since this material system can provide resonances with large excitation cross sections and strong near-field enhancements required for efficient SEIRAS.[89,135,160] Another advantage of gold is its biocompatibility with well-established surface functionalization protocols. Furthermore, on-chip plasmonic nanoantennas allow for straightforward integration with microfluidics.[60,104,160–163] Regarding resonator shape, nanorods are the most common plasmonic structures for SEIRAS, as they can be tuned to access different spectral ranges and fabricated easily and reproducibly. Their dipolar-like shape makes them inherently efficient at generating high electric near-field enhancements necessary for amplifying molecular vibrations.[164] Given the important role of these antenna systems in SEIRAS, it is important to maximize their sensing performance.

4.3 Results and Discussion

4.3.1 Engineering an Optimized Nanoantenna Array for Protein Sensing

Nanogaps, that is, spacings between plasmonic structures below a hundredth of the excitation wavelength, can generate strong field enhancements[165] and are thus interesting for SEIRAS applications.[141,144,146,147,166,167] Another effective method for increasing sensitivity is to make use of the enhancement originating from grating order coupling.[108,125] Traditionally, plasmonic sensing geometries only focus on optimizing one of these aspects, limiting the available design space. We

present a comprehensive framework for determining an optimal antenna unit cell geometry that efficiently combines these two enhancement methods simultaneously. Specifically, we demonstrate the importance of independently tuning the unit cell x- and y-periodicities to simultaneously achieve analyte-accessible nanogaps and strong grating order coupling Figure 4:1a displays a tilted view of a GONG sensor, which consists of unit cells with nonequal periodicities P_x and P_y, each containing a single rod antenna. As a consequence of this geometrical arrangement, the nanogaps arise between the adjacent unit cells along the x-direction of the array. Figure 4:1b is a schematic of a nanogap with two streptavidin proteins in the electromagnetic hotspot region (nanogap surface). The dimensions of the array parameters can be visualized in Figure 4:1c,d, which showcase SEM micrographs. The gap has a width G = 32 nm and the periodicities are P_x = 1516 nm and P_y = 3204 nm.
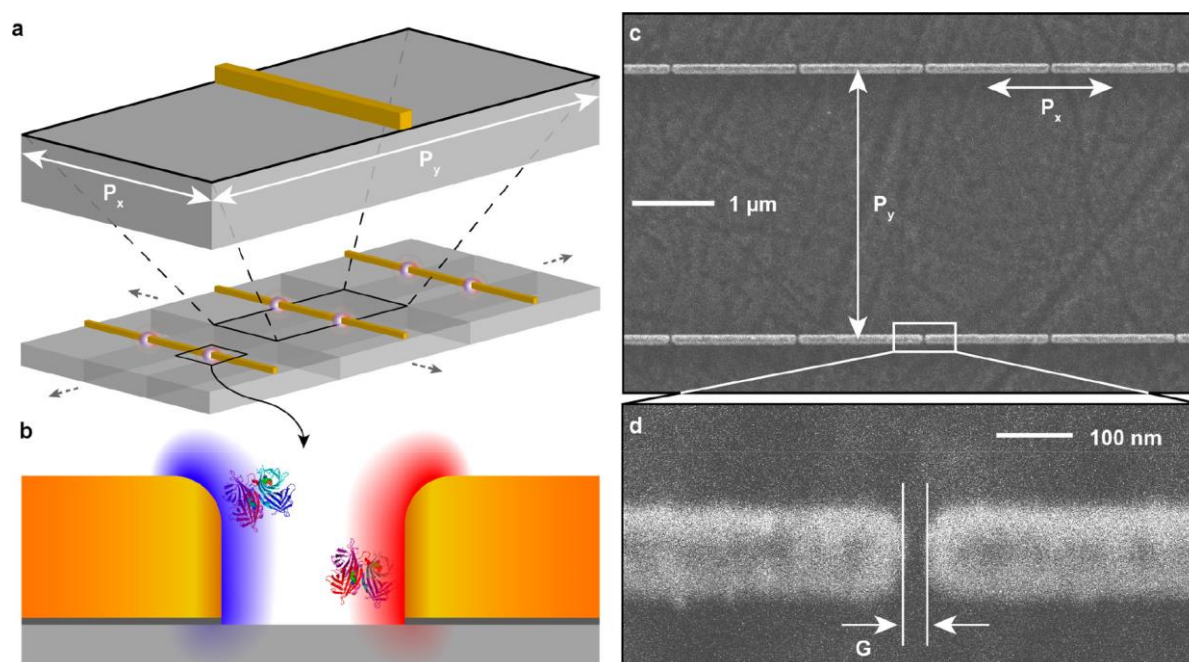
Figure 4:1 Grating order-coupled nanogap (GONG) antennas. a) 3D model of GONG antenna unit cell and array. b) Schematic representing two streptavidin proteins localized in a nanogap hotspot in which the electromagnetic fields are represented in red and blue gradients (not to scale). c) Scanning electron microscope (SEM) image displaying the periodicities P_x and P_y of a GONG array. d) SEM image of a nanogap with a width of G.

We obtained the optimized GONG design by performing extensive numerical simulations in which we vary both the gap size G as well as the strength of the grating order coupling, which is controlled by the parameter P_y. Numerical simulations are performed for multiple GONG designs in a parameter space of gap size and y-periodicity, where each data point is designated by the pair {G, P_y}. Specifically, we focus on gap sizes between 20 and 100 nm, as this encompasses the relevant range for protein studies (Figure 4:2a, bottom). Periodicities are selected so that the associated lowest frequency grating orders are tuned over the resonance frequency of the antennas. We benchmark the performance of these {G, P_y}-sensor designs by comparing their maximum absorbance for a 5 nm thick model protein layer placed on the surface of the nanogaps (Figure 4:2a, top). The protein layer is modeled with custom optical constants in order to have its extinction peak at 1600 cm^{-1}, between the amide I and II bands, and with the nondispersive component of the refractive index equal to 1.
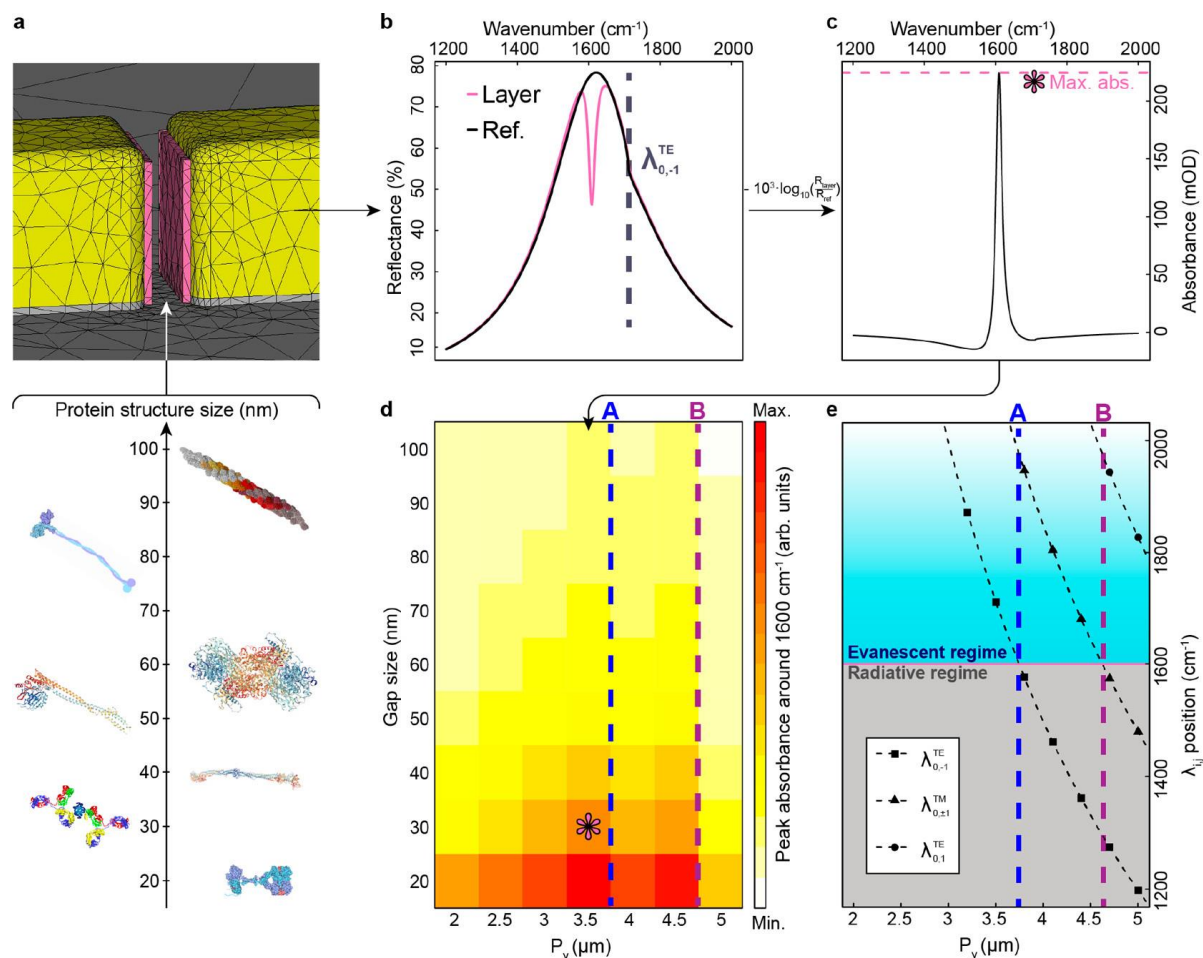
Figure 4:2 GONG sensitivity and gap accessibility. a) Lower panel: Size of exemplary protein structures on a scale from 20 to 100 nm. From smallest to largest: epidermal growth factor (David Goodsell, DOI: 10.2210/rcsb_pdb/mom_2010_6), IgG antibodies sandwiching an antigen, fibrinogen (PDB ID: 1M1J[168]), SMC protein (PDB ID: 5XEI[169]), tripeptidyl peptidase II (PDB ID: 3LXU[170]), kinesin (David Goodsell, DOI: 10.2210/rcsb_pdb/mom_2005_4), and amyloid protofibril (reproduced in part from Vestergaard et al.[171] under the Creative Commons Attribution license, CC BY 4.0). Upper panel: Meshed 3D model of a 30 nm gap with a 5 nm thick model protein film (pink layer) on the nanogap surfaces as used in the numerical simulations. b) Reflectance spectra R_{layer} and R_{ref} obtained from numerical simulations of a {G = 30 nm, P_y = 3.5 μm} sensor with and without model protein layer, respectively. The vertical dashed line at the kink indicates the spectral position of the corresponding grating order. c) Absorbance spectrum calculated from the reflectance spectra given in panel b. d) Heatmap displaying comparative absorbance strength as a function of gap size G and y-periodicity P_y. The asterisk indicates the array parameters used for the calculations in panels a–c. e) Spectral position against P_y for the three lowest frequency grating orders (dashed curves). The two vertical dashed lines labeled A and B indicate the critical periodicities for which each of the two lowest frequency grating orders transitions from high to low frequency side of the near-field resonance peak at 1600 cm^{-1} (pink horizontal line) and thereby causes a transition from evanescent (blue gradient area) to radiative regime (gray shaded area).

Each {G, P_y} sensor is adjusted to provide a near-field resonance maximum at 1600 cm^{-1}, and the structures are then simulated both with and without model protein layer in order to obtain the reflectance spectra (Figure 4:2b), from which we calculate the absorbance spectra (Figure 4:2c). Using

the maximum absorbance of each point of the {G, P_y} parameter space, we generate a heatmap allowing us to compare the performance of the sensors (Figure 4:2d).

This map shows that both the gap size and the y-periodicity strongly influence the performance of the sensors. Notably, for a given gap size, we observe that performance is highest for designs directly to the left of the dashed lines A and B. This behavior can be understood by considering the position of the lowest frequency grating modes with respect to the localized resonance frequency of the antennas. These grating orders $\lambda_{i,j}$ are commonly accessed at the conditions of i = 0 and j = ±1 and can be described by the following equations derived from previous works:[127,172]

$$\lambda_{0,\pm 1}^{TM} = P_y \cdot \sqrt{n_s{}^2 - \sin^2\theta}$$

$$\lambda_{0,\pm 1}^{TE} = P_y \cdot (n_s \mp \sin\theta)$$

Equations 4:1 – Grating orders

Here, n_s is the refractive index of the antennas' surroundings, θ is the incident light's inclination angle, TE corresponds to transverse electric, and TM corresponds to transverse magnetic light polarization (see section 4.5.1 for more details). These equations confirm that only the y-periodicity of the GONG unit cell needs to be tuned in order to achieve strong coupling to the grating order at the lowest frequency. Consequently, P_x could be freely adjusted to achieve a desired nanogap size G and resonance position, which can be tuned by choosing the right antenna length L. This results in the following condition for the x-periodicity of the GONG unit cell:

$$P_x = L + G$$

Equation 4:2 – x-periodicity condition

Using Equations 4:1 and Equation 4:2, we can plot the grating order positions as a function of P_y (Figure 4:2e). We observe that the lines A and B correspond to the periodicities for which the grating orders $\lambda_{0,-1}^{TE}$ and $\lambda_{0,\pm 1}^{TM}$, respectively, transition from the high frequency to the low frequency side of the antenna's localized resonance at 1600 cm^{-1}. Therefore, to maximize both far-field and near-field responses, we need to place the grating orders with the lowest frequencies directly at the high frequency side of the antenna far-field resonance in order to ensure that the antennas are in an evanescent regime, that is, their interacting electric field components add in phase to reduce the amount of energy that can escape the array as electromagnetic radiation.[108]

For increasing y-periodicity from 2 to 3.5 µm, the position of the lowest frequency grating order, that is, $\lambda_{0,-1}^{TE}$, approaches the resonance from the high frequency side (Figure 4:2e), until it reaches 1711 cm^{-1}, as can be seen as a kink in the reflectance curve in Figure 4:2b (indicated by the vertical dashed line). The array is thus in a purely evanescent regime, as opposed to the case when P_y = 4 µm, for which the position of $\lambda_{0,-1}^{TE}$ moves to the low frequency side of the far-field resonance (Figure 4:2e), thereby dampening the resonance in the TE channel and consequently decreasing the sensor's

overall response (Figure 4:2d). For P_y = 4.5 µm, the position of $\lambda^{TE}_{0,-1}$ is further in the radiative regime area, but now we also observe $\lambda^{TM}_{0,\pm1}$ at 1644 cm^{-1}, that is, positioned at the high frequency side of the antenna resonance (Figure 4:2e). This yields an overall high performance of the sensor, however, not as high as for P_y = 3.5 µm. For P_y = 5 µm, the array is in a highly radiative regime which explains the drastically weakened sensor performance observed for the sensors featuring this y-periodicity value.

Within the explored parameter space, the sensor {G = 20 nm, P_y = 3.5 µm} yields the best performance for protein measurements. Consequently, we choose antenna parameters in the direct vicinity of this combination to obtain a high-performance sensor compatible with practical considerations regarding nanofabrication reproducibility and the size of the biomacromolecules. In particular, a gap size of 32 nm is chosen to accommodate a wider range of biomolecules with dimensions above 20 nm, such as antibodies sandwiching an antigen (Figure 4:2a), thus making our design broadly applicable to the study of proteins. Another parameter that influences the performance of antenna-based sensors is the decay characteristics of the electromagnetic near-fields around the hotspots. Through full-wave simulations of the electromagnetic fields, we have estimated the decay length as 125 nm for a {G = 32 nm, P_y = 3204 nm}-GONG sensor (Figure 4:9b). This decay range makes the sensors effective for probing a large range of analyte molecules and changes in the environment.

4.3.2   Benchmarking Sensing Performance in Dry Conditions

In the following biomolecular studies in dry conditions, {G = 32 nm, P_y = 3204 nm}-GONG arrays with a size of 200 × 200 µm^2 are used for absorbance measurements using Fourier-transform infrared (FTIR) spectroscopy. To assess the performance of this optimized design for the detection of protein submonolayers, we perform experiments in which minute quantities of proteins are bound onto the antennas. Specifically, a piezoelectric microdispenser is used to spot droplets of controlled volume containing precise quantities of streptavidin in phosphate buffered saline (PBS) onto the antenna arrays (Figure 4:3a). The dispenser is equipped with a side camera to accurately measure the droplet size to be spotted on a specific region and by using this volume and the number of droplets being spotted, the total mass deposited on each sensor is controlled. Prior to spotting, the antenna surfaces are functionalized using biotinylated thiols. This allows us to probe the limit of amide I absorbance detection for specifically bound proteins on GONG arrays tuned to have their near-field resonance peaks at the amide I absorbance peak (Figure 4:3a).
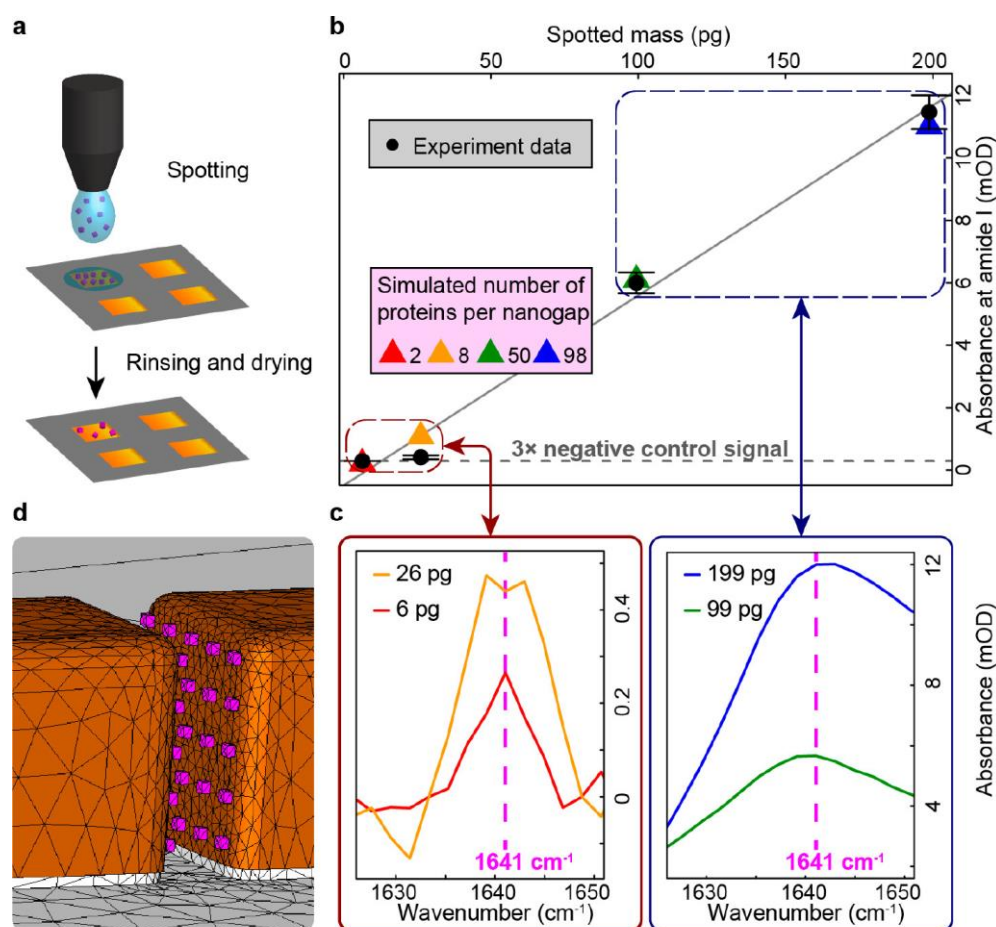
Figure 4:3 Dry protein measurements with GONG sensors. a) Schematics depicting the experimental procedure for the preparation of chips with bound streptavidin proteins (not to scale) with the use of a microspotting dispenser. b) Plot in which the black data points correspond to the experimentally measured absorbance at the amide I peak for different amounts of spotted protein mass. The colored triangular data points correspond to absorbance at the amide I peak obtained via simulations with different numbers of proteins per nanogap. c) Exemplary absorbance curves which showcase the amide I peak. d) 3D model of the simulation strategy followed to obtain the triangular data points shown in the plot of panel b. The streptavidin proteins were homogeneously distributed in the nanogaps and modeled as $4 \times 5 \times 5$ nm^3 blocks with optical constants extracted from infrared reflection absorption spectroscopy (IRRAS) measurements (Figure 4:7b).

Figure 4:3b displays absorbance at the amide I peak against the spotted protein quantity. For spotted masses of 99 and 199 pg, the observed amide I absorbance is very strong compared to the noise level, but for spotted masses of 6 and 26 pg, we only observe the amide I absorbance peak at 1641 cm^{-1}, just above three times the negative control signal level (Figure 4:3c). By using a surface-functionalization protocol, we ensure that our measured signals originate from specifically bound proteins. It is important to note that the measured surface masses are lower than the spotted mass quantities due to the thorough rinsing steps after incubation of the protein solutions. Thus, these values are conservative estimates and the measured signals should be generated from even lower quantities of analytes. Next, we correlate our measured signals with the corresponding number of proteins per nanogap using numerical simulations. We model the streptavidin proteins as blocks of $4 \times 5 \times 5$ nm^3, in agreement with reported streptavidin volumes[173,174] and use optical constants

extracted from IRRAS measurements (Figure 4:3b). In order to not overestimate the sensitivity of our sensors, we introduce a 1 nm thick layer with refractive index of 1.4 in between the antenna surface and the protein blocks to model the biotinylated thiol layer. Furthermore, we do not locate the blocks at the positions of the highest field enhancement, that is, the rounded corners and antenna/substrate intersections, but rather homogeneously space them on the gap surface (Figure 4:3d). Given that our antennas have a gap cross section of 100×100 nm^2, a maximum of approximately 800 proteins can be bound per nanogap surface area. We find that the numerical simulations for this case match the experimentally measured maximal signals very well, and similar results are obtained in the case of complete antenna coverage with a streptavidin layer (Figure 4:3c). This confirms that the simulations are in line with our measurements and that the signal predominantly originates from proteins within the gaps. From simulations with less than 800 proteins per nanogap, we can infer that measurements with spotted quantities of 199, 99, 26, and 6 pg correspond to approximately 128, 50, 8, and 2 proteins per nanogap.

4.3.3   Benchmarking Sensing Performance in an Aqueous Medium

Protein studies are usually conducted in solutions in order to maintain their native conformational state and biological function, therefore it is also crucial to establish the concentrations required for protein detection and secondary structure analysis in aqueous media. To perform in-solution absorbance measurements, we use {G = 32 nm, P_y = 3264 nm}-GONG arrays with a size of 200×200 μm^2.

Since our CaF$_2$ substrate is highly transparent in the mid-IR range, we can illuminate our chips from the backside and integrate them within custom-made microfluidic devices, as shown in Figure 4:4a. By injecting streptavidin at increasing concentrations, we can establish the curve shown in Figure 4:4b. We chose this additive injection method due to the strong streptavidin–biotin interaction, which prohibits surface regeneration. The obtained S-shaped curve covers a large concentration range from 100 pg·mL^{-1} to 100 μg·mL^{-1}. We fit the data using a Hill equation-derived fit, which empirically describes the correlation between the absorbance response A of the biosensor and the concentration C of the analytes in aqueous solution:

$$\text{A}(C) = A_{min} + \frac{A_{max} - A_{min}}{1 + 10^{n \cdot (C_{0.5} - C)}}$$

Equation 4:3 – Hill equation-derived absorbance against concentration fit

Here, A_{min} and A_{max} correspond to the minimum and maximum absorbance signals, $C_{0.5}$ represents the concentration, which yields $\frac{A_{max}}{2}$, n is an exponent that is related to binding cooperativity, similarly to the Hill coefficient.[175,176] In our case, we have n < 1 in accordance with the expected negative cooperative binding behavior. The inset of Figure 4:4b shows a zoomed linear plot for the lowest concentrations ranging from 100 pg·mL^{-1} to 1 ng·mL^{-1}. The absorbance signal from an injection of 100 pg·mL^{-1} streptavidin corresponds to approximately three times the absorbance signal from the

injection of analyte-devoid buffer (negative control) and, thus, we can infer that our limit of detection is around 100 pg·mL^{-1}.
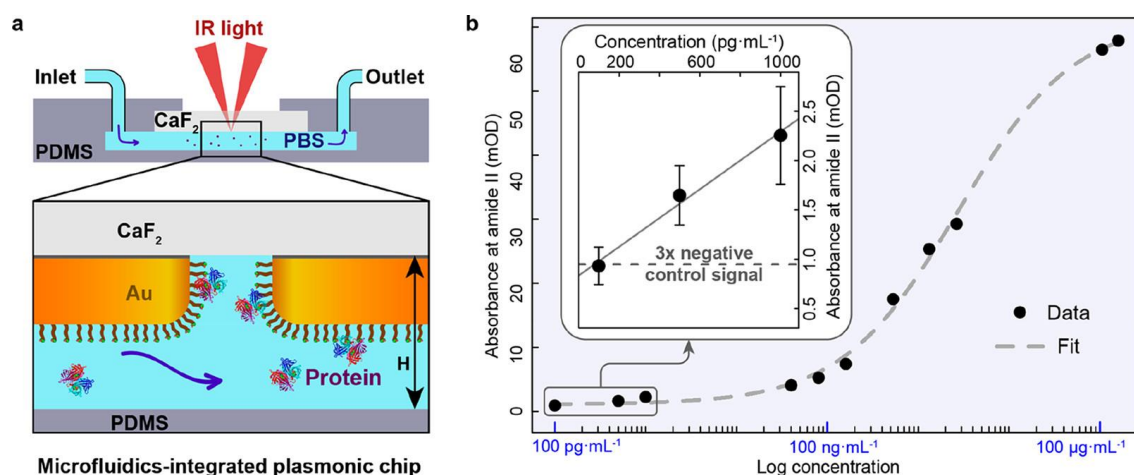
Figure 4:4 Aqueous protein measurements with GONG sensors. a) Schematic of the in-solution experimental setup with the fluidic inlet and outlet as well as the optical path (not to scale). The flow channel height H of the polydimethylsiloxane (PDMS) device is 30 µm. The zoomed schematic displays functionalized gold antennas displaying biotin groups and the captured proteins from the flowing solution. b) Plot of absorbance at the amide II peak for different concentrations of streptavidin. A linear fit is displayed in the inset and a fit using Equation 4:3 is displayed in the logarithmic plot.

4.3.4 Secondary Structure Analysis of Proteins

Using the same experimental data set, we can also estimate the concentration limit for secondary structure analysis. Information regarding the secondary structure of proteins is of great interest for unravelling complex biological processes[177] such as protein misfolding, which play a major role in diseases including Alzheimer's and Parkinson's disease.[178] Conventional IR spectroscopy of proteins in aqueous solution typically requires concentrations > 10 mg·mL^{-1}, which can be very challenging for the study of aggregation-prone proteins and peptides as well as rare samples.[153] It is thus of great interest to find new methods that can reduce the necessary concentrations for IR spectroscopy of proteins in aqueous solution.[179] In fact, it has recently been shown in a pioneering work that the secondary structure of the protein α-synuclein, which is involved in Parkinson's disease, can be analyzed in aqueous solution and in real-time using nanorod antennas.[162] The amide I band of proteins mainly arises from the C=O stretching of its backbone. This backbone configuration will influence the observed amide I absorbance spectrum as a consequence of transition dipole coupling between the different amide group oscillators and the particular hydrogen bonding patterns. Consequently, amide I absorbance spectra result from the superposition of sub-bands associated with different secondary structures present in a particular protein.

The secondary structure content of tetrameric streptavidin extracted from the current Uniprot database is 47.5 % β-strands, 22.4 % disorder, 11.5 % helices, and 18.5 % loops and turns. The deconvolution of the absorbance spectrum obtained for a submonolayer of streptavidin in aqueous solution (Figure 4:5a), which was obtained upon injection of 2.65 µg·mL^{-1}, yields a secondary structure content which agrees well with the database values, that is, we obtain 53.5 % β-strands, 16.9 %

disorder, 11.3 % helices, and 18.3 % loops and turns. Noticeably, we observe two bands for the helices centered at 1650 and 1666 cm^{-1}, which are known to correspond to regular α-helices and 3_{10}-helices, respectively (Table 4:1). Furthermore, since in the literature the spectral position of turns tends to be reported at slightly higher wavenumbers than the spectral position of loops, we refine our analysis by associating the band at 1674 cm^{-1} with loops and the band at 1679 cm^{-1} with turns. This yields contents of 6.6 %, 4.7 %, 11.1 %, and 7.2 % for 3_{10}-helices, α-helices, loops, and turns, respectively. These values are in good agreement with the average values calculated from Meskers et al.[180]: 55.5 % β-strands, 19.4 % disorder, 5.8 % 3_{10}-helices, 2.5 % α-helices, 12.3 % loops, and 4.5 % turns.

secondary structures	band positions (cm^{-1})
antiparallel β-strands	1629, 1639, 1693, 1696
disorder	1643
helices	1650, 1666
loops and turns	1674, 1679

Table 4:1 Secondary Structure Absorption Band Positions.[74,150]
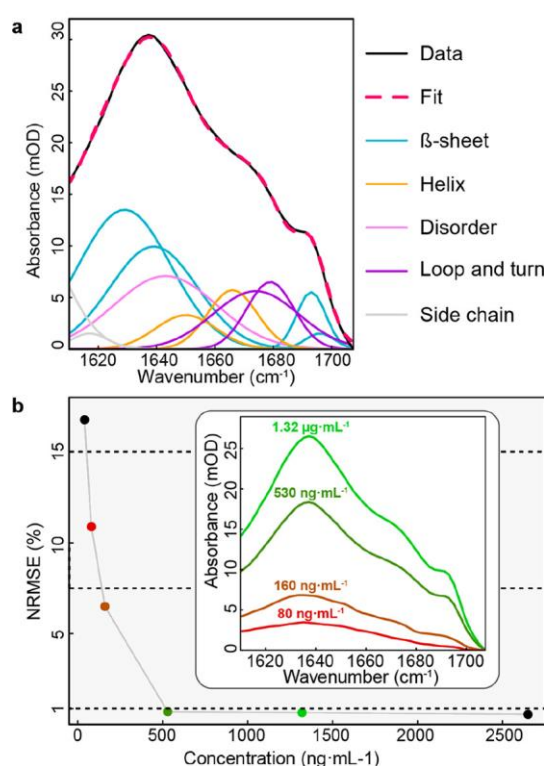
Figure 4:5 Secondary structure measurements with GONG sensors. a) Deconvoluted absorbance spectrum of a submonolayer of streptavidin in aqueous solution at a concentration of 2.65 µg·mL^{-1} for quantitative identification of different secondary structure motifs, which are listed in the legend on the side. The pink dotted curve corresponds to the sum of Gaussian peaks which were used for fitting the experimental data (solid black curve). b) The procedure shown in panel (a) is used to obtain the NRMSE for the experimental absorbance spectra at lower concentrations (colored dots) with respect to the (scaled) fit of the absorbance spectra shown with colored curves in the inset. The black dot with the lowest NRMSE corresponds to the data shown in panel (a).

By calculating the normalized root-mean-square error (NRMSE) for the spectra obtained for lower concentrations (Figure 4:5b) with respect to our scaled fit (Figure 4:5a), we see that we can retrieve the secondary structure content with high accuracy down to 530 ng·mL^{-1}, where the NMRSE remains

below 1 %. For 160 ng·mL^{-1}, the NMRSE falls in the range 1–7.5 %, which still allows for secondary structure analysis but with reduced accuracy. For 80 ng·mL^{-1} the NMRSE is in the range 7.5–15 %, in which it is no longer possible to reliably quantify the complete secondary structure content. Nonetheless, it is still possible to retrieve the amide I peak position, which can be used to draw qualitative conclusions on the dominant secondary structure motif (antiparallel β-sheet in our case). Such information can provide important insights into biological processes, for example, as a means to diagnose prodromal Alzheimer's disease.[181]

4.4   Conclusion

Even though our GONG design provides high sensitivities down to ng·mL^{-1} and pg·mL^{-1} levels, its performance could still be boosted if an increase in structural complexity is acceptable. For instance, it has been shown that the access of the enhanced near-fields to the target analyte can be increased by placing the plasmonic antennas on pedestals.[120,182] Furthermore, in situations where a more spatially homogeneous near-field enhancement distribution is desired, other plasmonic designs such as ones based on annular gaps could be implemented.[144]

In conclusion, we have introduced a framework for designing optimized nanogap arrays as well as assessing their performance for SEIRAS of minute quantities of biomolecules. We have used the optimized arrays for protein experiments and have shown that concentrations as low as 100 pg·mL^{-1} can be detected in aqueous solution using protein-specific absorbance signals and that the secondary structure can be accurately retrieved at concentrations on the order of 500 ng·mL^{-1}. Our results emphasize the potentials of SEIRAS and nanoplasmonics for protein studies, as traditional IR spectroscopy would require orders of magnitude higher concentrations. In addition to protein analysis, GONG arrays can be adapted to the study of other classes of biomolecular systems such as lipid vesicles and exosomes, which currently attract significant interest due to their relevance to health and disease (section 4.5.8). In this context, it has recently been shown that nanophotonic platforms based on metallic rods can resolve complex interaction processes in vesicular systems, such as the toxin-induced release of neurotransmitter molecules from synaptic vesicle mimics.[160] The versatility of nanorod antennas for the study of a broad range of biological samples combined with the optimization principles presented in this work opens up exciting new applications in fields such as diagnostics and pharmacology.

4.5 Supplementary Information

4.5.1 Analytical Calculations
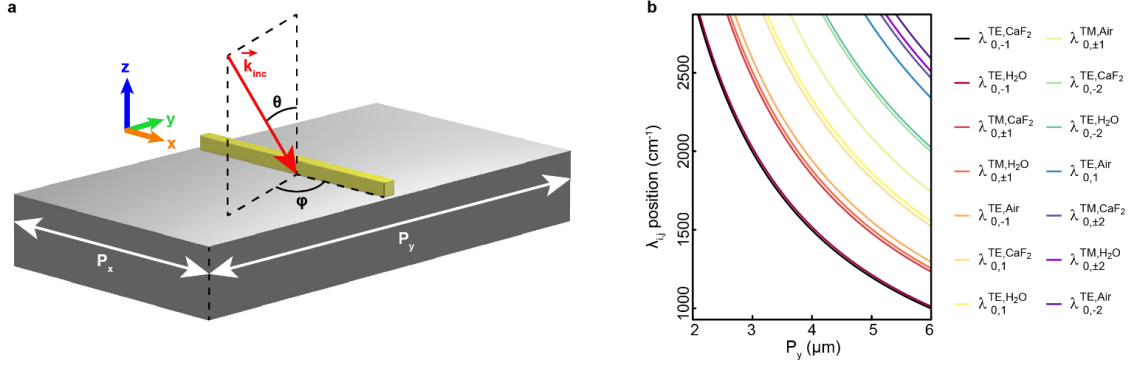
Figure 4:6 GONG unit cell and GOs. a) Schematic of GONG unit cell. b) Grating orders for $P_x \leq 2$ μm.

Equations 4:1 shown in the main text are derived from the phase-matching condition:[110]

$$\overrightarrow{k_s} = \overrightarrow{k_{inc}} \cdot \sin\theta + i \cdot \overrightarrow{G_x} + j \cdot \overrightarrow{G_y}$$

Equation 4:4 – Phase matching condition

Where θ and φ are the incident light's inclination and azimuthal angles (Figure 4:6a), respectively, $\overrightarrow{k_s}$ is the tangential momentum of the surface-propagating waves in the medium 's' and $\overrightarrow{k_{inc}}$ is the momentum of the freely propagating incident light in the medium 'inc'; $i \cdot \overrightarrow{G_x}$ and $j \cdot \overrightarrow{G_y}$ correspond to the lattice momenta in x- and y-direction, respectively, with the integers $i = 0, \pm 1, \ldots$ and $j = 0, \pm 1, \ldots$, defining the different grating orders. Using the following relations:

$$\frac{|\overrightarrow{k_{inc}}|}{n_{inc}} \cdot \lambda_{i,j} = \frac{|\overrightarrow{k_s}|}{n_s} \cdot \lambda_{i,j} = |\overrightarrow{G_x}| \cdot P_x = |\overrightarrow{G_y}| \cdot P_y = 2\pi$$

Equation 4:5 – Momentum relations

We can rewrite Equation 4:4 as:

$$\left(\frac{n_s}{\lambda_{i,j}}\right)^2 = \left(\frac{n_{inc}}{\lambda_{i,j}} \cdot \sin\theta \cdot \cos\varphi + \frac{i}{P_x}\right)^2 + \left(\frac{n_{inc}}{\lambda_{i,j}} \cdot \sin\theta \cdot \sin\varphi + \frac{j}{P_y}\right)^2$$

Equation 4:6 – Phase matching condition-derived equation

The equation for the spectral positions $\lambda_{i,j}$ of the GOs follows as:

$$\lambda_{i,j} = -A_{i,j} + \sqrt{A_{i,j}^2 - B_{i,j}}$$

Equation 4:7 – Spectral positions of the GOs

With:

$$A_{i,j} = \frac{n_{inc} \cdot \sin\theta \cdot \left(\cos\varphi \cdot \frac{i}{P_x} + \sin\varphi \cdot \frac{j}{P_y}\right)}{\left(\frac{i}{P_x}\right)^2 + \left(\frac{j}{P_y}\right)^2} \quad and \quad B_{i,j} = \frac{n_{inc}^2 \cdot \sin^2\theta - n_s^2}{\left(\frac{i}{P_x}\right)^2 + \left(\frac{j}{P_y}\right)^2}$$

Equations 4:8 – Definition of factors $A_{i,j}$ and $B_{i,j}$

In Figure 4:6b we display the grating order curves obtained from Equation 4:7 and Equations 4:8. Setting n_{inc} = 1, i = 0, j = ± 1, as well as φ = 0 and φ = π/2 for the TM and TE cases, respectively, we obtain Equations 4:1.

4.5.2   Numerical Simulations

The far- and near-field spectra of the nanoantenna structures are calculated using numerical simulations performed with CST Microwave Studio's finite integration solver. The CaF$_2$-supported antennas are modelled as 100 nm Au on 5 nm Cr represented as rectangular boxes with blended edges using a radius of curvature of 11 nm and meshed using tetrahedrons. In accordance with the numerical aperture of the Cassegrain objective used in the experiments, the structures are excited by an electromagnetic plane wave incident at an inclination angle θ of 16.7° on the array unit cell defined by P$_x$ and P$_y$. The scattering properties of the structure are calculated as the average of the response to a TM excitation along the y-direction, which is perpendicular to the long antenna axis, and the response to a TE excitation along the x-direction, which is parallel to the long antenna axis. The optical constants for the Au and Cr layers were taken from Olmon et al.[183] and Rakić et al.[184], respectively. The refractive index of CaF$_2$ was set to 1.38, in accordance with values reported by Li.[185]

For the simulation study presented in Figure 4:2, the optical constants displayed in Figure 4:7a below were used for the model protein layer. These values are derived from a Lorentzian model with a resonance frequency of 1600 cm^{-1}, an absorption line strength of 200 cm^{-1} and a damping rate of 100 cm^{-1} (similar to the values reported by Rodrigo et al.[186]). The nondispersive component of the refractive index is set to 1 to avoid the shifting of the sensors' resonance upon addition of the layer. This strategy allows us to generalize our sensor performance benchmarking procedure and thereby increase the accuracy of the sensor comparison. The simulation results featured in Figure 4:3 are based on the optical constants displayed in Figure 4:7b. These values were extracted from IRRAS measurements of a monolayer of streptavidin, following the procedure reported by Rodrigo et al.[186] The protein materials used in the simulations were placed exclusively on the gap surfaces, as we observe that proteins placed on other parts of the antenna surfaces only negligibly contribute to the total IR absorbance (Figure 4:9c). Thereby, we were able to increase numerical simulation efficiency and accuracy by improving the mesh resolution in this area of the antenna geometry.
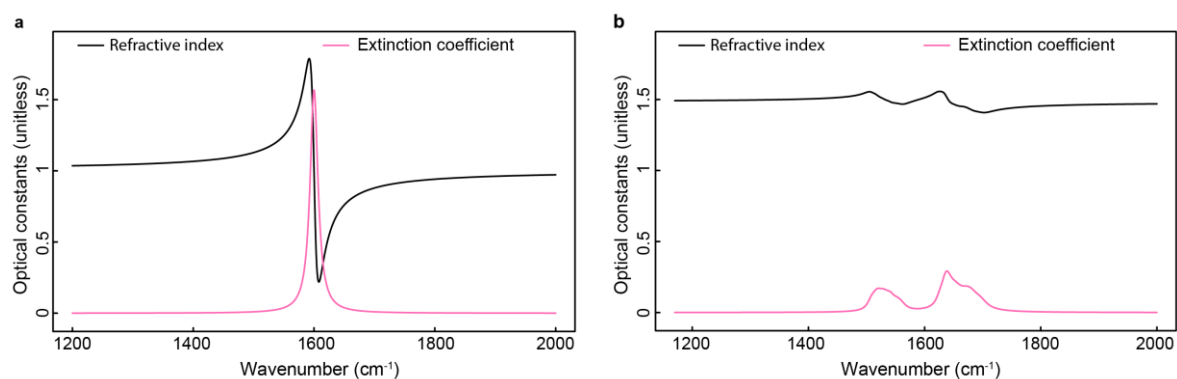
Figure 4:7 Optical constants of streptavidin. Refractive index and extinction coefficient used in the numerical simulations for (a) the model protein layer and (b) streptavidin.

4.5.3 Micro-/Nanofabrication

For plasmonic chip nanofabrication, CaF_2 substrates were cleaned with RCA1 solution ($5:1:1 \cdot H_2O/NH_4OH/H_2O_2$) followed by a sonicated acetone bath. The clean substrates were then spin coated with low and high molecular weight poly(methyl methacrylate) electron beam resist and sputter-coated with a thin Au layer to avoid electron charging during the subsequent exposure step with 100 keV electron beam lithography. The thin gold layer was then wet etched with a solution consisting of $25 \, g \cdot L^{-1}$ KI and $12 \, g \cdot L^{-1} \, I_2$ and the exposed resist was developed with a solution of MiBK:IPA 1:3. 100 nm of Au on 5 nm of Cr were then deposited using electron beam evaporation followed by wet-chemical liftoff in acetone. To remove resist residues, the chips were then subjected to a heated bath of Microposit Remover 1165 solution under sonication as well as an oxygen plasma treatment. The arrays have sizes of $200 \times 200 \, \mu m^2$, with antenna widths of 100 nm and lengths of 1156 nm for the in solution measurements and 1484 nm or 1452 nm for the dry measurements.

For microfluidic device fabrication, a mold was prepared from a Si wafer. The wafer was first spin coated with photoresist and subsequently exposed using direct laser writing. The exposed resist was then developed before dry etching the patterned Si wafer to achieve a channel depth of 30 μm and finally the resist was stripped with an oxygen plasma treatment. The Si mold as well as a mold obtained by xurography were then used to fabricate the PDMS devices for in solution SEIRAS experiments.

4.5.4 Chip Functionalization

The chips were functionalized by incubating them for at least 12 hours in a solution of at least 1.5 mM biotinylated thiols (HS-C11-EG3-Biotin, ProChimia Surfaces) in ethanol. For IRRAS measurements, biotinylated silicon chips coated with 100 nm Au on 5 nm Cr were incubated with 3 μM streptavidin (Thermo Fisher Scientific) in phosphate buffered saline (PBS) for 1.5 hours and then rinsed with PBS solution containing 0.05 % (wt/vol) polysorbate 20 (Tween 20, Sigma Aldrich) (PBST) to remove non-specifically bound proteins and then further rinsed with milli-Q water. Different amounts of streptavidin were bound onto the plasmonic arrays used for the measurements in dry conditions by spotting controlled quantities of streptavidin in 7.5 nL drops of PBS with a piezoelectric microdispenser (SciFLEXARRAYER S3, Scienion) solution. The buffer solution was supplemented with

2 % (wt/vol) glycerol to prevent evaporation during the one and a half hour of post-spotting incubation. The chips were then rinsed with PBST to remove non-specifically bound proteins and further rinsed with milli-Q water.

4.5.5   Infrared Measurements

Infrared spectral measurements were carried out with a Bruker Hyperion 3000 microscope coupled to a Bruker Vertex Fourier-transform infrared spectrometer at a resolution of 4 cm^{-1}. All SEIRAS measurements were performed in reflection mode with a Cassegrain objective (NA = 0.4, 15 × magnification, 9.8°-23.6° angular spread), a knife-edge aperture adjusted to match the array sizes of 200 × 200 μm^2, and polarization along the antennas' long axes. Measurements in dry conditions were done with 256 scans per spectrum and in solution measurements were performed with 128 scans per spectrum. The plasmonic chips were placed in the microscope's sample compartment subjected to continuous purging with dry air, while the chips for IRRAS measurements were placed in the spectrometer's sample compartment which was under vacuum during the measurements. IRRAS measurements were carried out with TM light incident at a grazing angle of 80°.

4.5.6   Data Analysis

Extraction of the protein IR fingerprints is performed by normalizing the reflectance spectrum R of the sensor to that of the functionalized sensor R_0 before analyte injection or spotting (Figure 4:8a, b). The differential absorbance spectrum is calculated by subtracting a polynomial baseline fitted by least-squares method to the normalized reflectance[160] (Figure 4:8b, c). We calculate the noise levels using negative controls, i.e. from three times the absorbance signals generated by the injection or spotting of analyte-devoid buffer solution. All error bars represent the standard error of the mean from two measurements.
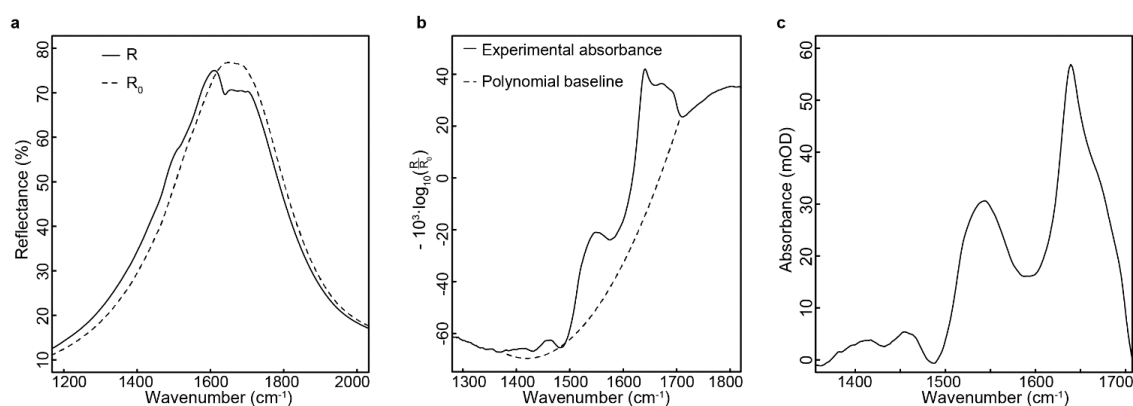
Figure 4:8 Reflectance to absorbance spectra. a) Experimental reflectance spectra taken before and after binding of a streptavidin monolayer to a functionalized {G = 32 nm, P_y = 3204 nm, L = 1484 nm}-GONG sensor. b) Normalized reflectance with polynomial baseline fit. c) Baseline-corrected absorbance.

Secondary structure analysis was carried out using a linear combination of Gaussians to model the measured absorbance spectrum and following the guidelines by Yang et al.[150] First, we determine the

spectral positions of the Gaussians by calculating the second derivative spectrum using the Savitzky-Golay filter and applying nonlinear least-squares fitting using the Levenberg-Marquardt algorithm. We then use the determined central frequencies of the Gaussians to fit the absorbance spectrum and eventually integrate the areas under the Gaussian curves to retrieve secondary structure content.

4.5.7 Experimental Data vs. Numerical Simulations
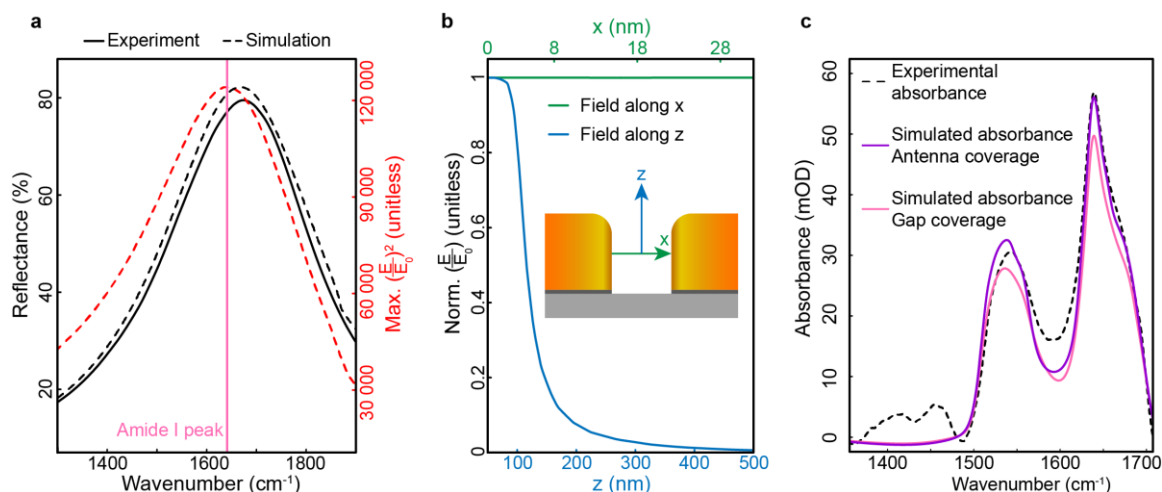
Figure 4:9 Experimental and simulated results for a GONG sensor with the parameters {G = 32 nm, P_y = 3204 nm, L = 1484 nm}. a) Reflectance and maximum near-field intensity enhancement. b) Normalized electric field enhancements along the x- and z-directions, which are represented by the green and blue arrows in the inset schematic, respectively. The green arrow extends from center to center of the gap surface cross sections and the blue arrow has its origin at the center of the gap on the substrate and extends upward perpendicular to the substrate. c) Absorbance for a monolayer of streptavidin. Both the case of full antenna as well as gap-only coverage is simulated.

We compare both experimental reflectance and absorbance spectra from experiments in dry conditions with spectra obtained using numerical simulations and observe a good agreement (Figure 4:9). The numerical simulations also reveal that we have a maximum electric near-field intensity enhancement on the order of 10^5 at the amide I band (Figure 4:9a), that the electric field decay length is on the order of 125 nm (Figure 4:9b) and that approximately 90 % of the absorbance signal comes from analytes located within the antennas' nanogaps (Figure 4:9c).

4.5.8 Applying the GONG Design Principles to Other Molecular Analytes

In this section, we will outline how to adjust the GONG array parameters for the sensing of analytes different than proteins. To give a concrete example, we will choose exosomes as the targeted analytes. Exosomes are an important class of lipid vesicles and thus abundantly contain lipid molecules, which can be targeted by the GONG sensor. Lipids have their strongest IR absorption bands around 2900 cm^{-1} and consequently, this is where the near-field resonance of the GONG array should be set. The y-periodicity needs to be tuned so to have strong grating order coupling, which can be achieved by placing the lowest frequency grating order directly on the high frequency side of where the sensor resonance will be. If we choose to place this grating order at 3100 cm^{-1} and consider Θ = 16.7° as well

as $n_s = 1.41$, than Equations 4:1 yields $P_y \approx 1900$ nm. In order to choose an adequate gap size, we need to consider the size of exosomes, which is usually reported to be between 30 and 100 nm. Accordingly, if we set G = 100 nm, the sensor should be accessible to most analytes. With the parameters P_y and G set, the antenna length can now be tuned so to have the near-field resonance coincide with the position of the IR bands around 2900 cm^{-1}. Using numerical simulations we obtain L = 934 nm. The x-periodicity is determined by Equation 4:2: P_x = L + G = 1034 nm. The numerically simulated reflectance spectrum for this {G = 100 nm, P_y = 1900 nm}-GONG sensor is displayed in Figure 4:10a. To demonstrate the lipid sensing capability of this sensor, we create a model of a single lipid vesicle within a nanogap (Figure 4:10b) and numerically simulate the resulting absorbance spectrum (Figure 4:10c). The lipids' symmetric and asymmetric CH$_2$ stretching bands are clearly visible.
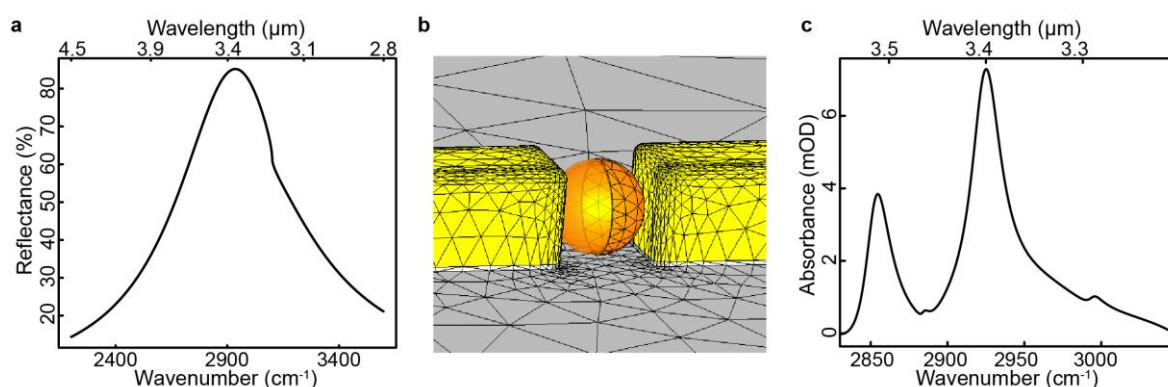
Figure 4:10 Numerical simulations with a GONG lipid sensor with the parameters {G = 100 nm, P_y = 1900 nm}. a) Reflectance spectrum. b) Meshed model of a single nanogap-entrapped lipid vesicle with a diameter of 100 nm and a bilayer thickness of 6 nm. The DOPC optical constants reported in Zawisza et al.[187] where used for this lipid vesicle model. Half the vesicle is displayed as partially transparent instead of the opaque meshed surface in order to visualize that the vesicle is hollow. c) Absorbance spectrum of the nanogap-entrapped lipid vesicle.

Chapter 5 Resolving Molecule-Specific Information in Dynamic Lipid Membrane Processes with Multiresonant Infrared Metasurfaces

This work has been published in Nature Communications, 2018.

Authors: Daniel Rodrigo, Andreas Tittl, Nadine Ait-Bouziad, Aurelian John-Herpin, Odeta Limaj, Christopher Kelly, Daehan Yoo, Nathan Wittenberg, Sang-Hyun Oh, Hilal Lashuel and Hatice Altug

Contribution: A. J.-H. designed and performed SEIRA, IRRAS, SPR and fluorescence experiments, micro-/nano-fabricated chips, carried out data analysis, and co-wrote the manuscript.

Reference: Rodrigo, Daniel, Andreas Tittl, Nadine Ait-Bouziad, Aurelian John-Herpin, Odeta Limaj, Christopher Kelly, Daehan Yoo et al. "Resolving molecule-specific information in dynamic lipid membrane processes with multi-resonant infrared metasurfaces." Nature communications 9, no. 1 (2018): 1-9.

Permission to reproduce the article is granted by Springer Nature.

5.1   Abstract

A multitude of biological processes are enabled by complex interactions between lipid membranes and proteins. To understand such dynamic processes, it is crucial to differentiate the constituent biomolecular species and track their individual time evolution without invasive labels. Here, we present a label-free mid-infrared biosensor capable of distinguishing multiple analytes in heterogeneous biological samples with high sensitivity. Our technology leverages a multiresonant metasurface to simultaneously enhance the different vibrational fingerprints of multiple biomolecules. By providing up to 1000-fold near-field intensity enhancement over both amide and methylene bands, our sensor resolves the interactions of lipid membranes with different polypeptides in real time. Significantly, we demonstrate that our label-free chemically specific sensor can analyze peptide-induced neurotransmitter cargo release from synaptic vesicle mimics. Our sensor opens up exciting possibilities for gaining new insights into biological processes such as signaling or transport in basic research as well as provides a valuable toolkit for bioanalytical and pharmaceutical applications.

5.2   Introduction

Optical spectroscopy approaches, including infrared (IR) absorption, circular dichroism (CD), and Raman scattering, are powerful label-free techniques for detecting biomolecules and extracting detailed chemical information in a real-time and non-destructive manner.[188–191] The mid-infrared spectral range is of pivotal importance for these detection approaches due to the presence of strong characteristic absorption fingerprints, which enable the specific identification of biomolecules of different chemical nature.[91–94,108,192] Importantly, all basic building blocks of life such as lipids, proteins, and nucleic acids exhibit distinct and unique fingerprints in this spectral range. Detecting association, dissociation, and other molecular interactions in mixtures of these components are crucial for understanding a multitude of biological systems and processes in health and disease. Consequently, differentiating and monitoring individual components in such heterogeneous mixtures are a central objective in biosensing. It is particularly important for the understanding of pathological conditions, where uncontrolled interactions of cellular membranes with lytic peptides lead to membrane perforation and cell death.[193,194] Resolving multi-analyte systems are also crucial in studying lipid vesicles encapsulating cargo molecules, which are utilized by most cell types as biological shuttles and regulate a multitude of important cellular processes.[195] For instance, synaptic vesicles in neurons loaded with neurotransmitter molecules can release their cargo upon stimulus to transmit chemical signals to postsynaptic neurons, thereby making perception and thought possible.[196]

Resolving such dynamic membrane processes with standard label-free assay techniques such as quartz crystal microbalance (QCM)[197] and surface plasmon resonance (SPR)[66] is extremely challenging. Indeed, the competing effects of protein association, lipid membrane perforation, and cargo release on net analyte mass and refractive index make it difficult to decouple the contribution of the individual analytes from the overall signal. Therefore, to study complex

interactions in multi-analyte biological systems, it is pivotal to develop new label-free sensing platforms that can chemically discriminate different biomolecular species and independently track their time evolution.

Infrared absorption spectroscopy is the prime tool for addressing such challenges, but traditional implementations struggle in resolving submonolayer films and ultrathin membrane systems. Metasurfaces excel at controlling light on the nanoscale and provide a powerful platform for tailoring the spectral response and light localization in nanophotonic devices.[198–201] Engineered metasurfaces can create intense highly confined hot spots of the electromagnetic field, providing strong interaction with adjacent analytes and thus making them ideal candidates for biosensing and spectroscopy applications.[107,128,202–206] Furthermore, the vibrational–absorption enhancement of IR metasurfaces extends tens of nanometers from their surface,[60] making them suitable for multi-layer assays which are not accessible by their Raman counterparts (surface-enhanced Raman spectroscopy), whose enhancement is limited to only a few nanometers.[207,208]

In this work, we present a chemically specific, label-free nanophotonic biosensor for distinguishing multiple analytes in dynamic lipid membrane processes. Our infrared sensor uses a multiresonant metasurface consisting of self-similar overlapping nanoantenna arrays to provide up to 1000-fold near-field intensity enhancement over multiple spectral bands. We exploit this metasurface sensor concept to unravel the interaction of biomimetic lipid membranes with different polypeptides as well as the dynamics of vesicular cargo release. Real-time, chemical-specific detection of these biological entities is performed by extracting their characteristic fingerprints in the amide and methylene absorption regions. Significantly, we leverage our technology to study the interaction of lipid membrane systems with melittin, a toxic pore-forming peptide. We show that our technique can monitor in real time the melittin association process and the simultaneous disruption of the lipid membrane with high sensitivity, exquisite chemical specificity and without labeling. Extending this concept to more complex dynamic membrane processes, we then leverage our method to monitor melittin-induced neurotransmitter cargo release from synaptic vesicle mimics, paving the way toward exciting applications in neurobiology and drug development for brain-related diseases.

5.3   Results and Discussion

5.3.1   Multiresonant Metasurface for Molecule-Specific Detection

The strong near fields excited in the vicinity of metallic nanoantennas provide an ideal platform to enhance the weak vibrational fingerprint signals originating from nanometer-sized analytes and biological membranes.[209] Typically, the resonance frequency of mid-IR nanoantennas is spectrally tuned to overlap with the characteristic vibrational modes of the target biomolecules, which has previously been demonstrated using arrays incorporating a single antenna length.[60,108] Extending this functionality to multi-analyte biosensing requires a metasurface that supports multiple resonances that can be individually tuned to match the characteristic vibrations of the different analytes of interest (Figure 5:1). Current approaches mainly use a uniform array of multiresonant

elements.[128,203] However, resonances in such systems are typically excited with reduced efficiency levels for higher-order modes associated with smaller resonant feature sizes, resulting in decreased SEIRAS performance at these frequencies.[133,210–212] Furthermore, the electromagnetic coupling between the different resonant modes impedes a straightforward spectral tuning of the individual resonance frequencies.[210,212] Our approach overcomes these two major limitations by allocating distinct resonances on multiple overlapping arrays with different periodicities.
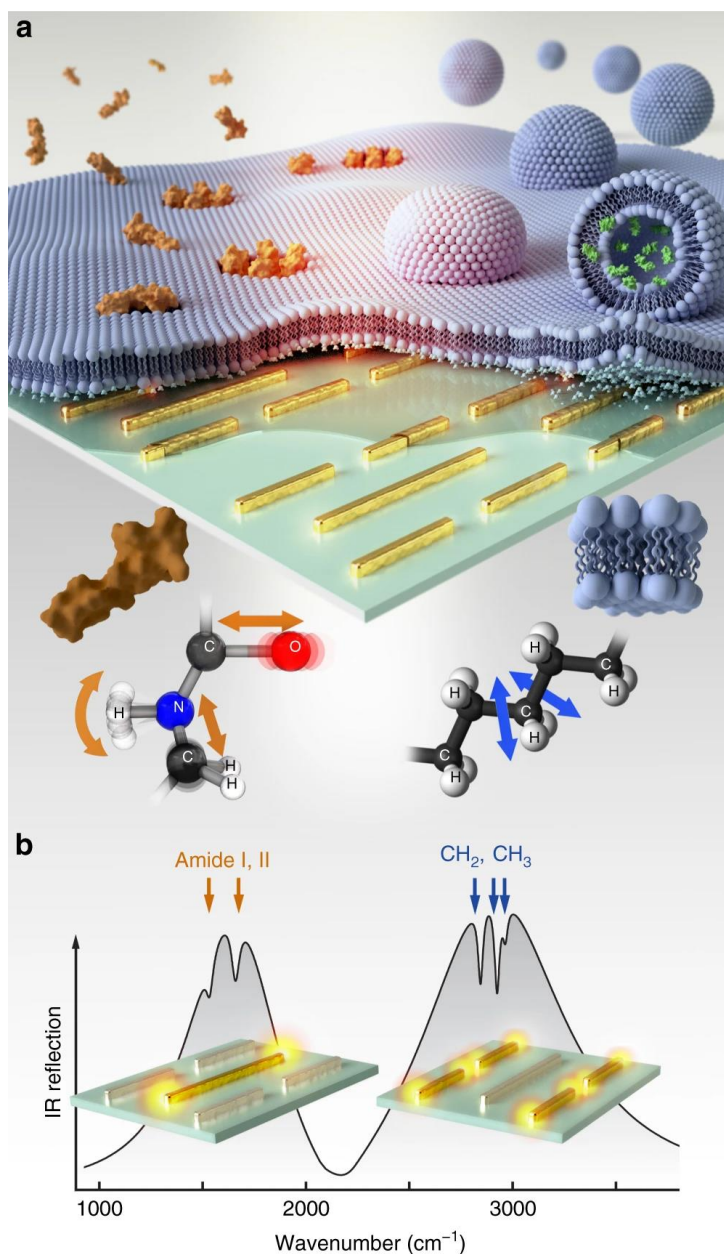
Figure 5:1 Nanophotonic label-free biosensor for chemically distinguishing multiple analytes in biological samples. a) Multiresonant mid-IR nanoantennas are leveraged to enhance the vibrational–absorption signals associated with biomimetic lipid membrane formation, polypeptide/membrane interaction, and vesicular cargo release on the sensor surface. b) Antenna resonance positions are engineered to simultaneously overlap with the vibrational signatures of both the amide I, II, and the CH2, CH3 absorption bands, allowing for the simultaneous enhancement and detection of lipid- and protein-induced absorption changes. The 3D model of melittin used in this figure was imported from RSCB Protein Data Bank, DOI: 10.2210/pdb2MLT/pdb, which was deposited by D. Eisenberg, M. Gribskov, and T.C. Terwilliger. All rights reserved.

Our metasurface design is composed of two sets of gold nanodipoles that provide simultaneously a low- and high-frequency resonance, which can be individually adjusted by tuning the corresponding dipole lengths L_1 and L_2 (Figure 5:2a). The lengths are designed to be approximately

half the corresponding operating wavelength accounting for the dielectric environment. Additionally, the periodicity is adjusted to make the accumulated scattering cross-section of the dipoles equal to the geometrical cross-section of the array, resulting in high reflectance values between 60 and 75 % at resonance. In particular, this requires the density of short dipoles (length L_1) in the multiresonant metasurface to be four times larger than that of long dipoles (length L_2). This design concept can also be understood as overlapping dipole arrays, where the lateral dimensions (both the dipole length and periodicity) of the second array have been almost equally scaled with respect to the first array. Because of this self-similar geometry, the spectral response is composed of two resonances that are spectrally separated by the geometric scaling factor between arrays and are excited with almost identical efficiency. Importantly, our versatile multi-periodicity self-similarity concept is scalable to achieve multiresonant devices with more than two peaks, if required by the target application.[134]
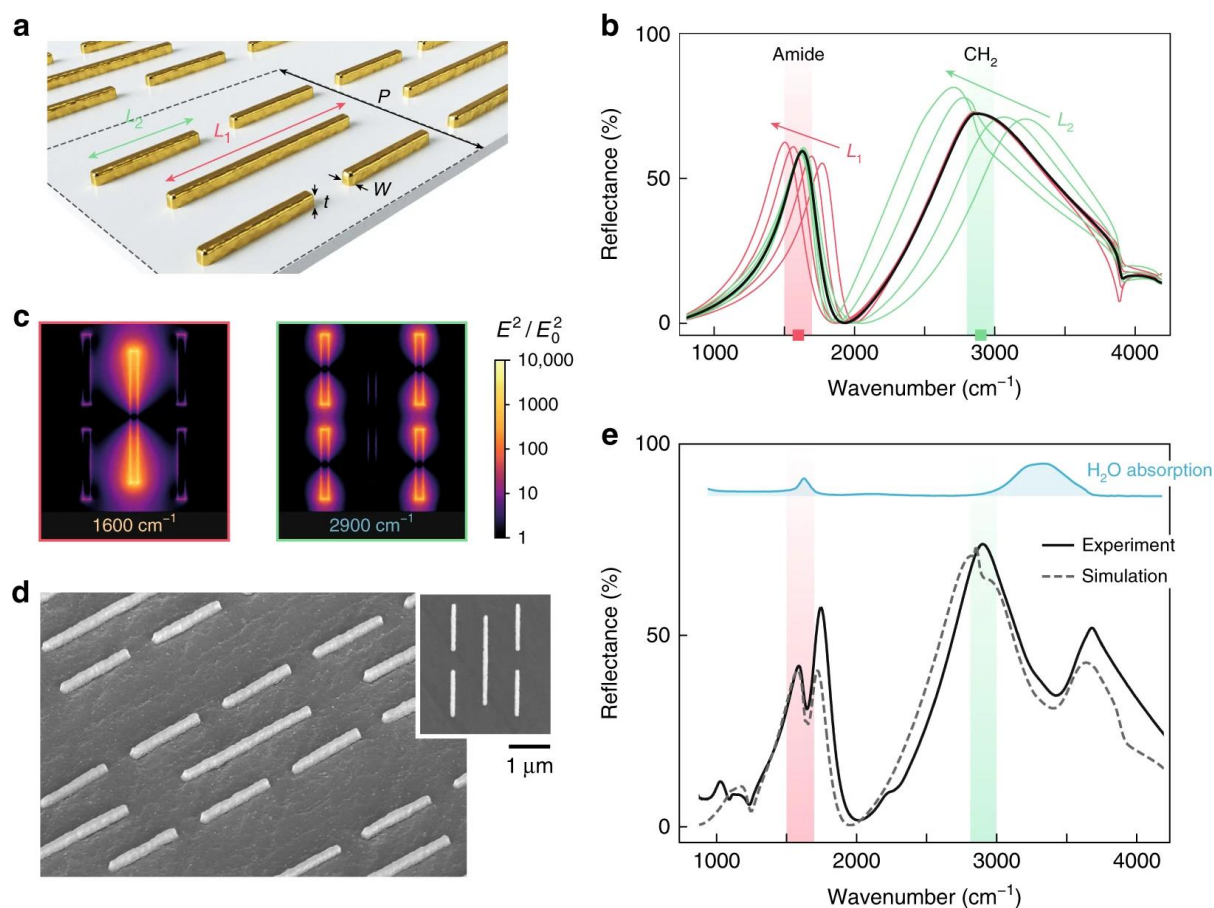
Figure 5:2 Multiresonant metasurface sensor platform. a) Schematic of the multiresonant mid-IR metasurface composed of two sets of gold nanodipoles (L_1 = 1.8 µm, L_2 = 0.95 µm, P = 2.6 µm, W = t = 100 nm). b) Simulated reflectance spectrum of the multiresonant metasurface for the nominal design (black curve), and with varying lengths L_1 (red curves) and L_2 (green curves) in a ± 10 % range. An immersion media with refractive index n = 1.32 has been considered to represent the aqueous environment. The two resonances are independently adjusted to overlap with amide and CH_2 bands. c) Near-field distribution of the multiresonant metasurface parallel to the substrate plane at the amide and CH_2 bands. Each set of dipole nanoantennas is excited and exhibits strong near fields (bright yellow color) only for the corresponding resonance frequency. d) Scanning electron microscope image of the nanofabricated multiresonant metasurface. e) Experimental reflectance spectra of the multiresonant metasurface in phosphate buffer saline (PBS) solution. The full frequency–dispersive complex refractive index of water has been considered in the simulated reflectance spectrum.[213] Peak positions agree well with the simulations from (b). The additional dips in the peak lineshapes are due to the absorption bands of water in the mid-IR (blue-shaded area).

The optical response of the multiresonant array is investigated using a 3D Maxwell equation solver based on the finite element method (see section 5.5.5). The simulated reflectance spectrum of the nanoantenna array contains two well-defined resonances, as shown in Figure 5:2b. These resonances are carefully adjusted to spectrally match with the amide and CH_2 spectral regions, which contain the intense IR absorption bands of proteins and lipids, respectively. Specifically, we target the amide I and II bands located around 1560 and 1660 cm^{-1} as well as the methylene doublet located around 2850 and 2930 cm^{-1}. Naturally, in addition to proteins and lipids, peptides

and other chemicals can equally be detected with our method as long as they support distinct fingerprint signatures within the resonance bands of the metasurface. Modifying L_1 or L_2 shifts the corresponding resonance while leaving the other resonance unaffected, indicating that the two sets of nanodipoles are weakly coupled and their electromagnetic response is independent from each other. Such independence is a key characteristic that allows the metasurface design to be adjusted in a straightforward manner to enhance selected vibrational bands from different analytes.

Simulated near-field distributions (Figure 5:2c) show that only one set of nanodipoles is resonantly excited for each spectral band of interest, which indicates that our metasurface design can also provide spatial sensitivity by detecting only the molecules placed in the near-field hot spots of the corresponding antennas. Even though this capability is not exploited in this work, it could find applications in multiplexed detection and imaging-based techniques. On the other hand, the spatial sensitivity can be a disadvantage in experiments where the analytes are inhomogeneously distributed over the surface, or if it is required that the vibrational signals arise from the same molecules for all the utilized infrared bands. Overall, our design provides maximum local near-field intensity enhancements between three and four orders of magnitude for both bands. Furthermore, the near-field intensity extends up to tens of nanometers from the metasurface (Figure 5:7), providing penetration depths that are comparable with those in state-of-the-art single-band SEIRA substrates. Such extended penetration depths are in contrast to the 1–2 nm depths achieved by surface-enhanced Raman spectroscopy and gives SEIRAS a unique advantage for probing lipid membranes and vesicles.

The multiresonant array is fabricated on an IR-transparent CaF_2 substrate by electron beam lithography and a lift-off process (see section 5.5.1). Scanning electron microscope images of the device are shown in Figure 5:2d. The IR reflection spectrum of the array is measured with a FTIR spectrometer, illuminating the chip from the backside of the substrate and immersing it in phosphate-buffered saline (PBS). The measured reflectance spectrum shown in Figure 5:2e is consistent with the dual-resonance spectrum shown in Figure 5:2b when the IR absorption bands of water are incorporated and is in good agreement with electromagnetic simulations accounting for the frequency–dispersive complex refractive index of water.[213] More importantly, the measured results confirm the multiresonant response of the metasurface, providing near-field enhancements at two spectral bands that overlap with the amide and CH_2 vibrations, making it an excellent candidate for multi-analyte mid-IR biosensing.

5.3.2   Simultaneous Monitoring of Multiple Analytes

To demonstrate the capability of monitoring and distinguishing multiple biological analytes simultaneously, we use a bioassay based on the additive association between streptavidin (SA) and a phospholipid membrane. Specifically, we utilize 1,2-dioleoyl-sn-glycero-3-phosphocholine (DOPC) vesicles to form a supported lipid bilayer (SLB) on the sensor surface, which acts as a model cell membrane for the study of protein interaction kinetics.[214] Prior to experiments, our plasmonic sensor chips are functionalized with a 10 nm silicon dioxide layer coated by atomic layer deposition

and exposed to a short oxygen plasma treatment to provide a hydrophilic surface suitable for membrane formation.[60,215–218] Bilayer membrane fluidity and thickness are confirmed via fluorescence recovery after photobleaching (FRAP) and surface plasmon resonance (SPR) experiments (Figure 5:8 and Figure 5:9). To selectively bind SA to the membrane, vesicles for bilayer formation are prepared from a lipid mixture consisting of DOPC and a small percentage of biotinylated lipids.

During biosensing measurements, the multiresonant metasurface chip is placed into a polydimethylsiloxane (PDMS) microfluidic cell to allow for the controlled delivery of the various molecules (Figure 5:3a). Real-time mid-IR reflectance spectra are measured with an FTIR spectrometer from the backside of the metasurface to prevent the complete absorption of infrared light by water and enable in-solution mid-IR experiments. This integrated microfluidic approach allows us to resolve the time evolution of both the lipid bilayer formation and subsequent streptavidin-binding kinetics in situ. A typical reflectance spectrum of the metasurface chip immersed in PBS buffer solution is shown in Figure 5:3b. In addition, a magnified view of the reflectance in the CH_2 spectral region is presented in Figure 5:3c, highlighting the absorption fingerprint after lipid membrane formation on the sensor chip. To aid the subsequent analysis of the time-resolved spectral data, the reflectance spectra are converted to differential absorption (Figure 5:3d) and baseline corrected.[60,104]
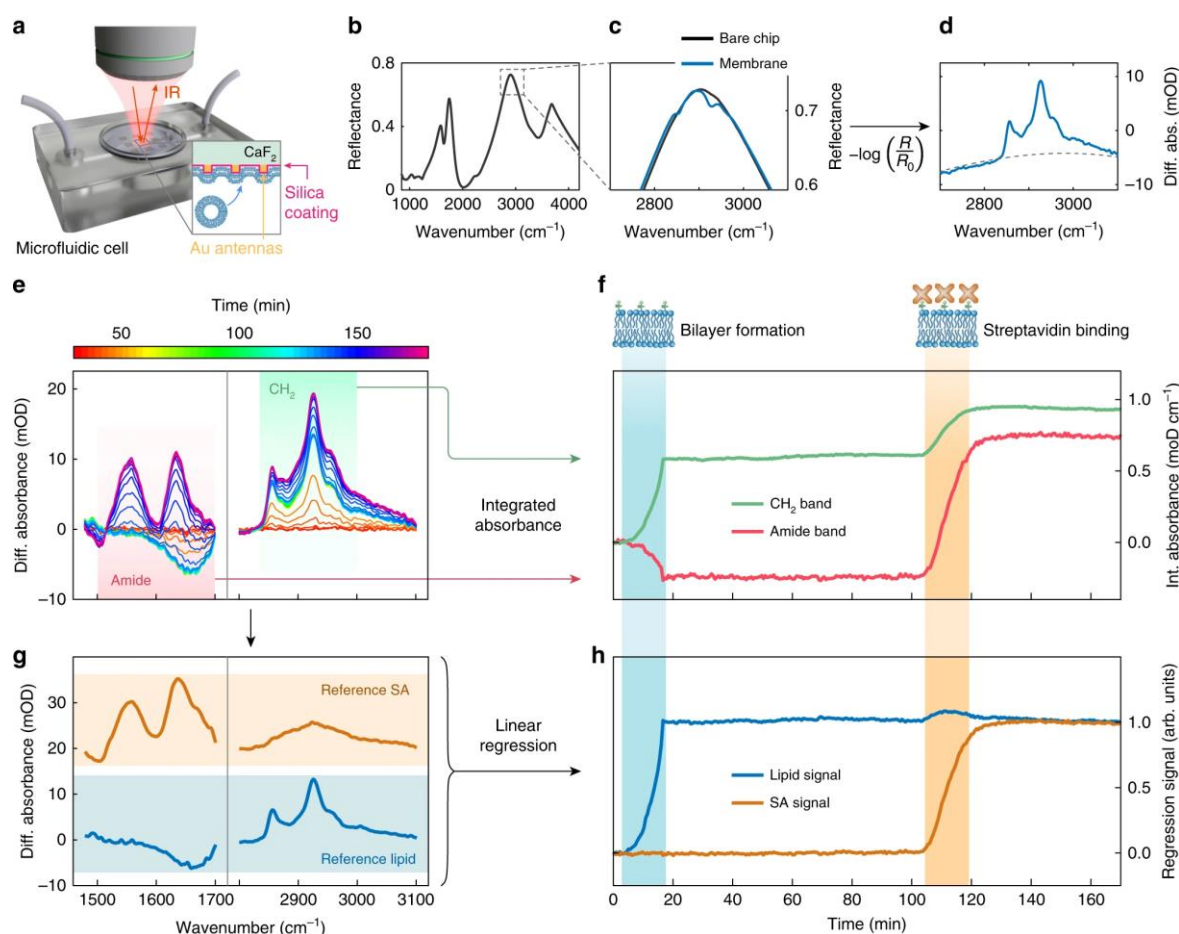
Figure 5:3 Simultaneous monitoring of multiple biological analytes. a) Schematic of the experimental configuration. b) Infrared reflectance spectrum of the multiresonant sensor chip in PBS buffer solution. c) Reflectance spectra before (R_0) and after (R) lipid membrane formation in the CH_2 band spectral region, magnified from marked area in (b). d) Differential absorption spectrum calculated from the reflectance spectra in (c). The dashed line corresponds to the second-order polynomial used for baseline correction. e) Color-coded time-dependent differential absorption spectra acquired during the lipid membrane formation and streptavidin-binding experiment. f) Time trace of the integrated absorbance signal in the amide (red-shaded area) and CH_2 (green-shaded area) bands from (e). The lipid and streptadivin injection steps are indicated by the blue- and orange-shaded areas, respectively. The integrated absorbance signals from the amide (red curve) and CH_2 (green curve) bands exhibit pronounced signal modulations during the lipid membrane formation and streptavidin-binding steps, evidencing an inadequate discrimination of the two analytes. g) Reference spectra for the lipid (blue-shaded area) and streptavidin (orange-shaded area) signal contributions. h) Linear regression signals obtained from the spectral data in (e) with respect to the reference spectra in (g). Linear regression signals for lipid (blue curve) and streptadivin (orange curve) show a significant signal increase only during the corresponding lipid or streptavidin injection step, demonstrating effective chemical discrimination

The time evolution of the differential absorbance spectra over the course of the experiment is shown in Figure 5:3e for both amide and CH_2 bands. After filling the fluidic channels with PBS buffer solution, 100 nm diameter DOPC vesicles containing 5 % of biotin-functionalized lipids were injected and allowed to form the SLB. Subsequently, streptavidin was injected to bind to the

biotinylated lipids present in the membrane (see section 5.5.3). The onset of absorption signals in both bands can clearly be observed in the differential absorbance results, indicating successful lipid membrane formation and streptavidin association in the bioassay. To further visualize these results, we calculate and trace the integrated absorbance from 1500 to 1700 cm^{-1} (amide I–II) and from 2800 to 3000 cm^{-1} (CH_2) over time (Figure 5:3f). The lipid bilayer formation results in a pronounced increase of the integrated absorbance in the CH_2 bands, while streptavidin binding produces a respective increase in the amide-integrated absorbance. However, since the molecular structure of streptavidin contains CH_2 groups, the streptavidin injection also produces a change in the CH_2 signal. A similar effect can be observed in the amide-integrated absorbance during lipid membrane formation, where water displacement produces a negative absorbance signature due to the H_2O in-plane bending mode. This complex behavior indicates that a simple tracking of the integrated absorbance is insufficient to resolve the different analytes in multi-component systems, especially if the constituent biomolecules have overlapping absorption signatures.

To overcome this challenge, we perform linear regression of the time-dependent differential absorbance data with respect to reference spectra for DOPC lipids and streptavidin (Figure 5:3g). Reference spectra were obtained by measuring an SLB for the lipid reference and, independently, a protein monolayer formed by physisorption for the streptadivin reference. The lipid and protein signals directly correspond to the coefficients in the linear combination of reference spectra that minimize deviation from the measured reflectance spectrum under the least square criterion (see section 5.5.4). This approach enables us to separate and identify the contributions of the two biological components in the full differential absorbance signal (Figure 5:3h).[219] The effective chemical discrimination of the components becomes obvious when examining the lipid and streptavidin regression signals, which show a significant signal increase only during the corresponding lipid and streptavidin injection steps, respectively. The extracted values of the regression signals correspond to the analyte mass on the sensor surface relative to the amount present in the corresponding reference. As a result, when the surface density of the molecules changes, the regression signals vary accordingly.

To confirm that two reference spectra used are sufficient to capture the full biological information in our time-dependent measurements, we performed principal component analysis (PCA) over the spectral data corresponding to all of the time points, and found that 99.7 % of the total variance is accounted for by the first two principal components (Figure 5:11). Importantly, our platform is not limited to two biochemical species and can be extended to bioassays with a higher number of biological components by including the corresponding reference spectra in the linear regression analysis, as will be shown in the next section. On the other hand, the linear regression approach has limitations when exploring unknown samples or analytes whose absorption spectra are not known. A PCA approach could be more suitable in these cases, but the interpretation based on principal component scores would be significantly more challenging (section 5.5.12).

5.3.3 Melittin-Induced Pore Formation in Membranes

Moving beyond simple additive protein–membrane association processes, we investigated more complex dynamics of lipid membrane disruption induced by toxic peptides. For this purpose, we utilize melittin, a hemolytic peptide constituting the main toxic component of apitoxin, the bee venom.[220] Melittin is well known for its efficient association with lipids and the resulting perforation of lipid membranes through the formation of pores.[221] Due to its cytotoxicity and membrane disruptive properties, melittin is a naturally occurring anti-microbial and holds potential for the treatment of immune-related diseases such as many types of cancer.[222] To demonstrate the versatility of our approach, we study melittin-induced pore formation in membranes for two distinct biological schemes: the disruption of a supported lipid membrane and the release of encapsulated cargo from surface-attached lipid vesicles.

In the first scheme, we monitor the interaction between lipids and melittin by forming an SLB from unloaded DOPC vesicles, next removing residual vesicles with PBST and subsequently injecting increasing concentrations of melittin (Figure 5:4a). In contrast to the previous additive association measurements, we observe a clear decrease of the lipid signal upon melittin injection, which correlates with a strong increase of the melittin signal after a transient fluctuation induced by PBST. This behavior is caused by insertion of melittin into the lipid membrane, which leads to the displacement of lipids due to the formation of nanosized pores.[223] The observed strong signal modulation is caused by the efficient association of melittin to the DOPC lipids, which is confirmed with independent bulk circular dichroism measurements (Figure 5:12). Increasing the injected melittin concentration from 1 to 100 µM demonstrates a progressively higher and non-proportional perforation of the lipid membrane. Particularly, for the highest concentration of 100 µM, more than 60 % of the lipid molecules are displaced from the surface based on the lipid regression signal, which is also corroborated by independent fluorescence experiments (Figure 5:13). The recorded signals capture clearly the melittin association and dissociation during melittin injection and PBS rinsing steps, respectively. The association kinetics for 1 µM concentration are qualitatively different than for 10 and 100 µM, which we attribute to the presence of melittin molecules in the membrane after the first injection step (1 µM). During the dissociation phase, we observe that ~80–90 % of the adsorbed melittin remains in the membrane after the PBS rinsing, indicating high membrane/melittin affinity. It is important to note that we are able to investigate melittin-binding kinetics on a supported lipid membrane (Figure 5:9), using melittin concentrations in the same range as in previous works.[221]
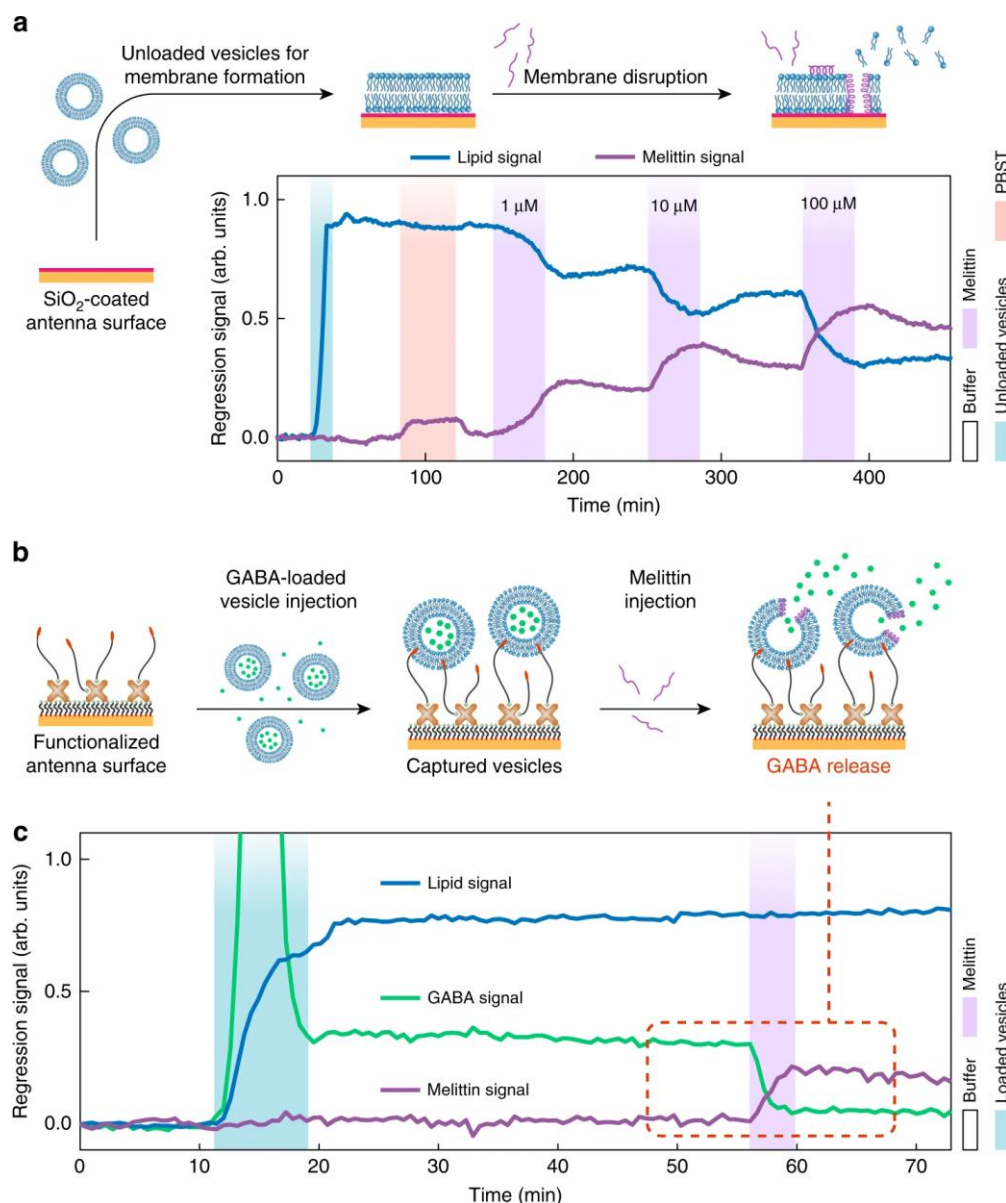
Figure 5:4 Melittin-induced membrane disruption and vesicular cargo release. a) Melittin association to the supported lipid bilayer (SLB) and melittin-induced disruption of the membrane for increasing melittin concentrations (1, 10, and 100 µM). The time evolution of the melittin linear regression signal (purple) shows melittin-membrane association and partial dissociation phases for each melittin injection time step. The increase in melittin signal is accompanied by a clear decrease in the lipid regression signal (blue) evidencing loss-of-membrane integrity, which intensifies with increasing melittin concentrations. b) Sketch of the vesicle cargo release experiment. The sensor metasurface is functionalized with hydrophilic tethers displaying cholesterol moieties, which are then used to capture lipid vesicles loaded with the neurotransmitter gamma-aminobutyric acid (GABA). Injection of melittin perforates the lipid vesicle membrane, resulting in a release of GABA cargo molecules. c) Time-resolved linear regression signals for the three characteristic biological components in the experiment: lipid, GABA, and melittin. After the injection of GABA-loaded vesicles, successful attachment of intact, loaded vesicles to the surface is corroborated by the stable lipid and GABA regression signals. The strong initial peak of the GABA signal is caused by the transient flow of extravesicular GABA molecules present in the bulk solution. Melittin injection results in a fast and pronounced decrease of the GABA signal, indicating efficient cargo release.

This experiment evidences that our sensor platform could go beyond the capabilities of other label-free biosensing approaches based on mass or refractive index detection, such as quartz crystal microbalance (QCM) or surface plasmon resonance (SPR) techniques, which are considered the gold standard in real-time label-free detection of biomolecular interactions.[66,224] These techniques enable the study of binding kinetics in processes where multiple analytes provide a net contribution to the total mass accumulated on the sensor, however, they struggle in situations where the injection of one kind of analyte triggers the removal of another analyte that is already present on the surface. The chemical specificity of our technique overcomes this fundamental limitation and provides exciting opportunities for the study of multi-analyte systems.

As a final demonstration, we applied our approach to a system with increased complexity, featuring small analyte molecules in addition to lipid vesicles and peptides. This system exemplifies that our technology can be extended to monitor multiple analytes in more complex scenarios, such as the release of cargo molecules from vesicles in our case. We focus on cholesterol-enriched lipid vesicles containing neurotransmitters, a system mimicking synaptic vesicles naturally found in neurons. Specifically, vesicles are loaded with GABA, which is the major neurotransmitter for inhibitory synaptic transmission. Consequently, GABA uptake and release processes influence a multitude of brain-related diseases and GABA receptors are major drug targets for such illnesses.[225]

To enable the observation of the biological process schematized in Figure 5:4b, we first optimized a surface functionalization protocol for capturing intact cargo-filled lipid vesicles with a diameter of 50–70 nm on our metasurface chip. This is achieved by functionalizing the gold antenna surface using biotinylated thiols, followed by the attachment of streptavidin, which is then utilized to bind biotin-PEG-cholesterol vesicle tethers (see section 5.5.3). In a second step, GABA-filled vesicles are captured on the functionalized metasurface and the release of the cargo is triggered via the melittin-induced perforation of the vesicle membrane.

To detect the vibrational signature of the GABA molecules, we focus on its distinct absorption peak at 1562 cm^{-1}, resulting from the asymmetric stretching of its carboxylate group. Our platform can efficiently detect the absorption peak of GABA via the first resonance mode of the metasurface. Crucially, the GABA absorption signature exhibits strong spectral overlap with the amide II signature of melittin. Therefore, simple analysis based on integrated absorbance over the amide I–II range is unable to simultaneously trace the signals of GABA and melittin. However, since the absorption spectra of the three analytes (lipid, melittin, and GABA) form a linearly independent set (Figure 5:14), our linear regression approach can easily extract the signal contributions of each molecule. As demonstrated in Figure 5:4c, time-resolved linear regression signals for the three biomolecular components in the experiment (lipid, melittin, and GABA) are efficiently distinguished. This result demonstrates the applicability of our approach in biological systems with more than two analytes, as long as their infrared spectra are sufficiently different and linearly independent over the detection bands of the metasurface.

The injection of GABA-loaded vesicles induces a pronounced increase in the signals corresponding to both lipid and GABA channels. After the initial binding phase, both signals remain stable for more

than 30 min under continuous buffer solution flow, indicating the capture of intact vesicles on the sensor metasurface. The strong, transient peak of the GABA signal during injection is attributed to extravesicular GABA molecules in the bulk solution, which are subsequently washed away by the flow of buffer solution. Crucially, GABA molecules cannot attach to the functionalized metasurface (Figure 5:15), confirming that the stable GABA signal in Figure 5:4c originates from encapsulated molecules in the vesicles.

After melittin injection, the association of this peptide with the vesicle membrane is clearly detected as an increase of the melittin regression signal. In contrast to our previous SLB experiments, here the lipid regression signal remains constant during melittin association, which is attributed to the accommodation of the inserted melittin molecules in the tethered vesicles via a slight increase of their size, leaving the density of lipid molecules mostly unaffected. On the other hand, the binding of melittin to SLBs in previous experiments produced a lateral displacement of lipid molecules, which lead to the reduction of the lipid surface density (compare to Figure 5:4a). Strikingly, the injection of melittin causes a simultaneous and pronounced decrease of the GABA regression signal. This is unequivocal evidence of the melittin-induced cargo release of the vesicles. Based on the relative GABA signal levels before and after the melittin injection step, we conclude that around 85 % of the encapsulated GABA molecules are released through the perforated membranes.

5.4   Conclusion

We have developed a label-free and chemically specific nanophotonic biosensor for extracting and distinguishing molecule-specific information in multi-analyte biological systems. Our approach leverages a multiresonant mid-IR metasurface that provides up to three orders of magnitude local near-field intensity enhancements simultaneously over the amide and methylene bands. The introduced metasurface concept is flexible to add additional bands that can be individually adjusted to suit different applications. The combination of real-time spectral acquisition with advanced linear regression analysis allows to discriminate the different analytes and accurately trace the interaction kinetics. We demonstrate that our sensor is well adapted for real-time monitoring of lipid–protein systems in aqueous environments and the study of a range of important processes such as lipid–protein association, protein-induced disruption of membranes and vesicular cargo release.

By studying the interaction of the pore-forming toxin melittin with lipid membranes, we showed that our method could independently trace melittin and lipid signals and reveal melittin-induced disruption of the membrane. This experiment highlights that our platform can greatly contribute to elucidate the underlying mechanisms of anti-microbial, cytolytic, and cell-penetrating peptides. Furthermore, the label-free real-time monitoring of neurotransmitter cargo release from synaptic vesicle mimics demonstrates the applicability of the method for biomolecular systems with increased complexity. In this regard, our sensor can contribute to study important classes of lipid

vesicles such as synaptic vesicles in neurodegenerative diseases, exosomes in cancer, as well as drug release mechanisms from liposomes in pharmaceutical research.

5.5   Supplementary Information

5.5.1   Sensor Nanofabrication

Metasurfaces are nanofabricated on a CaF_2 substrate by electron beam lithography and a lift-off process. Poly(methyl methacrylate) (PMMA) is used as the pattern defining electron beam resist and a lower molecular weight sublayer is used to help the lift-off process. The resist is coated with a 5–10 nm-thick gold layer to reduce electron charging during exposure. Metasurfaces with a lateral size of $280 \times 280\ \mu m^2$ are exposed with a 100 keV electron beam, developed in MiBK:IPA 1:3 solution and the gold conduction layer is wet etched in $KI + I_2$. Metal nanoantennas are formed by evaporation of a 5 nm-thick Cr adhesion layer and a 100 nm-thick Au layer, followed by a lift-off process carried out in acetone. The chips used for experiments with SLBs are then conformally coated with a thin SiO_2 layer deposited by atomic layer deposition (ALD). The ALD process is performed at 100 °C with alternating cycles of sequentially injecting trimethylaluminum (Al(CH3)3) and tris(tert-butoxy)silanol ((tBuO)3SiOH) with a deposition rate of 1.67 Å per cycle. The gold antennas without a SiO_2 layer used for cargo release experiments were functionalized ex situ by incubating the chip with 1.5 mM HS-C11-EG3-Biotin (ProChimia Surfaces) in ethanol for at least 12 h.

5.5.2   FTIR Measurements

Infrared spectral measurements are carried out using a Fourier transform infrared (FTIR) spectrometer (Bruker Vertex) coupled to an IR microscope (Hyperion 3000) equipped with a reflective Cassegrain objective (NA = 0.4, ×15) and a mercury cadmium telluride (MCT) detector. The light polarization is applied parallel to the axis of the nanoantennas and the collected light is limited to a $200 \times 200\ \mu m^2$ area by knife edge apertures. Experiments are carried out in a dry air purged environment. The measurements are performed in reflectance mode and illuminating the nanoantenna arrays from the backside of the substrate to avoid light propagation across the infrared-opaque water. For real-time microfluidic measurements, the chip is mounted in a custom-built polydimethylsiloxane (PDMS) microfluidic cell, which is connected to a pump to control the analyte flow through the cell. During experiments with SLBs, the flow rate is fixed at 30 $\mu L \cdot min^{-1}$ apart from the bilayer formation step, which is carried out at a flow rate of 15 $\mu L \cdot min^{-1}$ as shown previously.[60] During the cargo release experiments, the flow rate was 50 $\mu L \cdot min^{-1}$. All experiments are carried out in PBS buffer (10 mM phosphate buffer, 2.7 mM potassium chloride, and 137 mM sodium chloride, pH 7.4). Analyte injections (lipid, streptavidin, melittin, and GABA) are performed using a medium pressure injection valve (Upchurch Scientific V-451) to ensure uninterrupted analyte delivery. For the cargo release experiments, the gold antennas previously modified with

biotinylated alkanethiols are further functionalized in situ by flowing 3 µM streptavidin (Thermo Fisher Scientific) followed by 9 µM Cholesterol PEG Biotin (Nanocs Inc.).

5.5.3 Lipid Vesicle Experiments

Small unilamellar vesicles are prepared similarly to the protocol from Ref.[226]. Defined ratios of either DOPC (1,2-dioleoyl-sn-glycero-3- phosphocholine, Avanti Polar Lipids, Inc.) and Biotinyl PE (1,2-dipalmitoyl-sn- glycero-3-phosphoethanolamine-N-(biotinyl), Avanti Polar Lipids, Inc.) or POPC (1-palmitoyl-2-oleoyl-sn-glycero-3-phosphocholine, Avanti Polar Lipids, Inc.) and cholesterol (Sigma-Aldrich) are mixed in chloroform in a round bottom flask and dried under a stream of N_2. Remaining solvent is removed by keeping the mixture under vacuum overnight. The dried lipids are resuspended in PBS by vortexing to achieve a 1 mg·mL^{-1} solution of lipids, which is then exposed to bath sonication for 30 min. For cargo release experiments, the dried lipids are resuspended in PBS with 100 mg·mL^{-1} GABA. After sonication, the solution is then extruded for a minimum of 18 times through 100 nm pore-size polycarbonate filters using an Avestin LiposoFast extruder (Avestin Inc.). After SLB formation in real-time infrared experiments, residual vesicles in the microfluidic system are rinsed with PBS solution containing 0.05 % (wt/vol) polysorbate 20 (Tween 20, Sigma-Aldrich) surfactant (PBST). For cargo release experiments, a twofold dilution of the vesicles (20 % cholesterol, 80 % POPC) in PBS was carried out prior injection and mem- brane perforation was performed with 2 µM melittin (GenScript).

5.5.4 FTIR Data Analysis

The extraction of the IR fingerprints of the analyte is performed by normalizing the reflectance spectra of the sensor to that of the bare sensor before analyte injection. The differential absorbance spectra is calculated by subtracting a second-order polynomial fitted by least-squares method to the nor- malized reflectance. The integrated absorbance signal is calculated by integrating the extracted amide and CH bands over the 1525–1650 cm^{-1} and 2835–2935 cm^{-1} ranges, respectively. The protein and lipid signals are obtained by linear least- squares regression of the absorbance spectrum of the heterogeneous sample using as basis the individual reference spectrum of the protein and lipid. The protein and lipid signals (s_P, s_L) are calculated as (s_P, s_L) = $(\underline{X}^T\underline{X})^{-1}\cdot\underline{X}^T\cdot\underline{a}$, where $\underline{a}$ is the absorbance spectrum of the heterogeneous analyte and $\underline{X} = (\underline{a}_P, \underline{a}_L)$ is the reference absorbance matrix formed by the reference absorbance spectra of the protein and lipid. The reference spectrum for each individual analyte is obtained from independent experiment by measuring: a lipid bilayer formed by vesicle rupture, a streptavidin layer by physisorption, a mellitin layer formed by physisorption and GABA molecules by high concentration (100 mg·mL^{-1}) in flow measurements.

5.5.5 Numerical Simulations

The spectral and near-field characteristics of the nanoantenna arrays are calculated using a commercial solver of Maxwell equations (Ansys HFSS) based on the finite elements method. The periodicity of the arrays is modeled by periodic boundary conditions delimiting the array unit cell.

The structure is excited by an electromagnetic plane wave with light polarization aligned with the dipole antennas and including all propagating Floquet modes. The scattering properties are calculated over an iteratively refined mesh until convergence is reached.

5.5.6   Generalized Metasurface with Three Resonances

The multiresonance metasurface can be generalized to incorporate additional resonances. In Figure 5:5 we show the metasurface design that accommodates three resonances. The multi-resonant metasurface is composed of three sub-arrays of nano-antennas whose periodicities are in a 1:2:4 ratio. The experimental reflection spectrum shows three well-defined optical resonances. This technique can be further extended to accommodate a larger number of resonances by incorporating additional sub-arrays.
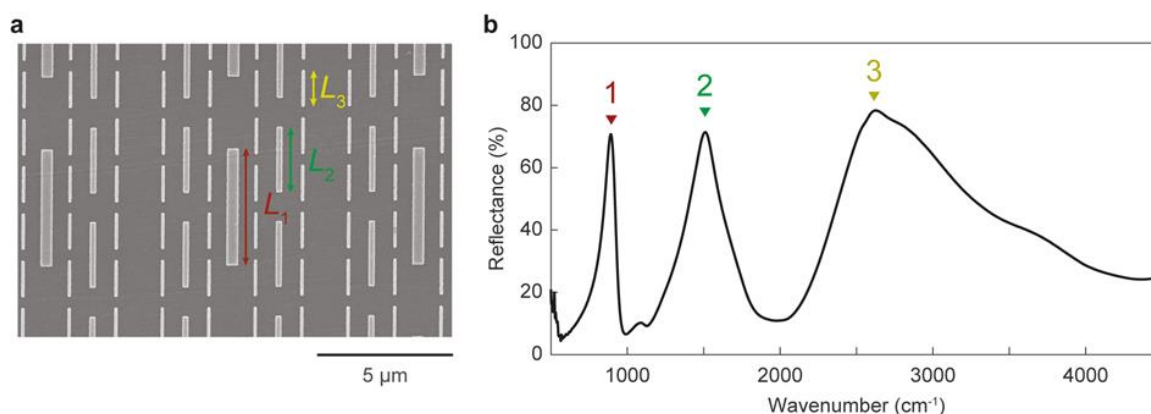
Figure 5:5 Generalized self-similar antenna array metasurface. a) Scanning electron microscope image of the generalized metasurface that accommodates three resonance peaks. The metasurface is composed of three sub-arrays of nanodipoles with lengths $L_1 = 4.10$, $L_2 = 2.30$, $L_3 = 1.27$, widths $W_1 = 0.4$, $W_2 = 0.2$, $W_3 = 0.1$ and periodicities $P_1 = 6.64$, $P_2 = 3.32$, $P_3 = 1.66$ (units in µm). b) Experimental reflectance spectrum of the generalized metasurface. The reflection spectrum shows three well-defined resonances. Each optical resonance is excited by the corresponding sub-array of nanodipoles.

5.5.7   Influence of Water Absorption in the Infrared on Metasurface Transmission

Microfluidic measurements in the mid-infrared are impacted by strong molecular absorption from the required aqueous buffer solutions close to the target amide and methylene bands. To quantify the influence of water absorption on the spectral shape of our multi-resonant metasurface, we extend the numerical simulations presented in the manuscript by including the full complex refractive index of water in this range. Specifically, we consider the metasurface designs from Figure 5:2b of the main text. We compare the reflection spectrum of the designs considering a non-dispersive water environment (Figure 5:6a) and a water environment with a frequency-dispersive complex refractive index from tabulated data taken from literature (Figure 5:6b).[213] In both cases the simulated reflection spectrum of the multi-resonant structure shows two peaks at 1600 and 3000 cm^{-1}, respectively) that are individually tuned modifying the respective dipole lengths L_1 and

L_2. Due to the effect of water absorption bands in this spectral range, the two resonance peaks in the second case show superimposed adsorption bands from water.
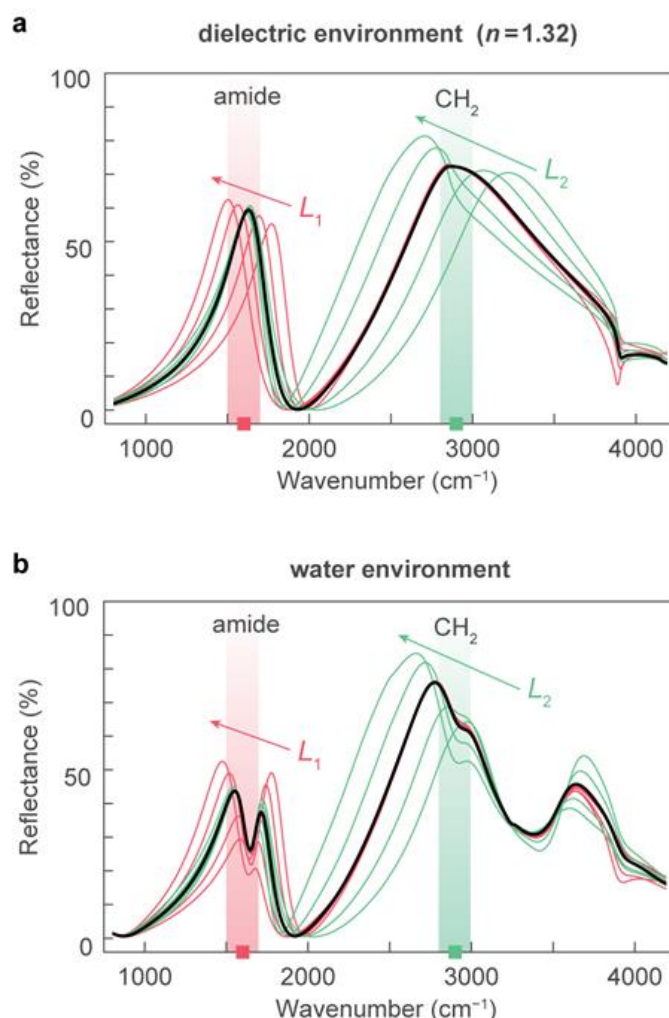
Figure 5:6 Simulated reflectance spectrum of the multiresonant metasurface for the nominal design (black curve), and with varying lengths L_1 (red curves) and L_2 (green curves) in a ± 10 % range. The simulated environment is represented in (a) as a non-dispersive aqueous medium with refractive index n = 1.32. The simulated environment in (b) as an absorptive water layer with a frequency-dispersive complex refractive index from tabulated data.

5.5.8   Near-Field Penetration Depth of the Metasurface

To evaluate the penetration depth of the near-field intensity away from the multiresonant metasurface we have simulated the near-field in the vicinity of the metallic nano-antennas for the two bands of interest. The penetration depth of the metasurface is $\delta = 5$ nm for the methylene band and $\delta = 10$ nm for the amide band (for 1/e drop in intensity). As expected, the penetration depth for the amide band is higher than for the methylene band due to longer wavelengths. Of course, the near-field extends beyond the penetration depth at a lower intensity and, for instance, the metasurface can access up to a 20 nm depth with 10 % of the near-field peak intensity. This result contrasts with the 1–2 nm depth achieved in SERS, the Raman counterpart of SEIRAS, and

allows the metasurface to probe multiple molecules in multi-layers systems (Figure 5:3) and the molecules inside the vesicles in the cargo-release experiments (Figure 5:4b).
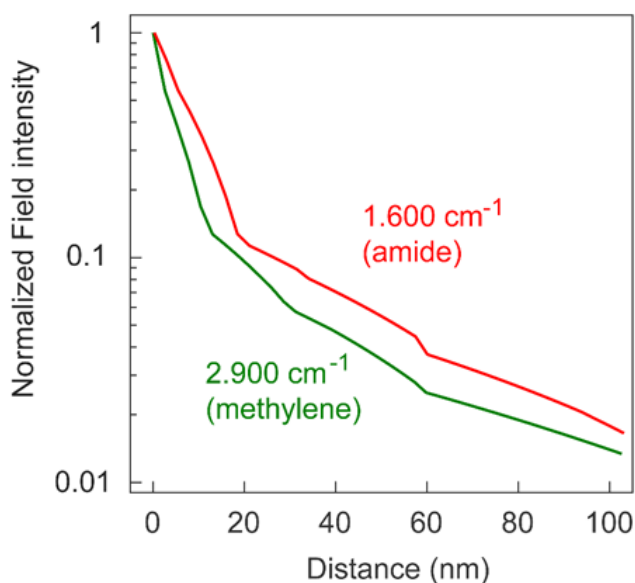
Figure 5:7 Simulated near-field intensity for the multiresonant metasurface as a function of the distance to the surface of the corresponding nano-antennas. The near- field intensity normalized to its maximum value is shown for the amid band (1600 cm^{-1}) and methylene band (2900 cm^{-1}).

5.5.9   Verification of Membrane Fluidity via FRAP Measurements

To assess the fluidity of the supported lipid bilayers used in our real-time microfluidic experiments, we perform fluorescence recovery after photobleaching (FRAP) measurements. The FRAP experiments shown in Figure 5:8 were carried out with a Zeiss LSM 710 upright confocal microscope following the protocol from Ref.[60], but with NBD-PC (1-palmitoyl-2-{12-[(7-nitro-2-1,3-benzoxadiazol-4-yl)amino]dodecanoyl}-sn-glycero-3-phosphocholine, Avanti Polar Lipids, Inc.) lipids instead of Texas Red DHPE (1,2-dihexadecanoyl-sn-glycero-3-phosphoethanolamine, Life Technologies).
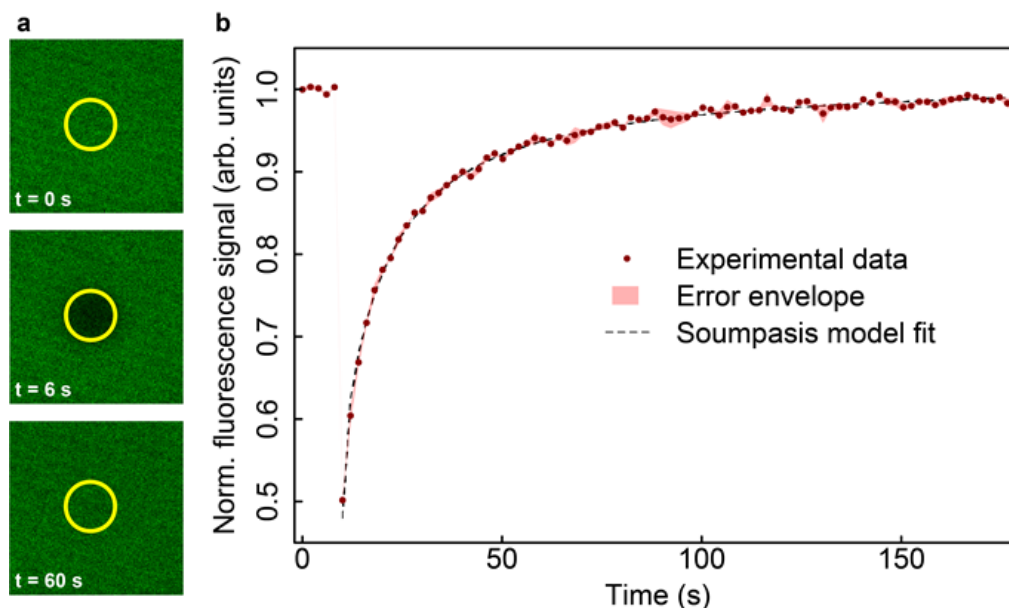
Figure 5:8 Membrane fluidity. a) FRAP microscopy images of a fluorescently tagged supported lipid bilayer at measurement start (t = 0 s), directly after bleaching (t = 6 s) and at t = 60 s. The bleaching spots have a diameter of 10 µm and are indicated with yellow circles. b) Data analysis of FRAP measurements confirm the fluidity of the lipid membranes utilized in our experiments. The average of three measurements as well as the error envelope (standard error of the mean) is shown.

Data analysis is performed with the FRAP Analyzer program (University of Luxembourg; http://actinsim.uni.lu) as described previously.[60] After photobleaching, we observe a fast recovery of the fluorescence signal on a timescale of 50 s, which confirms the fluidity of the bilayers utilized in our experiments and is consistent with previous studies on similar membrane systems.[60]

5.5.10 Determination of Supported Lipid Bilayer Thickness

The thickness of the supported lipid membranes in our experiments is determined via a multi-parametric surface plasmon resonance (SPR) spectroscopy recording angle-scanning SPR data simultaneously at three different wavelengths (Bionavis 210A VASA). In particular, we perform the SLB formation using DOPC vesicles prepared in the same way as for the other SLB experiments and inject them at the same flow rate over gold chips coated with ALD-deposited silica.

The resulting SPR signal curves before and after formation of a SLB (labelled baseline and membrane, respectively) are shown in Figure 5:9. The formation of the membrane induces a clear shift of the resonance angle for all three individual laser wavelengths. To extract the thickness of the lipid membrane, we fit a dielectric multilayer model to the measured SPR curves using BioNavis' LayerSolver software. The fitting procedure works by modeling the multilayered optical system in terms of thickness, refractive index and attenuation coefficient, and then numerical calculations are iteratively performed using Fresnel's equations and a transfer matrix formalism of 2 × 2 matrices.[227]

The parameters of the multilayer model for the baseline and membrane cases are shown in Table 5:1 and Table 5:2, respectively. The calculations yield a refractive index of n=1.45 and a thickness of 5.1 nm for the SLB. Both values agree very well with values reported in the literature[228,229] and confirm the presence of a single DOPC bilayer on the surface. It is important to note that our multi-parametric SPR results provide a thickness of 10.48 nm for the SiO_2 which is matching to the nominally used value in ALD deposition. This also evidences that the thickness readings provided by SPR are reliable.
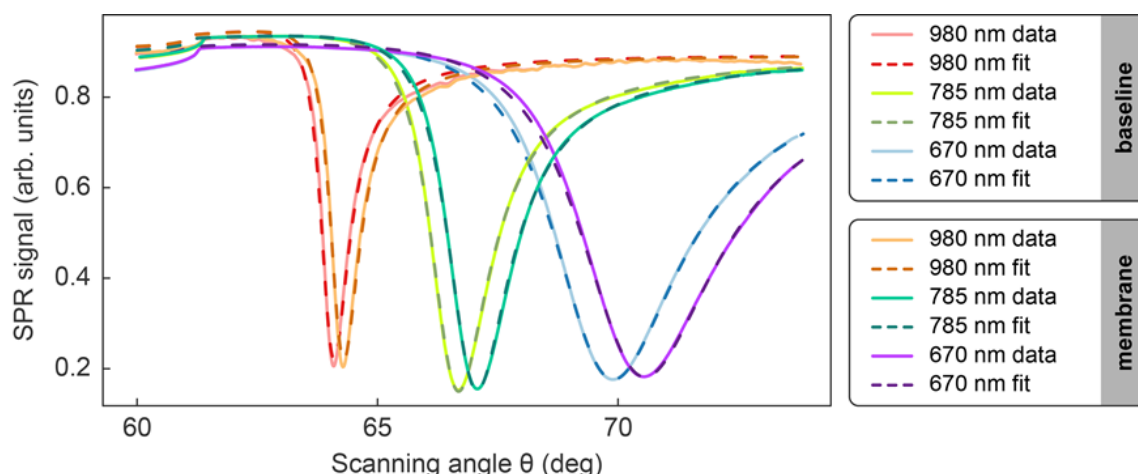
Figure 5:9 SPR measurement for confirming membrane thickness. Angle-scanning SPR signal curves for the three individual laser sources with multi-parametric Bionavis 210A VASA SPR instrument. The formation of the membrane induces a clear shift of the resonance angle in all three measurement channels.

Layer		Support	Au	SiO_2	PBS
n	670 nm	1.5202	0.17215	1.43351	1.33011
	785 nm	1.5162	0.19226	1.45443	1.32887
	980 nm	1.5129	0.26653	1.41842	1.32533
k	670 nm	0	3.86192	0.00213	0.00178
	785 nm	0	4.78515	0.00633	0.00011
	980 nm	0	6.22052	0	0
d (nm)		∞	57.01	10.48	∞

Table 5:1 Model parameters from the baseline measurement (without membrane) establish the properties of the multilayer system. Obtained values show fair agreement with tabulated values for the constituent material components. Values on grey shaded cells indicate parameters which were fixed, and values on orange shaded cells indicate parameters which were set as variables in the calculations.

	Layer	Support	Au	SiO$_2$	DOPC	PBS
n	670 nm	1.5202	0.17215	1.43351	1.45068	1.33011
	785 nm	1.5162	0.19226	1.45443	1.45169	1.32887
	980 nm	1.5129	0.26653	1.41842	1.451	1.32533
k	670 nm	0	3.86192	0.00213	0.00578	0.00178
	785 nm	0	4.78515	0.00633	0.00208	0.00011
	980 nm	0	6.22052	0	0	0
d (nm)		∞	57.01	10.48	5.07	∞

Table 5:2 SPR multilayer model fitting results, membrane. Model parameters for a fully formed supported lipid membrane on the SPR chip. A membrane thickness of 5.07 nm is obtained, indicating the presence of a single bilayer membrane on the surface. Values in grey shaded cells indicate parameters which were fixed, and values on orange shaded cells indicate parameters which were set as variables in the calculations.

5.5.11 Regression Signals for a Variable Surface Density of Streptavidin Molecules

We have replicated the lipid-streptavidin binding experiment in Figure 5:3 for a variable density of streptavidin molecules in the surface. This density has been controlled by modifying the concentration of biotinylated lipid in the membrane, which corresponds to the density of binding site available for streptavidin. As observed in Figure 5:10, the levels reached by the streptavidin regression signals vary accordingly to the biotinylated lipid concentration in the membrane. For a biotinylated lipid concentration of 0 %, 1 % and 5 %, the streptavidin signal values are 0.0, 0.2 and 1.0, demonstrating the direct correlation between streptavidin amount and regression signal. For a streptavidin monolayer, the density of molecules on the surface has been approximated as 5×10^{12} molecules·cm^{-2}.[174] Consequently, we can estimate the amount of bound streptavidin molecules in our experiments as 0, 1×10^{12} and 5×10^{12} molecules·cm^{-2} for the given biotinylated lipid amounts of 0 %, 1 % and 5 %. This result illustrates that the regression signals are able to capture the number of molecules in the sensor surface relative to the density of molecules in the experiment done to obtain the reference spectrum for the same analyte.
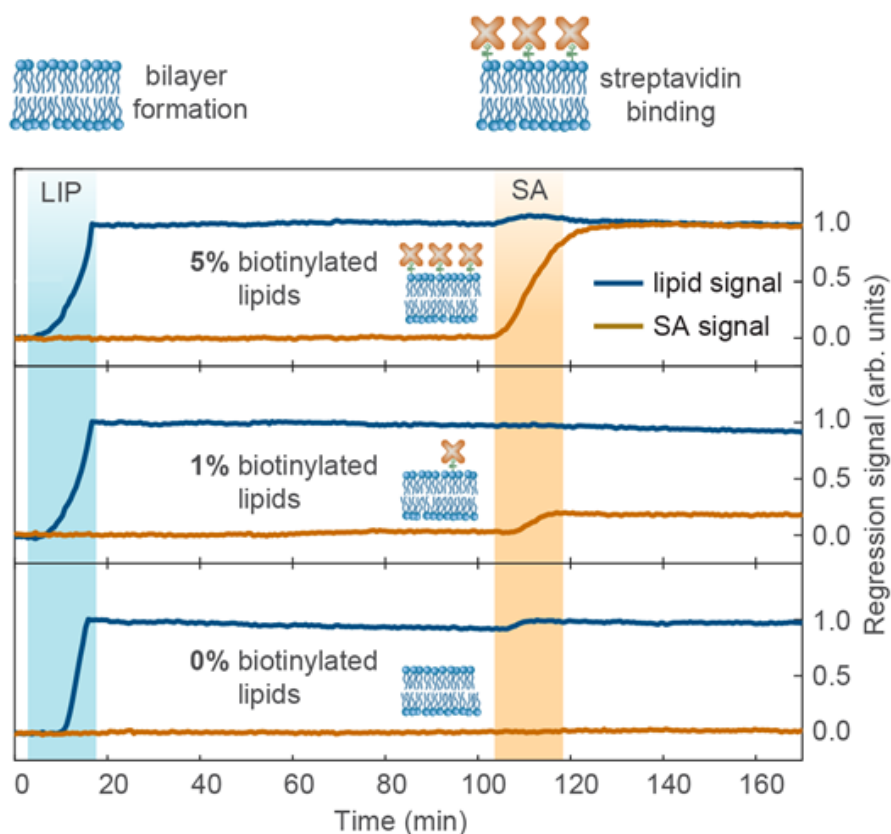
Figure 5:10 Regression signals for a variable surface density of streptavidin molecules.

5.5.12 Principal Component Analysis

The linear regression analysis in the manuscript decomposes the measured time-resolved absorbance spectra into a linear combination of the two reference absorbance spectra for lipid and protein (see, e.g., Figure 5:3). The linear regression results are valid as long as the infrared absorption spectrum of the heterogeneous sample is the addition of the absorption of its individual constituents, a condition that is satisfied in all our experiments and analyte concentrations used.

To confirm that two reference spectra used in the experiment corresponding to Figure 5:3 are sufficient to capture the full biological information contained in our time-dependent measurements, we performed principal component analysis (PCA) over the spectral data for all the time points in the experiment. In the PCA analysis the time-dependent spectra are decomposed into orthogonal spectra (principal components) maximizing the variance for the first principal component (PC1) and iteratively for the next components (PC2, PC3…). In Figure 5:11a we see that the first two principal components account for 99.7 % of the total variance contained in the data, indicating that there are two linearly independent components in our spectral data (lipid and streptavidin). In Figure 5:11b we show the PCA scores representing the time evolution of the experiment. There are three regions in the principal component space where the data points accumulate, which correspond to (a) the start of the experiment with no molecules adsorbed, (b) the lipid membrane and (c) the lipid membrane with immobilized streptavidin. The data points

linking these three regions correspond to the transients when the lipid bilayer is being formed and during the streptavidin binding. The interpretation of principal components is not straightforward in general, however in this case it is clear that the first principal component (PC1) corresponds mainly to the streptavidin spectrum and the second principal component (PC2) corresponds mainly to the lipid spectrum. Additionally, the large variance explained by PC1 (> 80 %) is due to the fact that the lipid injection took place at the beginning of the experiment and only a small fraction of the time points are free of lipids, leaving a relatively small variance for PC2 (lipid).

In addition, we compared the measured spectrum (dashed lines) and the linear regression result (solid lines) in the relevant amide and methylene bands. As an example, we show in Figure 5:11c the comparison for a specific time point after the lipid and streptavidin binding. Agreement between the data sets is excellent, validating the suitability of utilizing a linear regression for analyzing our experimental data. This agreement is not specific to the chosen time point and all other time points show similar agreement between measured data and linear regression results.
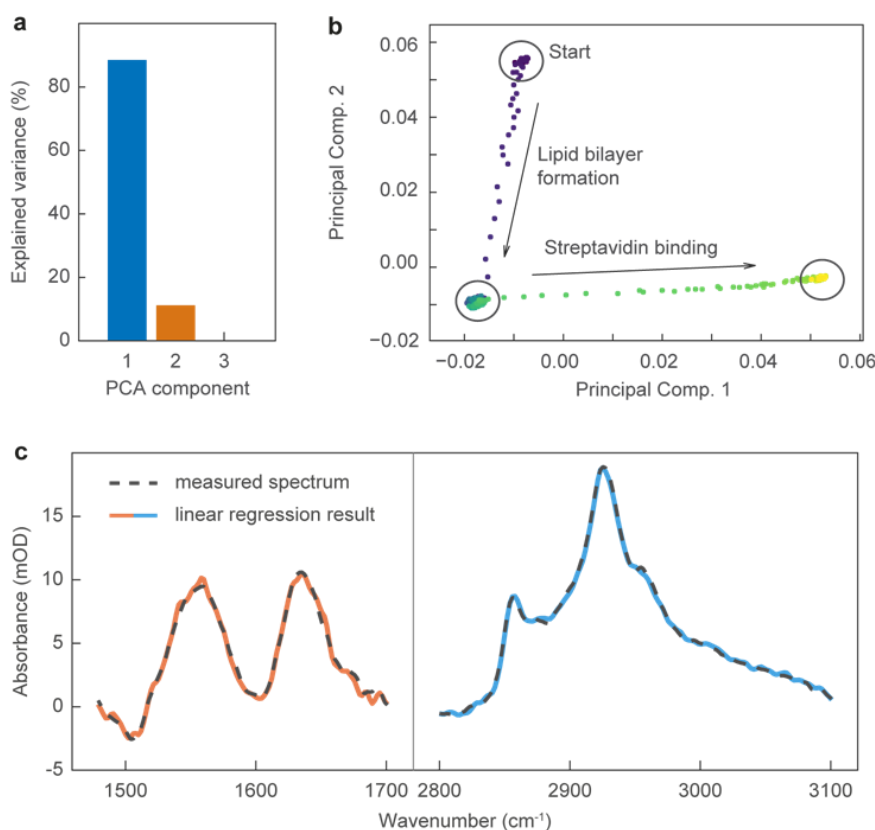
Figure 5:11 Validation of linear regression approach. a) PCA explained variance for the time-resolved absorbance spectra in Figure 5:3e, which confirm the presence of two independent components in the experimental data set. b) PCA scores for the main two principal components obtained from the spectral data over all the time points show the lipid bilayer formation and the melittin binding. c) The measured experimental absorbance spectrum (dashed lines) is in excellent agreement with the linear regression result (solid lines) based on the two reference spectra for lipid and protein.

5.5.13 Bulk Circular Dichroism Measurements of Lipid/Melittin Association

To validate the association of the melittin used in our experiments to the lipid membrane, we performed circular dichroism (CD) measurement in bulk solution. CD spectra were recorded on a Jasco J-815 CD spectrometer operated at 20 °C, and acquired from 195 nm to 250 nm at a scan rate of 50 nm·min⁻¹ and in increments of 0.2 nm. For each sample, five spectra are averaged and smoothed using binomial approximation. The melittin and vesicles concentrations are 20 μM and 1 mg·ml⁻¹, respectively.

Bulk CD results in Figure 5:12 clearly show that the random coil secondary structure of melittin changes into a α-helical conformation in the presence of DOPC lipid vesicles, confirming the efficient association of melittin to the lipid membrane observed in our microfluidic measurements.
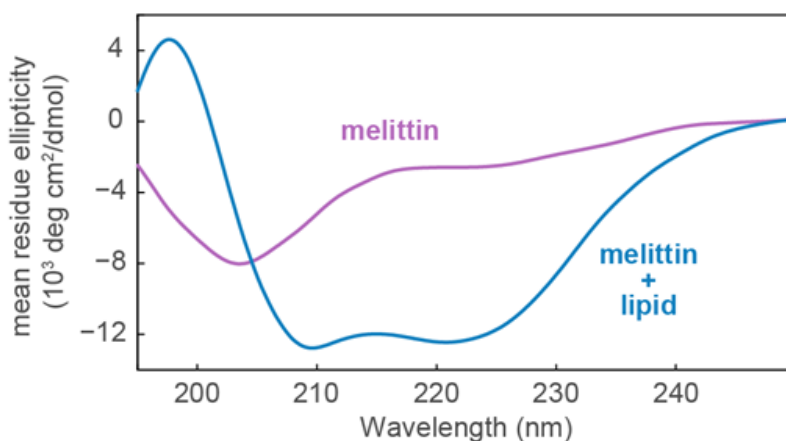
Figure 5:12 Bulk circular dichroism measurements. CD spectra of a melittin solution before (purple line) and after (blue line) the addition of DOPC vesicles clearly show a strong conformational change of the melittin secondary structure, confirming its efficient association with the lipid membrane.

5.5.14 Fluorescence Validation of Melittin-Induced Lipid Membrane Disruption

To confirm the displacement of lipids in the bilayer membrane as a consequence of the injection of melittin (Figure 5:4a) we reproduced the experiment with fluorescently-tagged lipids. To ensure consistency with the presented FTIR results, the same microfluidic setup of PDMS cell and syringe pump is used. The experiments start with the formation of supported lipid bilayer with fluorescence tagged lipids (Texas Red 1,2-dihexadecanoyl-sn-glycero-3-phosphoethanolamine) on the SiO$_2$ coated substrates. Continuous fluorescence images are recorded during bilayer formation and subsequent melittin-induced disruption using a confocal laser-scanning microscope (LSM 700, Zeiss Microscopy) with a 10x objective and analyzed using the Zen software (Zeiss Microscopy). The fluorescence signal is obtained by integrating the fluorescence image over a square region corresponding to an area of approximately 100 μm by 100 μm on the chip. We observed that the arrival of melittin molecules at 100 μM concentration induces a decrease of the fluorescent signal from lipid molecules. The decrease of fluorescent signal is approximately 50 %, which is consistent

with the SEIRAS signals in Figure 5:4a. This strong decrease of the lipid fluorescence contrast to the relatively flat fluorescent signal measured in the absence of melittin.
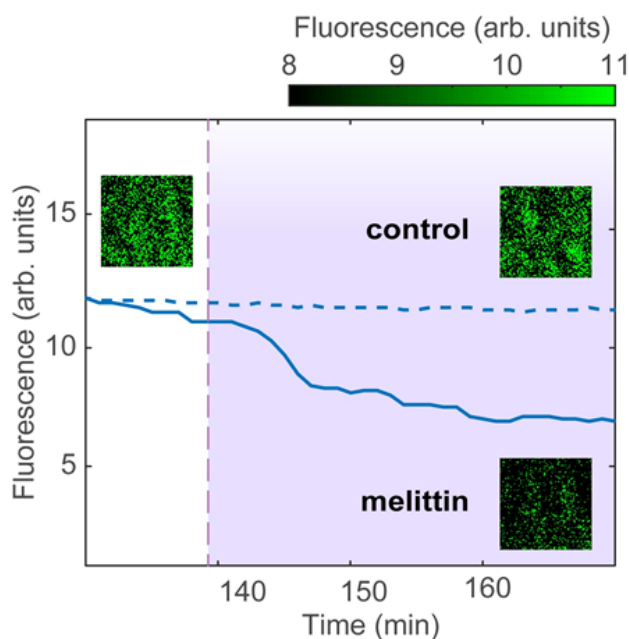
Figure 5:13 Validating fluorescence measurements of the melittin-induced disruption of the lipid membrane using a fluorescently tagged lipid membrane. The decrease in fluorescence signal level produced after the injection of melittin at 100 µM concentration indicates a displacement of lipid molecules upon melittin association, while the control with no melittin results in a flat fluorescence signal.

5.5.15 Linear Regression Reference Spectra for Vesicular Cargo Release Experiment

The vesicular cargo release experiment in Figure 5:4b of the main text includes three significant molecular components: lipid vesicles, melittin, and GABA cargo. The corresponding reference spectra for use in the linear regression analysis were acquired during independent measurements and are shown in Figure 5:14. Significantly, the three reference spectra form a linearly independent set, allowing for the efficient differentiation of the compounds using linear regression analysis.
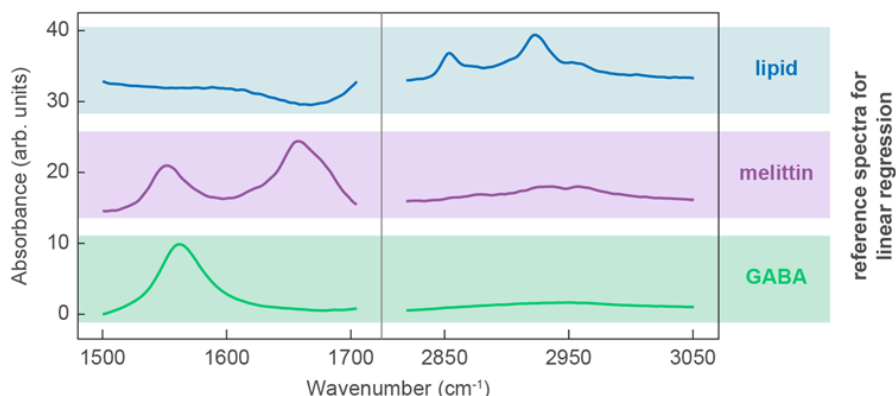
Figure 5:14 Reference spectra for the vesicular cargo release experiment. Reference spectra for the three significant biological components are acquired in separate experiments and demonstrate sufficient linear independence for linear-regression-based chemical discrimination.

5.5.16 GABA Sensing on Functionalized Metasurface

To confirm that the stable GABA regression signal in Figure 5:4b of the main text originates from GABA molecules encapsulated in the lipid vesicles and not from simple adsorption to the sensor metasurface, we flow a large concentration (100 mg·mL^{-1}) of GABA over our sensor metasurface without the presence of any lipid vesicles (Figure 5:15). We observe a strong peak of the GABA regression signal, which disappears completely through continuous washing with running buffer solution. These results show that GABA does not readily adsorb on our sensor metasurface and thus validates that we indeed observe encapsulated GABA molecules in our synaptic vesicle mimic experiment in Figure 5:4b of the main text.
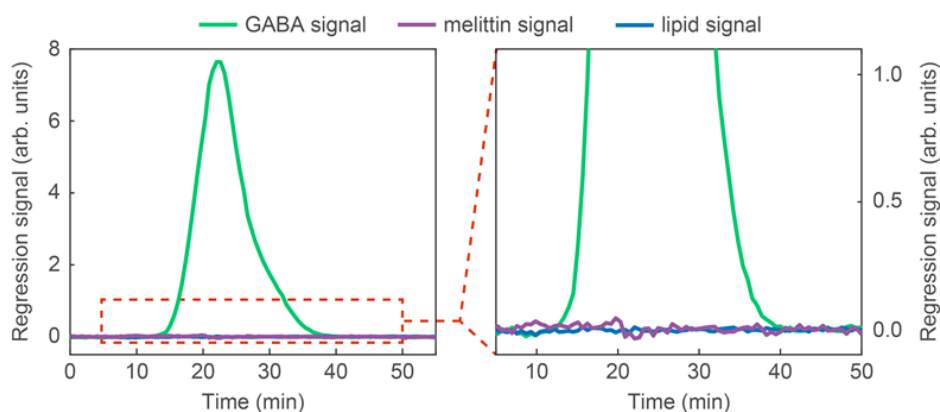
Figure 5:15 GABA adsorption directly on functionalized metasurface. The control experiment is performed by injecting GABA directly on top of the funtionalized metasurface, without encapsulating it in vesicles. We observe a strong peak of the GABA regression signal, which disappears completely through continuous washing with running buffer solution. This behaviour confirms that GABA molecules do not adsorb on the sensor metasurface. For easier comparison, the scale in the right panel is chosen to match the scale in Figure 5:4.

Chapter 6   Infrared Metasurface Augmented by Deep Learning for Monitoring Dynamics between All Major Classes of Biomolecules

This work has been published in Advanced Materials, 2021.

Authors: Aurelian John-Herpin, Deepthy Kavungal, Lea von Mücke and Hatice Altug

Contribution: A. J.-H. designed and performed experiments, designed and numerically simulated metasurfaces, micro-/nano-fabricated chips, carried out data analysis and developed artificial intelligence models, and wrote the manuscript.

Reference: John-Herpin, Aurelian, Deepthy Kavungal, Lea von Mücke, and Hatice Altug. "Infrared Metasurface Augmented by Deep Learning for Monitoring Dynamics between All Major Classes of Biomolecules." Advanced Materials 33, no. 14 (2021): 2006054.

Permission to reproduce the article is granted by Wiley-VCH.

6.1   Abstract

Insights into the fascinating molecular world of biological processes are crucial for understanding diseases, developing diagnostics, and effective therapeutics. These processes are complex as they involve interactions between four major classes of biomolecules, i.e., proteins, nucleic acids, carbohydrates, and lipids, which makes it important to be able to discriminate between all these different biomolecular species. In this work, a deep learning-augmented, chemically-specific nanoplasmonic technique that enables such a feat in a label-free manner to not disrupt native processes is presented. The method uses a highly sensitive multiresonant plasmonic metasurface in a microfluidic device, which enhances infrared absorption across a broadband mid-IR spectrum and in water, despite its strongly overlapping absorption bands. The real-time format of the optofluidic method enables the collection of a vast amount of spectrotemporal data, which allows the construction of a deep neural network to discriminate accurately between all major classes of biomolecules. The capabilities of the new method are demonstrated by monitoring a multistep bioassay containing sucrose- and nucleotides-loaded liposomes interacting with a small, lipid membrane-perforating peptide. It is envisioned that the presented technology will impact the fields of biology, bioanalytics, and pharmacology from fundamental research and disease diagnostics to drug development.

6.2   Introduction

The ability to detect and monitor biomolecules is essential to extend our understanding of biological processes of both physiological and pathological order. Biosensors enabling the analysis of biomolecules from a wide range of samples are indispensable tools for analytical and biochemical studies as well as for medical diagnostics, safety, and industrial applications. In this regard, plasmonic biosensors employing nanoparticles and localized surface plasmon resonances (LSPR) have been receiving significant attention over the years due to their advantages, including high sensitivity and label-free operation.[230] By detecting trace amounts of molecular compounds from minute samples, their use has been shown in various settings including for diagnostics,[231,232] environmental monitoring,[233] food industry,[234] and consumer products.[235] Access to kinetic information at the monolayer level has also been demonstrated with applications in bioanalytics and pharmacology.[236,237] The vast majority of LSPR sensors rely on refractive index change detection, and despite their advantage of high sensitivity, the method is inherently nonspecific and unable to identify the nature of the matter causing the refractive index shift. In order to achieve specificity with selective binding of the targeted analytes, LSPR sensors require biofunctionalization through surface chemistry. However, going beyond the detection of one or two target analytes is very challenging, especially for processes in which the net refractive index remains mostly unchanged due to simultaneously occurring association, dissociation, and removal events, making it difficult to perform accurate measurements and decouple the contribution of the individual analytes from the overall signal.[160] This is where plasmonic biosensors tailored for optical spectroscopy bring unique advantages because nanoantenna sensors can be tuned so that their resonances spectrally match molecular vibrations of analytes of interest, thereby making

chemically specific detection possible.[147,154] While surface-enhanced Raman spectroscopy allows the detection of single molecules due to its extremely tight near-field confinement on the surface (with a decay length of a few nanometers only),[238] SEIRAS nanosensors have a biologically relevant sensing depth (several tens of nanometers), which make it possible to monitor larger entities, such as lipid vesicles interacting with various other biomolecules.[60] These types of biological samples play a pivotal role in numerous physiological and biomedical studies, e.g., in the investigation of exosomes carrying proteins and nucleic acids used for intercellular communication or the characterization of liposomes loaded with drugs such as siRNA to treat pathological conditions.[30,35] SEIRAS using engineered nanoantennas is the ideal candidate for such studies; however, this research field is still in its infancy and several challenges remain to be addressed before a more widespread use can emerge. So far, most of the SEIRAS sensors exhibit narrowband resonances, thereby strongly restricting the number of absorption bands and analytes that can be analyzed. Many of these sensors have been tuned for protein detection via their characteristic Amide I and II absorption bands,[108,144,202,239,240] with some even operating in water and providing information about their 3D structures.[148,162,241,242] Given the importance of proteins in physiology and the challenge of their detection with IR spectroscopy due to the overlap between water and Amide absorption bands, such SEIRAS sensors represent an important milestone. The next challenge is to simultaneously detect different classes of biomolecules, which is complicated due to the broadband nature of IR spectroscopy. For instance, while the Amide I and II bands of proteins absorb around 6 µm, lipids absorb more strongly near 3 µm and nucleic acids and carbohydrates around 10 µm; this demands to have a wide spectral coverage over 7 µm. Multiresonant metasurfaces represent a promising approach to address this challenge by providing several resonances to target spectrally distant absorption bands.[128,134,203,243,244] At the same time, the increased wealth of collected absorption signals and their partial overlap requires the use of chemometrics to effectively discriminate between analytes spectroscopically.[86] Recently, multiple linear regression (MLR) was used to resolve protein–lipid interactions in processes involving lipid vesicles with dual-resonant metasurfaces consisting of plasmonic nanorod antennas.[160] While this approach showed promises, further developments are needed for simultaneous monitoring of a large number of analytes from all four major biomolecular classes without erroneous signal attributions by the readout system.

In this work, we experimentally demonstrate that deep learning empowers broadband plasmonic metasurfaces for SEIRAS by enabling the study of a multianalyte bioparticle system in water and in real-time. The biosample consists of liposome nanoparticles loaded with both sucrose and nucleotides, and upon their binding on the surface of the SEIRAS sensor integrated with microfluidics, we introduce melittin, a small cytolytic peptide, which perforates the lipid membranes of the liposomes. This interaction leads to the breakage of liposomes and dual cargo release as well as the formation of supported lipid bilayer (SLB) patches on the sensor. With our optofluidic biosensor we can resolve in real-time these interaction events between all four major classes of biomolecules without using any external labels. This feat is achieved by engineering a highly sensitive multiresonant metasurface providing large signal enhancements across a broad

mid-IR spectrum ranging from below 1000 to above 3000 cm^{-1} to cover all the major absorption bands of biomolecules. Significantly, the signals from the broadband metasurface is extracted with a deep neural network (DNN) for effective and reliable discrimination between all the simultaneously present biomolecules. By introducing for the first time a deep learning approach to real-time in situ SEIRAS measurements with nanoantennas, we expand the capabilities to new horizons where experiment complexity and training data wealth go hand in hand. Augmenting SEIRAS with deep learning unleashes a vast potential to tap into and provides a powerful tool for unraveling open questions in biology, such the role of exosomes in health and disease.

6.3   Results and Discussion

6.3.1   Multiresonant Metasurface for Broadband Mid-IR Sensing in Aqueous Media

To perform in situ SEIRAS, we nanofabricate gold antenna arrays on a transparent calcium difluoride substrate (Figure 6:1a) and integrate the plasmonic chip in a polydimethylsiloxane (PDMS) microfluidic device so that the incident light comes from the backside of the chip and reflects back to the objective above (Figure 6:1b). In this way, less IR light gets lost due to absorption by water and the analytes flowing through the microfluidic device can be sensed via the evanescent electric fields emanating from the resonant nanoantennas (Figure 6:1c). The nanoantennas are tuned so as to provide three resonances (Figure 6:1d, black and gray curves) which overlap with the molecular vibrations of all the major biological building blocks, i.e., polypeptides, nucleic acids/nucleotides, lipids, and polysaccharides (Figure 6:1d, colored curves). In the experimentally measured reflectance (Figure 6:1d, dotted gray curve), in addition to the three resonance peaks of the nanoantennas, we observe two large reflectance dips caused by the absorption due to water molecule vibrations around 1650 and 3500 cm^{-1}. The numerical simulation (Figure 6:1d, solid black curve) does not feature these water absorption-caused modulations, as the imaginary part of water was not taken into account (k_{water} = 0) to visualize better the antenna resonances. The low-frequency antenna resonance around 1200 cm^{-1} is suitable to sense the strong asymmetric phosphate group stretching vibrations from nucleic acids ($\approx$ 1230 cm^{-1}) as well the characteristic stretching motion of the CO bond within the glycosidic linkage of carbohydrates ($\approx$ 1142 cm^{-1}),[149,245] while the other two resonances around 1600 and 2900 cm^{-1} are tuned to sense the Amide I-II vibrations of proteins ($\approx$ 1650, $\approx$ 1550 cm^{-1}) and methylene stretching vibrations of lipids ($\approx$ 2850, $\approx$ 2920 cm^{-1}), respectively.[160]
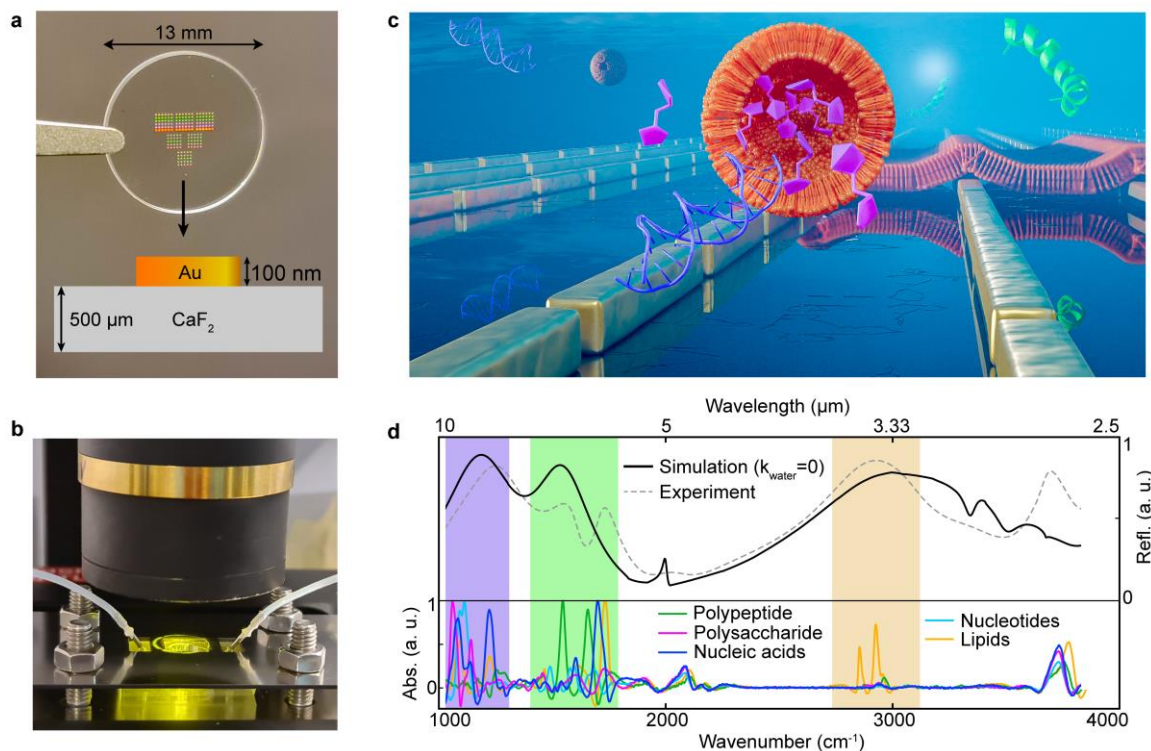
Figure 6:1 Plasmonic chip and its microfluidics integration for bio-experiments in water. a) Top: Top-view picture of a representative plasmonic chip. Bottom: Side view schematic. b) Fluidic setup used for in situ micro-FTIR bioexperiments in water. A plasmonic chip is integrated into a PDMS device clamped below the micro-FTIR objective. c) Artwork showcasing the flow over plasmonic antennas of polypeptides, nucleic acids, lipid vesicles, and polysaccharides. d) Plot displaying the metasurface's numerically simulated (black solid curve) as well as experimentally measured reflectance spectrum in water (gray dotted curve) together with the absorption spectra of five species from all the major classes of biomolecules (colored curves). In the simulation, the imaginary part of water was not taken into account ($k_{water} = 0$) to visualize better the antenna resonances, which are highlighted with colored, shaded areas.

Our nanoplasmonic metasurface is a multiresonant grating order-coupled nanogap (MR-GONG) design based on the recently introduced grating order-coupled nanogap (GONG) antenna arrays.[148] It combines a single resonant array (SR-GONG) with a novel dual resonant array (DR-GONG). Each biochip (Figure 6:1a) contains pairs of $250 \times 250\ \mu m^2$ SR- and DR-GONG arrays separated by $100\ \mu m^2$, which as a whole define a MR-GONG metasurface sensor (Figure 6:2a). In order to spectrally target four different major classes at the same time, we design the three resonances of the metasurface to be at 1200, 1600, and 2900 cm^{-1} by tuning the geometrical parameters of the two types of arrays as seen in Figure 6:2b.
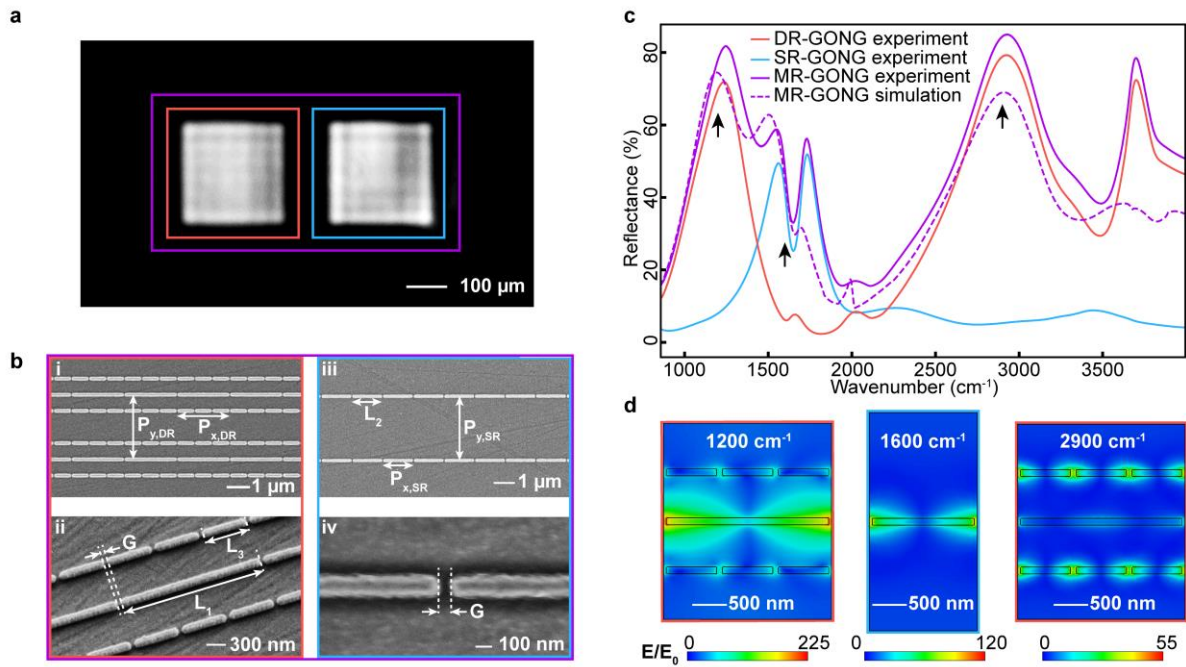
Figure 6:2 MR-GONG metasurface. a) Infrared reflectance microscopy image in dry conditions obtained using quantum cascade laser light at 6 µm wavelength. Two 250×250 µm^2 arrays can be seen with red and blue squares identifying DR- and SR-GONG arrays, respectively. Together, the two arrays form the MR-GONG metasurface indicated with the purple rectangle. b) Scanning electron microscopy (SEM) images of: i) a DR-GONG array with periodicities $P_{x,DR}$ = 2.4 µm and $P_{y,DR}$ = 2.9 µm, and ii) antenna lengths L_1 = 2.32 µm and L_3 = 0.72 µm as well as interantenna gap size G = 80 nm, iii) an SR-GONG array with periodicities $P_{x,SR}$ = 1.58 µm, $P_{y,SR}$ = 3.2 µm and antenna length L_2 = 1.5 µm, and iv) an interantenna gap size G = 80 nm. c) Micro-FTIR measured SR- and DR-GONG arrays in water as well as the combined MR-GONG metasurface reflectance, incl. numerically simulated spectrum. The arrows indicate the spectral positions at which we show d) numerically simulated electric field enhancements around the three resonances in water.

The experimentally measured reflectance spectra from SR-, DR-, and MR-GONG in water match well with the numerical simulations (Figure 6:2c). Here, the imaginary part of the refractive index for water has been used in the simulation to take into account absorption by water. The positions of the grating orders were tuned by the y-periodicities of the arrays to boost the electric near field enhancements around the 1200, 1600, and 2900 cm^{-1} resonances (Figure 6:2d). The maximum near-field intensity enhancement in water surpasses 50 000 for the lower frequency resonance and scales with the third power of the wavelength for the two higher frequency resonances, in accordance with classical antenna theory.[246] The grating order presence can be observed as small modulations in the reflectance spectra at multiple locations, and the most prominent ones are around 2000 and 3800 cm^{-1}.

6.3.2 Multi-Analyte Bio-Experiment with Vesicular Bionanoparticles

Next, we experimentally demonstrate the applicability of the metasurface with a dynamically interacting nanoparticle biosystem (Figure 6:1c), which features multiple different species, including melittin polypeptides and lipid vesicles loaded with nucleotides as well as sucrose

polysaccharides. Successfully resolving the interactions between all these analytes in water medium would open the door to studies with native vesicles, such as exosomes or biomedical liposomes loaded with drugs. To perform real-time in situ SEIRAS measurements, we continuously measure the reflectance spectrum R of the MR-GONG metasurface and compute the absorbance with respect to the initial baseline spectrum R_0 as $-10^3 \cdot \log_{10}(R/R_0)$. The thereby obtained real-time absorbance spectra incorporate the IR signatures of the four analytes (Figure 6:3a). The grayscale color bar in Figure 6:3a represents discrete time points, and the complete spectrotemporal data can be seen in Figure 6:4d as a 3D plot. To identify the contributions of each analyte at different time points, we have initially tested the use of MLR to model the relationship between the overall real-time absorbance signal and the individual analyte absorbance signal contributions by least-squares fitting.
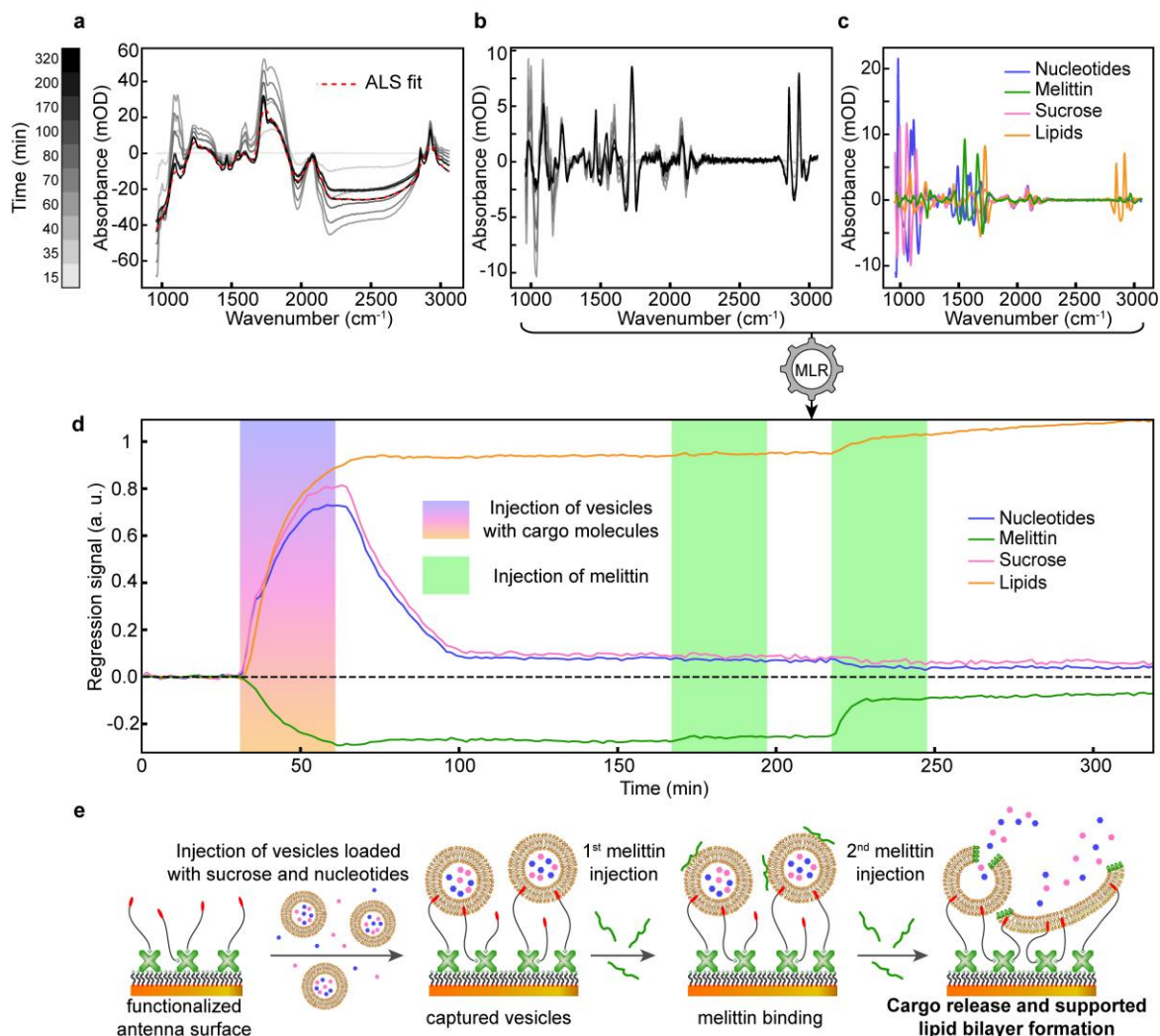
Figure 6:3 Multiple linear regression analysis of dual cargo release bio-experiment. a) Real-time absorbance spectra calculated as $-10^3 \cdot \log_{10}(R/R_0)$ with R the reflectance spectrum of the MR-GONG metasurface and R_0 the baseline reflectance. The asymmetric least squares (ALS) fit for the ultimate spectrum is also shown. The grayscale bar represents discrete time points. b) Absorbance spectra after subtracting the ALS fit for each spectrum. c) Reference absorption spectra for the four bioanalytes used to apply MLR to obtain d) the regression curves of the dynamic experiment involving lipid vesicles, sucrose, nucleotides, and melittin. e) Schematic depiction of the experiment.

SEIRAS spectra typically appear on a skewed baseline (Figure 6:3a) as a consequence of spectral shifting of the antenna resonance wavelengths throughout the experiment, which is due to the effective refractive index change in the antenna vicinity as analytes are introduced. We take this effect into account in the preprocessing of the raw spectra where we subtract an asymmetric least squares (ALS) fit to have the real-time absorbance signals centered around zero (Figure 6:3b). To implement MLR, the resulting spectra (Figure 6:3b) and the reference absorbance spectra of all the analytes present in the experiment (Figure 6:3c) are fed into the model to extract the regression coefficients for each analyte and time point (Figure 6:3d). Most of the substantial absorbance changes (Figure 6:3a,b) happen within the first hour after baseline, i.e., between 30 and 90 min

(Figure 6:3d) and the rest of the experiment features only subtle spectral changes over a longer time window, i.e., from 100 to 320 min. As shown in Figure 6:3e, we start the assay with a plasmonic chip functionalized with biotinylated thiols to which biotinylated vesicle tethers are bound via an intercalated streptavidin layer, which corresponds to the initial stable baseline in Figure 6:3d. Half an hour after the start of the experiment, the lipid, sucrose, and nucleotide signals start to rise, as can be seen in the tricolor shaded area of Figure 6:3d. This corresponds to the injection and capturing of liposomes filled and surrounded with nucleotides and sucrose, as is depicted in Figure 6:3e. Interestingly, this injection also induces a negative melittin curve, although the peptide is only introduced later in the experiment; we will discuss this point later in the text. The liposome capture is followed by the rinsing of the surface with the buffer solution (white shaded areas in Figure 6:3d), leading to the stabilization of the signals at t = 100 min. Specifically, the lipid signal reaches a stable maximum, while the sucrose and nucleotide signals peak before stabilizing above zero. This can be understood with the help of Figure 6:3e schematics, i.e., the loaded liposomes are captured by the surface-displayed tethers, while the extravesicular nucleotide and sucrose molecules gradually rinse off with the flowing buffer. The remaining nucleotide and sucrose signals correspond to the molecules trapped as liposome cargo on the antenna surfaces.

An hour after all the signals have stabilized, we perform the first injection of 3×10^{-6} M cytolytic polypeptide melittin, which results in a slight increase of the melittin curve while the curves of the other analytes remain largely unaffected. It appears that at this concentration melittin binds without forming pores in the membranes[221] composed of 40 mol% 1-palmitoyl-2-oleoyl-sn-glycero-3-phosphocholine (POPC), 20 mol% 1,2-dioleoyl-sn-glycero-3-phosphoethanolamine (DOPE), 20 mol% 1-palmitoyl-2-oleoyl-sn-glycero-3-phospho-l-serine (POPS), and 20 mol% cholesterol. For the second injection at t = 220 min, we increase the melittin concentration to 6×10^{-6} M. At this higher concentration the peptides should breach the lipid membranes and thereby lead to the release of nucleotides and sucrose.[223] However, this is not observed in the MLR sensorgrams, which points toward the limitations of the analysis. Another artefact of the MLR analysis is that before the peptide is even introduced on the sensor, the melittin curve becomes negative after the nanoparticle injection and remains below zero throughout the experiment. We believe that this artefact is mostly caused by the displaced water molecules from the binding of the nanoparticles on the sensors' surface and the overlapping water absorption band with the Amide I band of polypeptides. In addition to the water interference, another complication for the MLR analysis arises from erroneous absorption signals caused by the grating order positions shifting with the change in the effective refractive index within the vicinity of the antennas throughout the experiment. This effect can be clearly visualized in Figure 6:3c, where we detect signal that resembles absorption bands in a spectral window (2000–2200 cm^{-1}), which should normally be transparent. In fact, the origin of this signal can be traced back to the grating orders in that range because their corresponding peaks are observable in the resonance spectrum of the metasurface (Figure 6:1d and Figure 6:2c). Overall, even though the spectral signatures extracted by MLR give some insights into the molecular events happening on the metasurface, it is evident that MLR is

not performing accurately. In fact in comparison to our earlier work with fewer numbers of analytes (i.e., three excluding the water medium),[160] we encounter that MLR is rather simplistic to fully resolve the signals over a broader spectrum when there are more analytes present in the sample simultaneously.

6.3.3   Deep Learning for Improved Discrimination Between Analytes

To address these shortcomings, we develop a DNN to discriminate between different molecular components effectively. In general, deep learning models require a large set of input data to work accurately;[247–249] this is in stark contrast to the MLR approach, which only needed one spectrum per analyte for the input references. These single spectra references (Figure 6:3c) were extracted from additional real-time measurements featuring only one analyte at a time. These measurements can be seen in Figure 6:4a, where we performed three real-time in situ experiments, i.e., one with melittin, one with nucleotides as well as sucrose, and one with empty lipid vesicles. In the first experiment, we flow melittin onto the bare sensing surface while continuously measuring the spectra to obtain a 3D plot of absorbance for each spectral and temporal point. Next, we extract a single spectrum around the time of maximum signal, which we then use as a reference spectrum to get regression coefficients (Figure 6:4b). For the nucleotides and sucrose, we flow the molecules sequentially onto the sensor in a single experiment, as it is visible that these completely rinse off the functionalized surface (Figure 6:4b). Given the real-time format of these measurements, more spectral data are available than the one that is used for the MLR analysis. We utilize all these spectra (Figure 6:4a) as well as their associated regression coefficients (Figure 6:4b) as input to build the DNN. Beyond the data shown in Figure 6:4a,b, we record a total input data set of more than three million spectrotemporal data points, from measurements featuring up to three analytes simultaneously (Figure 6:5a,b), which we use to fit our DNN. The DNN input layer has 1089 nodes to match the wavenumber points of our spectra that spans from 960 to 3060 cm^{-1} with a 4 cm^{-1} resolution, and the output layer has four nodes to match the number of analytes (Figure 6:4c). After training/validating the DNN, we input the data of the experiment with the four analytes (Figure 6:4d) to predict the output weights for each analyte and time point (Figure 6:4e).
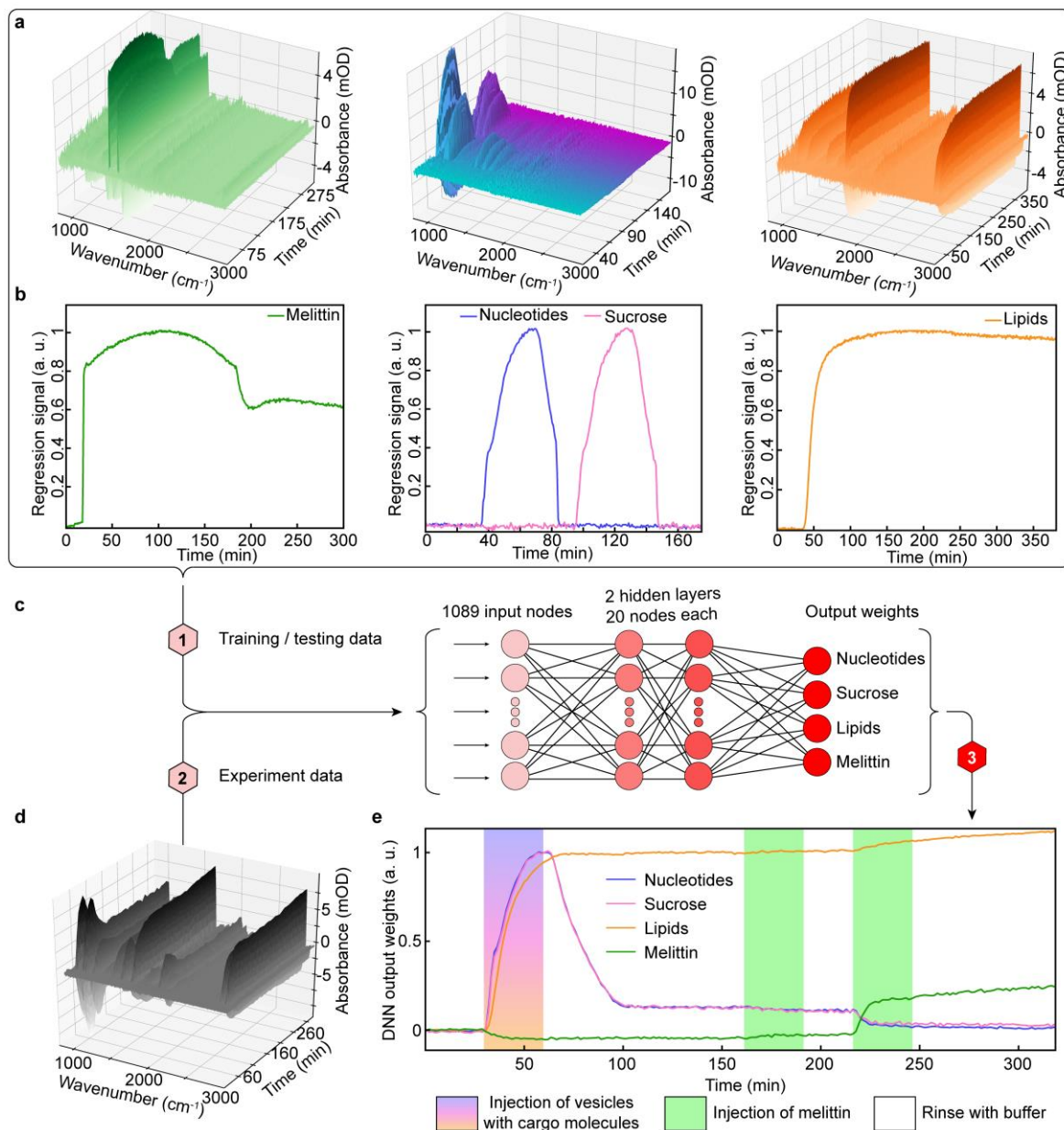
Figure 6:4 Deep learning analysis of dual cargo release bio-experiment. a) From several real-time measurements featuring melittin, nucleotides, sucrose, and lipids, the real-time 3D plots of absorbance signal versus time and wavenumber are extracted, b) as well as the associated regression curves obtained by MLR. c) The absorbance plots together with the associated regression coefficients shown in (a,b) are then used to fit the deep neural network. d) The spectrotemporal data points of the dual cargo release experiment were subsequently fed into the trained network to e) predict the scaled DNN output weight curves for each analyte.S

In Figure 6:4e, we observe the increase of lipid, sucrose, and nucleotide signals after half an hour of baseline as the liposomes and cargo/extravesicular molecules are injected onto the metasurface. At the end of the injection, the lipid signal stabilizes as the liposomes are captured on the surface, while the sucrose and nucleotide molecule signals initially drop as the buffer rinses the molecules off and then stabilize at t = 100 min, corresponding to the signal from the trapped cargo molecules only. In contrast with Figure 6:3d, the melittin signal barely features erroneous

negative values and remains stable around zero before we introduce it onto the surface. Furthermore, as compared to Figure 6:3d, we can see a clear drop in the cargo molecule signals with the second melittin injection, evidencing the content release from the breached liposome membranes. As could already be seen previously in Figure 6:3d, this second melittin injection also leads to a pronounced increase in the lipid curve, which can be understood as the opening of some of the liposomes to form patches of SLBs in closer proximity to the sensing surfaces and thus giving stronger signals (Figure 6:7). This effectively demonstrates the suitability of SEIRAS for sensing small molecules simultaneously with larger structures, such as lipid assemblies, as the antennas' evanescent fields can probe tens of nanometers away from the surface, thereby giving additional information regarding the analyte distribution along the surface normal. It is also important to highlight that the DNN approach helped to effectively reduce the interfering effects of grating orders and water displacement. These results show that the information extracted by the DNN yields superior performance in comparison to using only MLR.

6.4   Conclusion

In conclusion, we have introduced a deep learning-augmented infrared nanoplasmonic metasurface, which is broadly applicable to the study of biomolecular interactions. In addition to the high sensitivity, label-free, and chemical specificity characteristics of the spectroscopic biosensor, we also demonstrated its versatility and universality by simultaneously monitoring major biomolecule classes in water. Significantly, we could observe in real-time vesicle capture, perforation with dual cargo release, and partial transition to planar lipid bilayers. The biosensor offers numerous application prospects, including characterization of liposomal drugs,[250,251] antimicrobial peptides,[252,253] and exosomes.[254,255] Besides biomolecular interactions involving lipid membranes, bioanalytical studies for the characterization of protein-DNA interactions in gene regulation,[256] or protein–polysaccharide interactions in neurodegenerative diseases,[257,258] could also be investigated. The complexity of the tackled bioanalytical studies go hand in hand with the wealth of available DNN training data, which is both a blessing and a curse, as extensive data collection can be tedious but also brings the prospect of eventually unraveling the biomolecular events.[259] Looking forward to future developments, one can envision the adaption of the technology to become compatible with mass-production methods[144,260–262] and miniaturization efforts[158,263–265] for convenient diagnostics and therapeutics. This will probably require a move away from Au as the resonator material, and a Fourier-transform infrared (FTIR) spectroscope as the measurement instrument, because the former is not complementary metal–oxide–semiconductor (CMOS)-compatible and the latter is bulky and expensive. Among the alternatives to Au as the resonator material, CMOS-compatible materials such as Al and Si have shown promising results for SEIRAS via plasmonic and dielectric resonances, respectively.[158,266] As for overcoming FTIR-related limitations, cutting edge measurement tools based on quantum cascade lasers and imaging-based microarrays offer the prospect of biosensor miniaturization.[158,267,268]

6.5 Supplementary Information

6.5.1 Chip Functionalization

The antenna surfaces were first modified ex-situ by incubating them for a minimum of 12 hours in a solution of 2 mM biotinylated thiols (HS-$(CH_2)_{11}$-EG_3-Biotin, ProChimia Surfaces) mixed in a 1:9 ratio with spacer thiols (HS-$(CH_2)_6$-EG_3-OH, ProChimia Surfaces) in ethanol. Subsequent functionalization steps were carried out in situ by injecting 300 µL of 1 µM streptavidin (Thermo Fisher Scientific) followed by 300 µL of 3 µM Biotin-TTCACT-Cholesterol-TEG (IDT). The liposomes were prepared as reported previously.[160] A twofold dilution in PBS of the 2 mg·mL^{-1} liposome solution with 200 mg·mL^{-1} nucleotides and sucrose, respectively, was carried out just before injection into the optofluidic device.

6.5.2 Data Processing and Analysis

The MR-GONG metasurface reflectance spectra are obtained by alternately measuring SR- and DR-GONG arrays and averaging the spectra. The absorbance spectra are then extracted by first dividing the reflectance spectra of the metasurface by that of the bare metasurface baseline before any analyte injection, and then subtracting an asymmetric least squares (ALS) fit.[269] The smoothness and asymmetry parameter pair used is ($5 \cdot 10^3$, 0.5), except for illustrative Figure 6:1d where ($1 \cdot 10^4$, 0.1) was used. The analyte regression signals are obtained by linear least-squares regression of the absorbance spectrum of the heterogeneous solution using as a basis the individual reference spectra of the analytes. Our DNN training/validation data set comprises 3 325 806 spectrotemporal data points obtained from real-time measurements featuring up to three analytes simultaneously, including Figure 6:4a,b and Figure 6:5a,b. We randomly split these data in a 4:1 ratio to define training and validation sets to build a hundred DNN models slightly differing only because of their different random weight initializations. This process is repeated ten times using a different random 4:1 training/validation data set split, and then the results of the 100 x 10 models are averaged. The average learning curves, as well as average standard deviation of the mean (SDM) for each analyte are shown in Figure 6:5c and Figure 6:5d, respectively. To build the DNN models, we use the Sequential model of Python's Keras library, which uses Tensorflow as backend. The "Dense" type layers use ReLU activation functions, and we compile the models with the mean absolute error as the loss function and Adam as the optimizer.[270] The data is fitted using 150 epochs.
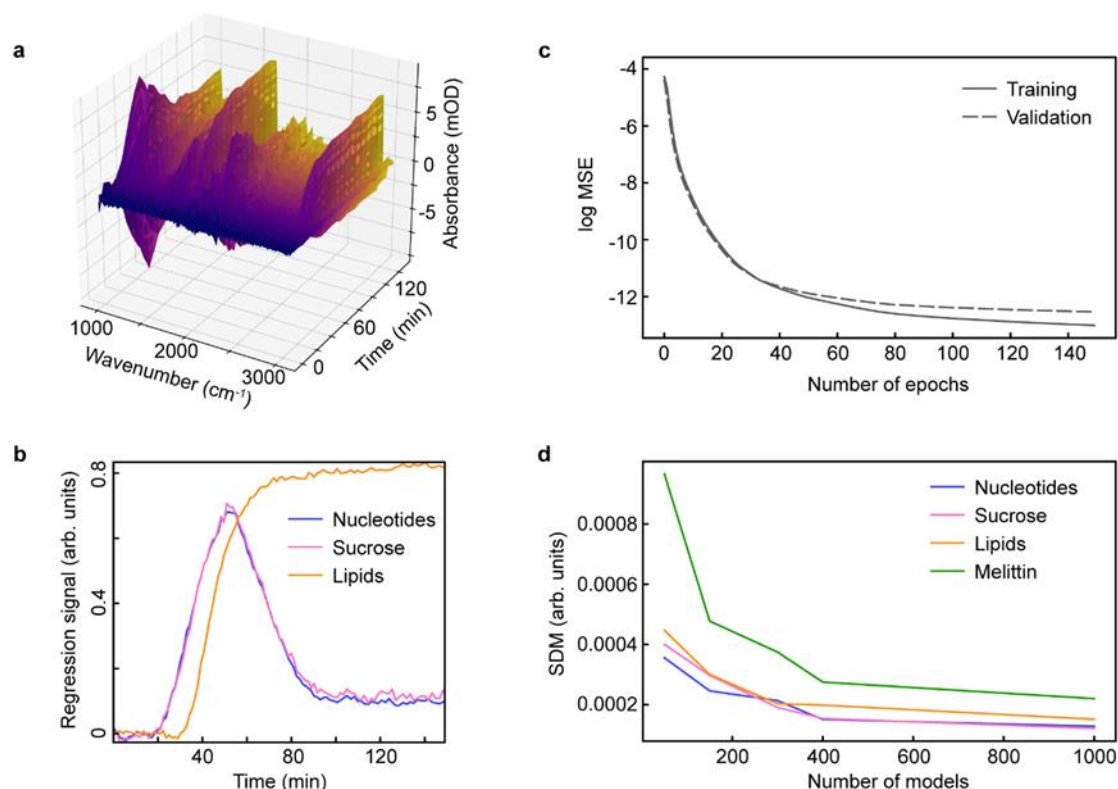
Figure 6:5 DNN training data and model evaluation. a) Real-time 3D plot of absorbance signal versus time and wavenumber b) as well as the associated regression curves obtained by MLR. c) Mean squared error (MSE) of DNN training and validation data fits plotted on a logarithmic scale against the number of epochs. d) Average standard deviation of the mean (SDM) for each analyte DNN output weights against the number of models.

We perform a test experiment where we inject nucleotides and sucrose in different ratios and analyze it with our DNN approach. The output weights (Figure 6:6) are in good agreement with the injected quantities; and therefore validate the capability of the DNN approach to pick out the signals of our cargo molecules, despite their strongly overlapping absorption bands.
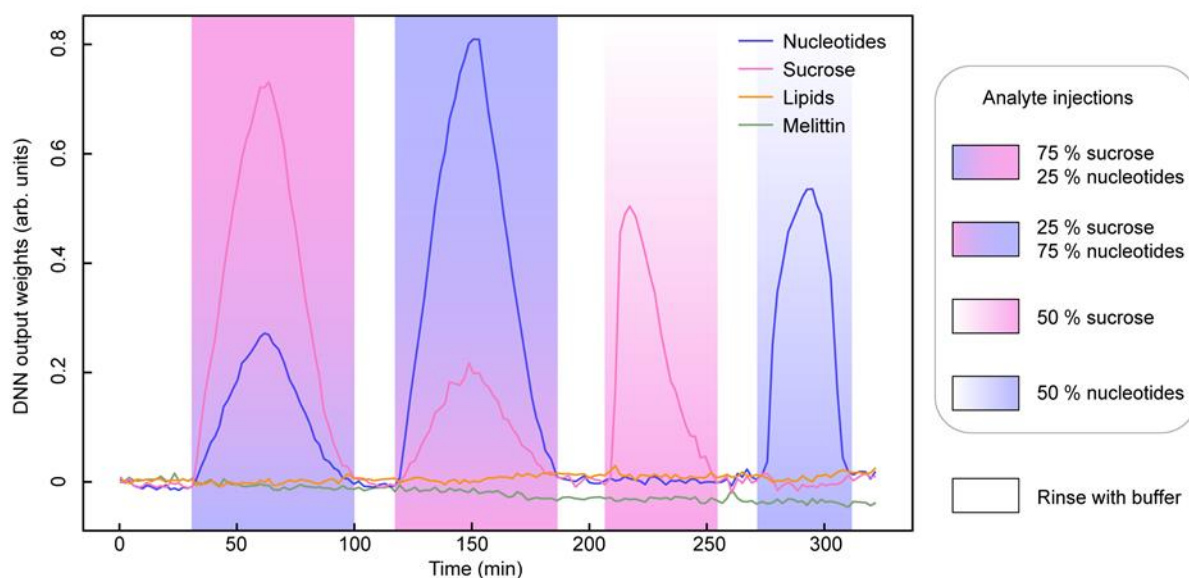
Figure 6:6 DNN output weights for a test experiment with different ratios of sucrose and nucleotides, where 100 % corresponds to 100 mg/mL in PBS buffer.

6.5.3 Fluorescence Measurements

To assess the effect of melittin on the surface-tethered liposomes, we perform fluorescence recovery after photobleaching (FRAP) measurements. The FRAP experiments were carried out with a Zeiss LSM 710 upright confocal microscope and liposomes supplemented with 1 %mol NBD-PC (1-palmitoyl-2-{12-[(7-nitro-2-1,3-benzoxadiazol-4-yl)amino]dodecanoyl}-sn-glycero-3-phosphocholine, Avanti Polar Lipids, Inc.) lipids. The liposomes were attached to a 100 nm gold-coated silicon wafer fragment with surface modifications as used in the SEIRAS experiments. After photobleaching, we observe no recovery of the fluorescence signal, except after incubation with 9 µM melittin, where a small diffusion constant of $0.029 \pm 0.008\ \mu m^2 \cdot s^{-1}$ can be extracted. Data analysis is performed with the FRAP Analyzer program (University of Luxembourg) as described previously.[60,160] As for our SEIRAS measurements, this data supports the likely formation of supported lipid bilayer (SLB) patches after melittin-induced liposome breakage.
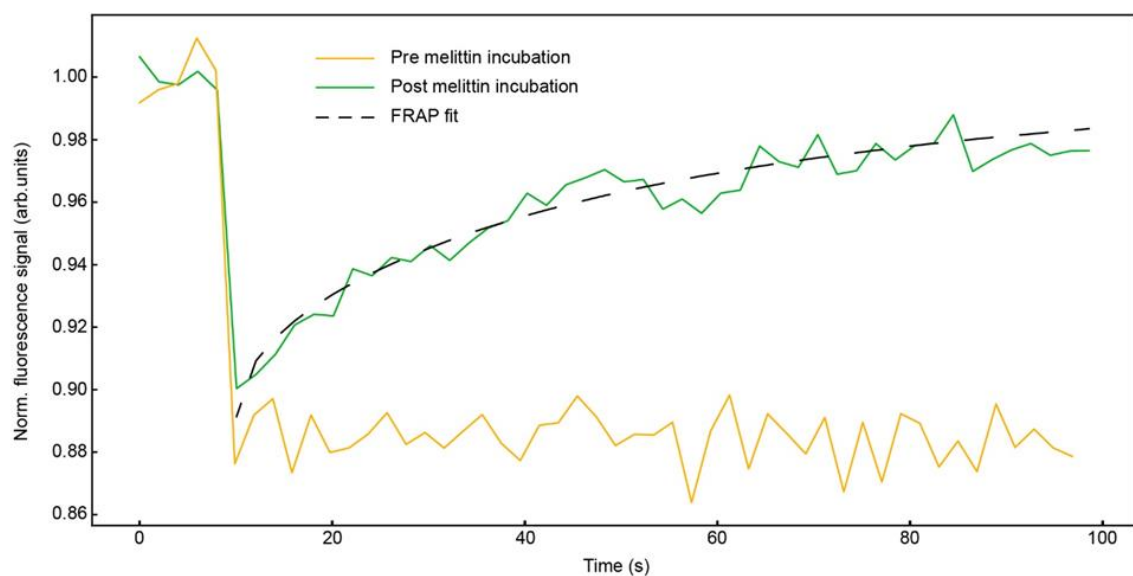
Figure 6:7 Fluorescence recovery after photobleaching (FRAP) measurements. Normalized fluorescence signal before and after incubation of the surface tethered liposomes with melittin. The curves are averaged from two different measurements on different areas, respectively. A fit of the FRAP post melittin incubation is also displayed.

Chapter 7   Conclusion

Parts of this chapter have been adapted from a review published in Angewandte Chemie International Edition.

Authors: Andreas Tittl, Aurelian John-Herpin, Aleksandrs Leitis and Hatice Altug

Contribution: A. J.-H. co-wrote the manuscript.

Reference: Tittl, Andreas, Aurelian John-Herpin, Aleksandrs Leitis, Eduardo R. Arvelo, and Hatice Altug. "Metasurface-based molecular biosensing aided by artificial intelligence." Angewandte Chemie International Edition 58, no. 42 (2019): 14810-14822.

Permission to reproduce the article is granted by American Chemical Society.

In recent years, the field of molecular spectroscopy has seen rapid progress through the introduction of surface-enhanced technologies. Plasmonics has provided a powerful toolkit for concentrating and controlling light at the nanoscale, providing amplified electromagnetic fields for outstanding signal enhancements of targeted analytes. These technologies have opened the door to a plethora of unprecedented applications, such as the label-free monitoring of complex, water-solvated bio-systems and their interaction dynamics. In this thesis, the vast potential of metasurface-enhanced biospectroscopy is unleashed by combining novel single and multiresonant infrared metasurfaces with artificial intelligence methods, including deep neural networks. The thereby created platforms represent new analytical measurement tools for studies in health and disease.

7.1   Achieved Results

We have developed three different nanoplasmonic metasurfaces coupled to three different types of data analysis methods to explore and push the limits of metasurface-enhanced mid-IR biospectroscopy.

In the first original contribution, we introduce grating order-coupled nanogap (GONG) antenna arrays, which achieve extremely high electric field intensity enhancement values of up to five orders of magnitude. This is enabled by combining two sensitivity enhancement principles into one congruent plasmonic design. The first sensitivity-boosting strategy taps into nanogaps to create hotspots for strong light-matter interactions. The second strategy uses the coupling to the grating orders to optimally benefit from constructively interfering electric fields from resonators in an array. The asymmetrical tuning of the array periodicities was the key to create these GONG sensors. Nanogaps with sizes down to 32 nm were fabricated with electron beam lithography to provide protein-accessible hotspots. The performance of the GONG sensors has been benchmarked with extensive numerical simulations and bio-experiments in both dry and aqueous medium conditions. In dry conditions, the detection limit was found to be down to two proteins per nanogap. In aqueous solution, proteins could be detected in real-time and chemically specifically at concentrations down to picograms per milliliter, outclassing traditional mid-IR spectroscopy by orders of magnitudes. Furthermore, by applying data analysis methods based on the Savitzky-Golay filter and nonlinear least-squares fitting, secondary structure motifs of proteins could be detected down to concentrations in the nanograms per milliliter range. Analytical tools for assessing the three-dimensional structure of proteins are essential to health and disease, as the structures are linked to the proteins' functionality and possible pathological behavior.

In the second original contribution, we introduce a dual-resonant metasurface based on a self-similar nanoantenna array design. The far-field resonances are of similar amplitude and tuned to overlap with the characteristic absorption bands of proteins and lipids. Protein-lipid interactions are crucial to physiological processes such as intercellular communication, and we demonstrate that we can resolve them with our platform. We show this using bio-experiments featuring

liposomes and peptides dynamically interacting on the metasurfaces. In one experiment, we monitor the formation of supported lipid bilayers followed by their disintegration by the action of cytolytic peptides. In another experiment, we resolve the neurotransmitter release from synaptic vesicle mimics perforated by the toxic peptides. Resolving these mass-preserving processes represents a remarkable feat that could not be achieved with established label-free sensors such as surface plasmon resonance (SPR) and quartz crystal microbalance (QCM) sensors. This achievement is enabled by coupling our dual-resonant metasurfaces with machine learning algorithms and custom microfluidic devices.

In the third and final original contribution, we developed a triple-resonant metasurface based on the previously introduced GONG design concept. The three resonances provide broadband signal enhancement from around 3 to 10 μm over the entire mid-IR range to overlap with the fingerprint-like absorption bands of different analytes from all four major biomolecule classes, i.e., nucleic acids, carbohydrates, proteins, and lipids. We showcase the ability of our sensor to resolve interactions between all the classes simultaneously by integrating the chip in a microfluidic device and carrying out real-time experiments with exosome-like bionanoparticles loaded with carbohydrates and nucleotides. We successfully track the dual cargo release from the vesicles breached by the injection and binding of toxic peptides. The accurate discrimination between analytes is enabled by the extensive collection of absorption bands across the mid-IR range and a deep neural network model, which we built to handle the complexity of this dynamic bio-system. The introduction of this universal biomolecule sensor based on mid-IR metasurfaces and deep learning provides a potent new analytical measurement tool for applications ranging from pharmaceutical drug development to the unraveling of cellular processes.

7.2   Future Developments

Our mid-IR metasurface sensors are timely and provide significant advancements in the field of biomolecule sensing. Nonetheless, as with any technology, some limitations remain to be overcome. For example, the use of sizable FTIR spectrometers and optical components hinders the portability and accessibility of our sensors. Moreover, mass-production of our sensors would further open the path towards their widespread application, but our current use of non-CMOS-compatible gold as the resonator material impedes this prospect.

The capability of real-time measurements is a significant advantage of our sensors, as they provide vital information about biological systems. Nevertheless, our temporal resolution is not suitable for resolving fast biomolecular interactions in the microsecond range.

Fortunately, as discussed below in more detail, the development of novel surface-enhanced molecular spectroscopy technologies is currently the subject of immense interest. This demonstrated by the emergence of a new generation of metasurface-based biospectroscopies that use novel sensing schemes, various materials, and advanced artificial intelligence implementations to reach new functionalities and application prospects. Though these advanced metasurface

approaches are still in their infancy, they present exciting opportunities to further the research and overcome challenges, including those listed above.

7.2.1   New Materials for Advancing Metasurface-based Mid-IR Spectroscopy

2D materials such as graphene offer exciting possibilities for SEIRA as they provide plasmonic resonances in the mid-IR with extreme near-field confinements,[89] enabling the detection of very small analytes such as volatile organic compounds in gas sensors.[271] Furthermore, their electronic properties have allowed novel functionalities such as voltage-controlled resonance tuning and dielectrophoretic analyte trapping for advanced biomolecule sensing.[202,272] The mechanically flexible nature of these materials could also be used for flexible bioelectronic sensor technologies.[273]

CMOS-compatible resonator materials like aluminum or silicon have excellent prospects for SEIRA as they bring a range of new opportunities. Aluminum is a low-cost and highly abundant material capable of supporting plasmonic resonances over a vast spectral range spanning from the UV to the IR.[155,266,274,275] Unlike gold, it rapidly oxidizes, but the oxide layer is so thin (3-5 nm) that it only minimally buries the evanescent field available for sensing. Furthermore, this Al_2O_3 layer acts as a protective layer against corrosion and can also be readily functionalized for biosensing applications.[239] Its compatibility with wafer-scale fabrication could enable the mass-production of metasurface-based SEIRA chips for disposable diagnostic devices. Silicon benefits from the same CMOS-compatibility aspects, but silicon is not a plasmonic material in contrast to aluminum. Nevertheless, dielectric materials such as silicon and germanium have recently attracted much attention due to their ability to support resonances that can reach very high quality factors (high Q-factors), e.g., by supporting quasi-bound states in the continuum (quasi-BIC).[276] The high Q-factor of dielectric resonators enables new functionalities such as spectroscopy without bulky FTIR spectrometers, thereby paving the way for the miniaturization of SEIRA sensors.[158,264]

7.2.2   Sensor Miniaturization

High Q-factor dielectrics are not the sole enablers of miniaturization, and other emerging developments are playing key roles. Coupling the light from the source to the SEIRA resonators typically requires bulky optics such as reflective Cassegrain objectives. Besides this setup's relatively large space requirement, the coupling of light is also relatively inefficient due to the size mismatch between the micrometer-large light spot and the nanometer-sized resonators. These limitations can be overcome with on-chip light sources and waveguides to provide efficient light coupling and a considerably reduced setup footprint.[277] The recent development of light sources such as quantum cascade lasers (QCLs) is particularly appealing, and their high brilliance enables the use of resonator arrays with minimal footprints. The integration of nanoantenna resonators with waveguide photonics represents a promising strategy for the miniaturization of SEIRA sensor technologies.[263]

7.2.3   A New Era for Metasurface-based Mid-IR Biospectroscopy

QCLs are also extremely interesting for hyperspectral imaging in the mid-IR; they enable chemical imaging of biosamples such as tissues and fluids using fast uncooled detectors with a large field of view (FOV), outclassing traditional FTIR instruments.[278] Furthermore, QCL-based frequency combs represent yet another mid-IR spectroscopy revolution by improving temporal resolution by orders of magnitudes to enable microsecond-resolved measurements at high signal-to-noise ratio (SNR).[279,280] Coupling all these benefits with highly sensitive metasurfaces integrated into advanced microfluidics will generate an incredible wealth of data with a high SNR and outstanding temporal, spatial, and spectral resolution. We can envision that these large data cubes will be combined with advanced artificial intelligence models to usher in a new era for biospectroscopy.

References

1   Moran LA, Horton RA, Scrimgeour KG, Perry MD. *Principles of biochemistry*. 5th ed. Pearson, 2012.

2   Rudd PM, Elliot T, Cresswell P, Wilson IA, Dwek RA. Glycosylation and the Immune System. *Science (80-)* 2001; **291**: 2370–2376.

3   Kaczanowska M, Rydén-Aulin M. Ribosome Biogenesis and the Translation Process in Escherichia coli. *Microbiol Mol Biol Rev* 2007; **71**: 477–494.

4   Cui J, Li F, Shi Z-L. Origin and evolution of pathogenic coronaviruses. *Nat Rev Microbiol* 2019; **17**: 181–192.

5   O'Connor CM, Adams JU, Fairman J. *Essentials of cell biology*. 1st ed. NPG Education: Cambridge, MA, 2010http://portal.acm.org/citation.cfm?doid=634067.634339.

6   Martino F, Perestrelo AR, Vinarský V, Pagliari S, Forte G. Cellular Mechanotransduction: From Tension to Function. *Front Physiol* 2018; **9**: 1–21.

7   Harris NJ, Charalambous K, Findlay HE, Booth PJ. Lipids modulate the insertion and folding of the nascent chains of alpha helical membrane proteins. *Biochem Soc Trans* 2018; **46**: 1355–1366.

8   Chaturvedi D, Mahalakshmi R. Transmembrane β-barrels: Evolution, folding and energetics. *Biochim Biophys Acta - Biomembr* 2017; **1859**: 2467–2482.

9   Hipp MS, Kasturi P, Hartl FU. The proteostasis network and its decline in ageing. *Nat Rev Mol Cell Biol* 2019; **20**: 421–435.

10   Hershko A, Ciechanover A. The ubiquitin system. *Annu Rev Biochem* 1998; **67**: 425–479.

11   Nandi D, Tahiliani P, Kumar A, Chandu D. The ubiquitin-proteasome system. *J Biosci* 2006; **31**: 137–155.

12   Mann M, Jensen ON. Proteomic analysis of post-translational modifications. *Nat Biotechnol* 2003; **21**: 255–261.

13   Narita T, Weinert BT, Choudhary C. Functions and mechanisms of non-histone protein acetylation. *Nat Rev Mol Cell Biol* 2019; **20**: 156–174.

14   Ardito F, Giuliani M, Perrone D, Troiano G, Muzio L Lo. The crucial role of protein phosphorylation in cell signaling and its use as targeted therapy (Review). *Int J Mol Med* 2017; **40**: 271–280.

15   Tenreiro S, Eckermann K, Outeiro TF. Protein phosphorylation in neurodegeneration: friend or foe? *Front Mol Neurosci* 2014; **7**: 42.

16   Manning JC, Romero A, Habermann FA, García Caballero G, Kaltner H, Gabius H-J. Lectins: a primer for histochemists and cell biologists. *Histochem Cell Biol* 2017; **147**: 199–222.

17   Tabatabaei M, Wallace GQ, Caetano FA, Gillies ER, Ferguson SSG, Lagugné-Labarthet F. Controlled positioning of analytes and cells on a plasmonic platform for glycan sensing using surface enhanced Raman spectroscopy. *Chem Sci* 2016; **7**: 575–582.

18   Reily C, Stewart TJ, Renfrow MB, Novak J. Glycosylation in health and disease. *Nat Rev Nephrol* 2019; **15**: 346–366.

19   Bastide A, David A. Interaction of rRNA with mRNA and tRNA in Translating Mammalian Ribosome:

Functional Implications in Health and Disease. *Biomolecules* 2018; **8**: 100.

20   Lyko F. The DNA methyltransferase family: a versatile toolkit for epigenetic regulation. *Nat Rev Genet* 2018; **19**: 81–92.

21   Pfeifer G. Defining Driver DNA Methylation Changes in Human Cancer. *Int J Mol Sci* 2018; **19**: 1166.

22   Harayama T, Riezman H. Understanding the diversity of membrane lipid composition. *Nat Rev Mol Cell Biol* 2018; **19**: 281–296.

23   Patching SG. Glucose Transporters at the Blood-Brain Barrier: Function, Regulation and Gateways for Drug Delivery. *Mol Neurobiol* 2017; **54**: 1046–1077.

24   Pivovarov AS, Calahorro F, Walker RJ. Na+/K+-pump and neurotransmitter membrane receptors. *Invertebr Neurosci* 2019; **19**: 1.

25   Gomes J, Lucien F, Cooper T, Kim Y, Williams K, Liao X *et al.* Analytical Considerations in Nanoscale Flow Cytometry of Extracellular Vesicles to Achieve Data Linearity. *Thromb Haemost* 2018; **118**: 1612–1624.

26   Raposo G, Stoorvogel W. Extracellular vesicles: Exosomes, microvesicles, and friends. *J Cell Biol* 2013; **200**: 373–383.

27   Qu L, Akbergenova Y, Hu Y, Schikorski T. Synapse-to-synapse variation in mean synaptic vesicle size and its relationship with synaptic morphology and function. *J Comp Neurol* 2009; **514**: 343–352.

28   Kaeser PS, Regehr WG. The readily releasable pool of synaptic vesicles. *Curr Opin Neurobiol* 2017; **43**: 63–70.

29   Valencia K, Montuenga LM. Exosomes in Liquid Biopsy: The Nanometric World in the Pursuit of Precision Oncology. *Cancers (Basel)* 2021; **13**: 2147.

30   Kalluri R, LeBleu VS. The biology, function, and biomedical applications of exosomes. *Science (80-)* 2020; **367**: eaau6977.

31   Hofmann L, Ludwig S, Vahl JM, Brunner C, Hoffmann TK, Theodoraki M-N. The Emerging Role of Exosomes in Diagnosis, Prognosis, and Therapy in Head and Neck Cancer. *Int J Mol Sci* 2020; **21**: 4072.

32   Sercombe L, Veerati T, Moheimani F, Wu SY, Sood AK, Hua S. Advances and Challenges of Liposome Assisted Drug Delivery. *Front Pharmacol* 2015; **6**: 1–13.

33   Bulbake U, Doppalapudi S, Kommineni N, Khan W. Liposomal Formulations in Clinical Use: An Updated Review. *Pharmaceutics* 2017; **9**: 12.

34   Filipczak N, Pan J, Yalamarty SSK, Torchilin VP. Recent advancements in liposome technology. *Adv Drug Deliv Rev* 2020; **156**: 4–22.

35   Ickenstein LM, Garidel P. Lipid-based nanoparticle formulations for small molecules and RNA drugs. *Expert Opin Drug Deliv* 2019; **16**: 1205–1226.

36   Yonezawa S, Koide H, Asai T. Recent advances in siRNA delivery mediated by lipid-based nanoparticles. *Adv Drug Deliv Rev* 2020; **154**: 64–78.

37   Syedmoradi L, Daneshpour M, Alvandipour M, Gomez FA, Hajghassem H, Omidfar K. Point of care testing: The impact of nanotechnology. *Biosens Bioelectron* 2017; **87**: 373–387.

38   Nayak S, Blumenfeld NR, Laksanasopin T, Sia SK. Point-of-Care Diagnostics : Recent Developments in a Connected Age. 2017; **89**: 102–123.

39   Yüce M, Filiztekin E, Özkaya KG. COVID-19 diagnosis — A review of current methods. *Biosens*

Bioelectron 2021; **172**: 112752.

40   Toptan T, Eckermann L, Pfeiffer AE, Hoehl S, Ciesek S, Drosten C *et al.* Evaluation of a SARS-CoV-2 rapid antigen test : Potential to help reduce community spread ? *J Clin Virol* 2021; **135**: 104713.

41   McKeating KS, Aubé A, Masson J-F. Biosensors and nanobiosensors for therapeutic drug and response monitoring. *Analyst* 2016; **141**: 429–449.

42   Yu D, Blankert B, Viré J, Kauffmann J. Biosensors in Drug Discovery and Drug Analysis. *Anal Lett* 2005; **38**: 1687–1701.

43   Olaru A, Bala C, Jaffrezic-Renault N, Aboul-Enein HY. Surface Plasmon Resonance (SPR) Biosensors in Pharmaceutical Analysis. *Crit Rev Anal Chem* 2015; **45**: 97–105.

44   Gonçalves A, Pedro A, Santos F, Martins L, Maia C, Queiroz J *et al.* Trends in Protein-Based Biosensor Assemblies for Drug Screening and Pharmaceutical Kinetic Studies. *Molecules* 2014; **19**: 12461–12485.

45   Zhao Y, Kankala R, Wang S-B, Chen A-Z. Multi-Organs-on-Chips: Towards Long-Term Biomedical Investigations. *Molecules* 2019; **24**: 675.

46   Dewey JA, Dickinson BC. *Split T7 RNA polymerase biosensors to study multiprotein interaction dynamics*. 1st ed. Elsevier Inc., 2020 doi:10.1016/bs.mie.2020.04.047.

47   Pipchuk A, Yang X. Using Biosensors to Study Protein–Protein Interaction in the Hippo Pathway. *Front Cell Dev Biol* 2021; **9**: 1–8.

48   Maerkl SJ, Quake SR. A Systems Approach to Measuring the Binding Energy Landscapes of Transcription Factors. *Science (80-)* 2007; **315**: 233–237.

49   Xiao T, Wu F, Hao J, Zhang M, Yu P, Mao L. In Vivo Analysis with Electrochemical Sensors and Biosensors. *Anal Chem* 2017; **89**: 300–313.

50   McLamore ES, Mohanty S, Shi J, Claussen J, Jedlicka SS, Rickus JL *et al.* A self-referencing glutamate biosensor for measuring real time neuronal glutamate flux. *J Neurosci Methods* 2010; **189**: 14–22.

51   Kilic T, Erdem A, Ozsoz M, Carrara S. microRNA biosensors: Opportunities and challenges among conventional and commercially available techniques. *Biosens Bioelectron* 2018; **99**: 525–546.

52   Johnson BN, Mutharasan R. Biosensor-based microRNA detection: techniques, design, performance, and challenges. *Analyst* 2014; **139**: 1576.

53   Udugama B, Kadhiresan P, Kozlowski HN, Malekjahani A, Osborne M, Li VYC *et al.* Diagnosing COVID-19: The Disease and Tools for Detection. *ACS Nano* 2020; **14**: 3822–3835.

54   Seydack M. Nanoparticle labels in immunosensing using optical detection methods. *Biosens Bioelectron* 2005; **20**: 2454–2469.

55   Belushkin A, Yesilkoy F, Altug H. Nanoparticle-Enhanced Plasmonic Biosensor for Digital Biomarker Detection in a Microarray. *ACS Nano* 2018; **12**: 4453–4461.

56   Tenaglia E, Ferretti A, Decosterd LA, Werner D, Mercier T, Widmer N *et al.* Comparison against current standards of a DNA aptamer for the label-free quantification of tobramycin in human sera employed for therapeutic drug monitoring. *J Pharm Biomed Anal* 2018; **159**: 341–347.

57   Garçon L-A, Genua M, Hou Y, Buhot A, Calemczuk R, Livache T *et al.* A Versatile Electronic Tongue Based on Surface Plasmon Resonance Imaging and Cross-Reactive Sensor Arrays—A Mini-Review. *Sensors* 2017; **17**: 1046.

58   Brenet S, John-Herpin A, Gallat F-X, Buhot A, Livache T, Herrier C *et al.* Development of a novel

multiplexed optoelectronic nose for analysis of volatile organic compounds. In: *2017 ISOCS/IEEE International Symposium on Olfaction and Electronic Nose (ISOEN)*. IEEE, 2017, pp 1–3.

59   Brenet S, John-Herpin A, Gallat F-X, Musnier B, Buhot A, Herrier C *et al.* Highly-Selective Optoelectronic Nose Based on Surface Plasmon Resonance Imaging for Sensing Volatile Organic Compounds. *Anal Chem* 2018; **90**: 9879–9887.

60   Limaj O, Etezadi D, Wittenberg NJ, Rodrigo D, Yoo D, Oh S *et al.* Infrared Plasmonic Biosensor for Real-Time and Label-Free Monitoring of Lipid Membranes. *Nano Lett* 2016; **16**: 1502–1508.

61   Soler M, Li X, John-Herpin A, Schmidt J, Coukos G, Altug H. SI: Two-Dimensional Label-Free Affinity Analysis of Tumor-Specific CD8 T Cells with a Biomimetic Plasmonic Sensor. *ACS Sensors* 2018; **3**: 2286–2295.

62   Husale BS, Sahoo S, Radenovic A, Traversi F, Annibale P, Kis A. ssDNA Binding Reveals the Atomic Structure of Graphene. *Langmuir* 2010; **26**: 18078–18082.

63   Bhalla N, Jolly P, Formisano N, Estrela P. Introduction to biosensors. *Essays Biochem* 2016; **60**: 1–8.

64   Nirschl M, Reuter F, Vörös J. Review of Transducer Principles for Label-Free Biomolecular Interaction Analysis. *Biosensors* 2011; **1**: 70–92.

65   Lim HJ, Saha T, Tey BT, Tan WS, Ooi CW. Quartz crystal microbalance-based biosensors as rapid diagnostic devices for infectious diseases. *Biosens Bioelectron* 2020; **168**: 112513.

66   Homola J. Surface Plasmon Resonance Sensors for Detection of Chemical and Biological Species. *Chem Rev* 2008; **108**: 462–493.

67   Koczula KM, Gallotta A. Lateral flow assays. *Essays Biochem* 2016; **60**: 111–120.

68   Ferreira GNM, Da-Silva A-C, Tomé B. Acoustic wave biosensors: physical models and biological applications of quartz crystal microbalance. *Trends Biotechnol* 2009; **27**: 689–697.

69   Zhao J, Huvent I, Lippens G, Eliezer D, Zhang A, Li Q *et al.* Glycan Determinants of Heparin-Tau Interaction. *Biophys J* 2017; **112**: 921–932.

70   Sekhar A, Kay LE. An NMR View of Protein Dynamics in Health and Disease. *Annu Rev Biophys* 2019; **48**: 297–319.

71   Ranjbar B, Gill P. Circular Dichroism Techniques: Biomolecular and Nanostructural Analyses- A Review. *Chem Biol Drug Des* 2009; **74**: 101–120.

72   Borbat PP, Costa-Filho AJ, Earle KA, Moscicki JK, Freed JH. Electron Spin Resonance in Studies of Membranes and Proteins. *Science (80-)* 2001; **291**: 266–269.

73   Kneipp K, Kneipp H, Itzkan I, Dasari RR, Feld MS. Ultrasensitive Chemical Analysis by Raman Spectroscopy. *Chem Rev* 1999; **99**: 2957–2976.

74   Barth A. Infrared spectroscopy of proteins. *Biochim Biophys Acta - Bioenerg* 2007; **1767**: 1073–1101.

75   Chen S, Gao S, Cheng D, Huang J. The characterization and comparison of amyloidogenic segments and non-amyloidogenic segments shed light on amyloid formation. *Biochem Biophys Res Commun* 2014; **447**: 255–262.

76   Perro A, Lebourdon G, Henry S, Lecomte S, Servant L, Marre S. Combining microfluidics and FT-IR spectroscopy: towards spatially resolved information on chemical processes. *React Chem Eng* 2016; **1**: 577–594.

77   Taylor RW, Benz F, Sigle DO, Bowman RW, Bao P, Roth JS *et al.* Watching individual molecules flex

within lipid membranes using SERS. *Sci Rep* 2015; **4**: 5940.

78   Pieczonka NPW, Aroca RF. Inherent Complexities of Trace Detection by Surface-Enhanced Raman Scattering. *ChemPhysChem* 2005; **6**: 2473–2484.

79   Schatz GC, Young MA, Duyne RP. Electromagnetic Mechanism of SERS. In: *Surface-Enhanced Raman Scattering*. Springer Berlin Heidelberg, 2006, pp 19–45.

80   Marquestaut N, Martin A, Talaga D, Servant L, Ravaine S, Reculusa S *et al.* Raman Enhancement of Azobenzene Monolayers on Substrates Prepared by Langmuir–Blodgett Deposition and Electron-Beam Lithography Techniques. *Langmuir* 2008; **24**: 11313–11321.

81   Ćulum NM, Cooper TT, Bell GI, Hess DA, Lagugné-Labarthet F. Characterization of extracellular vesicles derived from mesenchymal stromal cells by surface-enhanced Raman spectroscopy. *Anal Bioanal Chem* 2021. doi:10.1007/s00216-021-03464-8.

82   Tittl A, John-Herpin A, Leitis A, Arvelo ER, Altug H. Metaoberflächen-basierte molekulare Biosensorik unterstützt von künstlicher Intelligenz. *Angew Chemie* 2019; **131**: 14952–14965.

83   Mantsch HH. Biomedical Vibrational Spectroscopy in the Era of Artificial Intelligence. *Molecules* 2021; **26**: 1439.

84   Lussier F, Thibault V, Charron B, Wallace GQ, Masson JF. Deep learning and artificial intelligence methods for Raman and surface-enhanced Raman scattering. *TrAC - Trends Anal Chem* 2020; **124**. doi:10.1016/j.trac.2019.115796.

85   Ayres LB, Gomez FJV, Linton JR, Silva MF, Garcia CD. Taking the leap between analytical chemistry and artificial intelligence: A tutorial review. *Anal Chim Acta* 2021; **1161**: 338403.

86   Morais CLM, Lima KMG, Singh M, Martin FL. Tutorial: multivariate classification for vibrational spectroscopy in biological samples. *Nat Protoc* 2020; **15**: 2143–2162.

87   Yang J, Xu J, Zhang X, Wu C, Lin T, Ying Y. Deep learning for vibrational spectral analysis: Recent progress and a practical guide. *Anal Chim Acta* 2019; **1081**: 6–17.

88   Kajendirarajah U, Olivia Avilés M, Lagugné-Labarthet F. Deciphering tip-enhanced Raman imaging of carbon nanotubes with deep learning neural networks. *Phys Chem Chem Phys* 2020; **22**: 17857–17866.

89   Yang X, Sun Z, Low T, Hu H, Guo X, García de Abajo FJ *et al.* Nanomaterial-Based Plasmon-Enhanced Infrared Spectroscopy. *Adv Mater* 2018; **30**: 1704896.

90   Stuart B. Infrared Spectroscopy. In: *Kirk-Othmer Encyclopedia of Chemical Technology*. John Wiley & Sons, Inc.: Hoboken, NJ, USA, 2015, pp 1–18.

91   Hung K-K, Stege U, Hore DK. IR Absorption, Raman Scattering, and IR-Vis Sum-Frequency Generation Spectroscopy as Quantitative Probes of Surface Structure. *Appl Spectrosc Rev* 2015; **50**: 351–376.

92   Kazarian SG, Chan KLA. Applications of ATR-FTIR spectroscopic imaging to biomedical samples. *Biochim Biophys Acta - Biomembr* 2006; **1758**: 858–867.

93   Lendl B, Frank J, Schindler R, Müller A, Beck M, Faist J. Mid-Infrared Quantum Cascade Lasers for Flow Injection Analysis. *Anal Chem* 2000; **72**: 1645–1648.

94   Khalil M, Demirdöven N, Tokmakoff A. Coherent 2D IR Spectroscopy: Molecular Structure and Dynamics in Solution. *J Phys Chem A* 2003; **107**: 5258–5279.

95   Griffiths PR. Infrared Emission Spectroscopy. I. Basic Considerations. *Appl Spectrosc* 1972; **26**: 73–76.

96   Michaelian KH. *Photoacoustic IR Spectroscopy: Instrumentation, Applications and Data Analysis*.

2010https://books.google.ch/books?hl=en&lr=&id=-WhbmpKUj5YC&oi=fnd&pg=PR11&dq=photoacoustic+infrared+spectroscopy&ots=gahOmI_WlK&sig=2unBAP27mfsld3y3xYAXKMmJ8xw&redir_esc=y#v=onepage&q=photoacoustic   infrared spectroscopy&f=false (accessed 8 Jun2021).

97   Michaelian KH, Frogley MD, Kelley CS, Pedersen T, May TE, Quaroni L *et al.* Micro-photoacoustic infrared spectroscopy. *Infrared Phys Technol* 2018; **93**: 240–246.

98   He Y, Shi J, Pleitez MA, Maslov K, Wagenaar DA, Wang L V. Label-free imaging of lipid-rich biological tissues by mid-infrared photoacoustic microscopy. *J Biomed Opt* 2020; **25**: 1–7.

99   Mayerhöfer TG, Popp J. Beer's law derived from electromagnetic theory. *Spectrochim Acta Part A Mol Biomol Spectrosc* 2019; **215**: 345–347.

100   Neubrech F, Pucci A, Cornelius TW, Karim S, García-Etxarri A, Aizpurua J. Resonant Plasmonic and Vibrational Coupling in a Tailored Nanoantenna for Infrared Detection. *Phys Rev Lett* 2008; **101**: 157403.

101   Pucci A. IR spectroscopy of adsorbates on ultrathin metal films. *Phys status solidi* 2005; **242**: 2704–2713.

102   Berreman DW. Infrared Absorption at Longitudinal Optic Frequency in Cubic Crystal Films. *Phys Rev* 1963; **130**: 2193–2198.

103   Schrettl S, Stefaniu C, Schwieger C, Pasche G, Oveisi E, Fontana Y *et al.* Functional carbon nanosheets prepared from hexayne amphiphile monolayers at room temperature. *Nat Chem* 2014; **6**: 468–476.

104   Adato R, Altug H. In-situ ultra-sensitive infrared absorption spectroscopy of biomolecule interactions in real time with plasmonic nanoantennas. *Nat Commun* 2013; **4**: 2154.

105   Fahrenfort J. Attenuated total reflection. *Spectrochim Acta Part A Mol Spectrosc* 1989; **45**: 251–263.

106   Sergei G. Kazarian, Chan KLA. Micro- and Macro- Attenuated Total Reflection Fourier Transform Infrared Spectroscopic Imaging. *Appl Spectrosc* 2009; **64**: 135A-152A.

107   Neubrech F, Huck C, Weber K, Pucci A, Giessen H. Surface-Enhanced Infrared Spectroscopy Using Resonant Nanoantennas. *Chem Rev* 2017; **117**: 5110–5145.

108   Adato R, Yanik AA, Amsden JJ, Kaplan DL, Omenetto FG, Hong MK *et al.* Ultra-sensitive vibrational spectroscopy of protein monolayers with plasmonic nanoantenna arrays. *Proc Natl Acad Sci* 2009; **106**: 19227–19232.

109   Ataka K, Stripp ST, Heberle J. Surface-enhanced infrared absorption spectroscopy (SEIRAS) to probe monolayers of membrane proteins. *Biochim Biophys Acta - Biomembr* 2013; **1828**: 2283–2293.

110   Maier SA. *Plasmonics: Fundamentals and Applications*. Springer US: New York, NY, 2007 doi:10.1007/0-387-37825-1.

111   Tittl A, Giessen H, Liu N. Plasmonic gas and chemical sensing. *Nanophotonics* 2014; **3**: 157–180.

112   Willets KA, Van Duyne RP. Localized Surface Plasmon Resonance Spectroscopy and Sensing. *Annu Rev Phys Chem* 2007; **58**: 267–297.

113   Estevez M-C, Otte MA, Sepulveda B, Lechuga LM. Trends and challenges of refractometric nanoplasmonic biosensors: A review. *Anal Chim Acta* 2014; **806**: 55–73.

114   Jahn M, Patze S, Hidi IJ, Knipper R, Radu AI, Mühlig A *et al.* Plasmonic nanostructures for surface

enhanced spectroscopic methods. *Analyst* 2016; **141**: 756–793.

115 Novotny L, van Hulst N. Antennas for light. *Nat Photonics* 2011; **5**: 83–90.

116 Lovera A, Gallinet B, Nordlander P, Martin OJF. Mechanisms of Fano Resonances in Coupled Plasmonic Systems. *ACS Nano* 2013; **7**: 4527–4536.

117 Limonov MF, Rybin M V., Poddubny AN, Kivshar YS. Fano resonances in photonics. *Nat Photonics* 2017; **11**: 543–554.

118 Adato R, Artar A, Erramilli S, Altug H. Engineered Absorption Enhancement and Induced Transparency in Coupled Molecular and Plasmonic Resonator Systems. *Nano Lett* 2013; **13**: 2584–2591.

119 Lahiri B, Khokhar AZ, De La Rue RM, McMeekin SG, Johnson NP. Asymmetric split ring resonators for optical sensing of organic materials. *Opt Express* 2009; **17**: 1107.

120 Cetin AE, Etezadi D, Altug H. Accessible Nearfields by Nanoantennas on Nanopedestals for Ultrasensitive Vibrational Spectroscopy. *Adv Opt Mater* 2014; **2**: 866–872.

121 Hicks EM, Zou S, Schatz GC, Spears KG, Van Duyne RP, Gunnarsson L *et al.* Controlling Plasmon Line Shapes through Diffractive Coupling in Linear Arrays of Cylindrical Nanoparticles Fabricated by Electron Beam Lithography. *Nano Lett* 2005; **5**: 1065–1070.

122 Abb M, Wang Y, Papasimakis N, de Groot CH, Muskens OL. Surface-Enhanced Infrared Spectroscopy Using Metal Oxide Plasmonic Antenna Arrays. *Nano Lett* 2014; **14**: 346–352.

123 Giannini V, Vecchi G, Gómez Rivas J. Lighting Up Multipolar Surface Plasmon Polaritons by Collective Resonances in Arrays of Nanoantennas. *Phys Rev Lett* 2010; **105**: 266801.

124 Mayerhöfer TG, Popp J. Periodic array-based substrates for surface-enhanced infrared spectroscopy. *Nanophotonics* 2018; **7**: 39–79.

125 Bagheri S, Weber K, Gissibl T, Weiss T, Neubrech F, Giessen H. Fabrication of Square-Centimeter Plasmonic Nanoantenna Arrays by Femtosecond Direct Laser Writing Lithography: Effects of Collective Excitations on SEIRA Enhancement. *ACS Photonics* 2015; **2**: 779–786.

126 Glaser T, Beck S, Lunkenheimer B, Donhauser D, Köhn A, Kröger M *et al.* Infrared study of the MoO3 doping efficiency in 4,4'-bis(N-carbazolyl)-1,1'-biphenyl (CBP). *Org Electron* 2013; **14**: 575–583.

127 Maß TWW, Taubner T. Incident Angle-Tuning of Infrared Antenna Array Resonances for Molecular Sensing. *ACS Photonics* 2015; **2**: 1498–1504.

128 Chen K, Adato R, Altug H. Dual-Band Perfect Absorber for Multispectral Plasmon-Enhanced Infrared Spectroscopy. *ACS Nano* 2012; **6**: 7998–8006.

129 Chen H. Interference theory of metamaterial perfect absorbers. *Opt Express* 2012; **20**: 7165.

130 Tittl A, Michel A-KU, Schäferling M, Yin X, Gholipour B, Cui L *et al.* A Switchable Mid-Infrared Plasmonic Perfect Absorber with Multispectral Thermal Imaging Capability. *Adv Mater* 2015; **27**: 4597–4603.

131 Tittl A, Mai P, Taubert R, Dregely D, Liu N, Giessen H. Palladium-Based Plasmonic Perfect Absorber in the Visible Wavelength Range and Its Application to Hydrogen Sensing. *Nano Lett* 2011; **11**: 4366–4369.

132 Landy NI, Sajuyigbe S, Mock JJ, Smith DR, Padilla WJ. Perfect Metamaterial Absorber. *Phys Rev Lett* 2008; **100**: 207402.

133 Aouani H, Šípová H, Rahmani M, Navarro-Cia M, Hegnerová K, Homola J *et al.* Ultrasensitive

Broadband Probing of Molecular Vibrational Modes with Multifrequency Optical Antennas. *ACS Nano* 2013; **7**: 669–675.

134   Rodrigo D, Tittl A, John-Herpin A, Limaj O, Altug H. Self-Similar Multiresonant Nanoantenna Arrays for Sensing from Near- to Mid-Infrared. *ACS Photonics* 2018; **5**: 4903–4911.

135   Wallace GQ, Foy HC, Rosendahl SM, Lagugné-Labarthet F. Dendritic Plasmonics for Mid-Infrared Spectroscopy. *J Phys Chem C* 2017; **121**: 9497–9507.

136   Hughes TW, Fan S. Plasmonic Circuit Theory for Multiresonant Light Funneling to a Single Spatial Hot Spot. *Nano Lett* 2016; **16**: 5764–5769.

137   Maksymov IS, Davoyan AR, Miroshnichenko AE, Simovski C, Belov P, Kivshar YS. Multifrequency tapered plasmonic nanoantennas. *Opt Commun* 2012; **285**: 821–824.

138   Urbieta M, Barbry M, Zhang Y, Koval P, Sánchez-Portal D, Zabala N *et al.* Atomic-Scale Lightning Rod Effect in Plasmonic Picocavities: A Classical View to a Quantum Effect. *ACS Nano* 2018; **12**: 585–595.

139   Ermushev A V, Mchedlishvili B V, Oleĭnikov VA, Petukhov A V. Surface enhancement of local optical fields and the lightning-rod effect. *Quantum Electron* 1993; **23**: 435–440.

140   Dodson S, Haggui M, Bachelot R, Plain J, Li S, Xiong Q. Optimizing Electromagnetic Hotspots in Plasmonic Bowtie Nanoantennae. *J Phys Chem Lett* 2013; **4**: 496–501.

141   Huck C, Neubrech F, Vogt J, Toma A, Gerbert D, Katzmann J *et al.* Surface-Enhanced Infrared Spectroscopy Using Nanometer-Sized Gaps. *ACS Nano* 2014; **8**: 4908–4914.

142   Yu N, Cubukcu E, Diehl L, Bour D, Corzine S, Zhu J *et al.* Bowtie plasmonic quantum cascade laser antenna. *Opt Express* 2007; **15**: 13272.

143   Brown L V., Yang X, Zhao K, Zheng BY, Nordlander P, Halas NJ. Fan-Shaped Gold Nanoantennas above Reflective Substrates for Surface-Enhanced Infrared Absorption (SEIRA). *Nano Lett* 2015; **15**: 1272–1280.

144   Yoo D, Mohr DA, Vidal-Codina F, John-Herpin A, Jo M, Kim S *et al.* High-Contrast Infrared Absorption Spectroscopy via Mass-Produced Coaxial Zero-Mode Resonators with Sub-10 nm Gaps. *Nano Lett* 2018; **18**: 1930–1936.

145   Li Y, Simeral ML, Natelson D. Surface-Enhanced Infrared Absorption of Self-Aligned Nanogap Structures. *J Phys Chem C* 2016; **120**: 22558–22564.

146   Chen X, Ciracì C, Smith DR, Oh S-H. Nanogap-Enhanced Infrared Spectroscopy with Template-Stripped Wafer-Scale Arrays of Buried Plasmonic Cavities. *Nano Lett* 2015; **15**: 107–113.

147   Dong L, Yang X, Zhang C, Cerjan B, Zhou L, Tseng ML *et al.* Nanogapped Au Antennas for Ultrasensitive Surface-Enhanced Infrared Absorption Spectroscopy. *Nano Lett* 2017; **17**: 5768–5774.

148   John-Herpin A, Tittl A, Altug H. Quantifying the Limits of Detection of Surface-Enhanced Infrared Spectroscopy with Grating Order-Coupled Nanogap Antennas. *ACS Photonics* 2018; **5**: 4117–4124.

149   Socrates G. *Infrared and Raman characteristic group frequencies: tables and charts*. John Wiley & Sons, 2001.

150   Yang H, Yang S, Kong J, Dong A, Yu S. Obtaining information about protein secondary structures in aqueous solution using Fourier transform IR spectroscopy. *Nat Protoc* 2015; **10**: 382–396.

151   Cai X, Dass C. Conformational Analysis of Proteins and Peptides. *Curr Org Chem* 2003; **7**: 1841–1854.

152   Wu L, Jiang X. Infrared Spectroscopy for Studying Plasma Membranes. In: *Membrane Biophysics*.

Springer: Singapore, 2018, pp 319–354.

153   Baldassarre M, Barth A. Pushing the detection limit of infrared spectroscopy for structural analysis of dilute protein samples. *Analyst* 2014; **139**: 5393–5399.

154   Tabatabaei M, McRae D, Lagugné-Labarthet F. Recent Advances of Plasmon-Enhanced Spectroscopy at Bio-Interfaces. In: *Frontiers of Plasmon Enhanced Spectroscopy Volume 2*. 2016, pp 183–207.

155   Cerjan B, Yang X, Nordlander P, Halas NJ. Asymmetric Aluminum Antennas for Self-Calibrating Surface-Enhanced Infrared Absorption Spectroscopy. *ACS Photonics* 2016; **3**: 354–360.

156   Low T, Chaves A, Caldwell JD, Kumar A, Fang NX, Avouris P *et al.* Polaritons in layered two-dimensional materials. *Nat Mater* 2017; **16**: 182–194.

157   Wu C, Arju N, Kelp G, Fan JA, Dominguez J, Gonzales E *et al.* Spectrally selective chiral silicon metasurfaces based on infrared Fano resonances. *Nat Commun* 2014; **5**: 3892.

158   Tittl A, Leitis A, Liu M, Yesilkoy F, Choi D-Y, Neshev DN *et al.* Imaging-based molecular barcoding with pixelated dielectric metasurfaces. *Science (80-)* 2018; **360**: 1105–1109.

159   Unser S, Bruzas I, He J, Sagle L. Localized Surface Plasmon Resonance Biosensing: Current Challenges and Approaches. *Sensors* 2015; **15**: 15684–15716.

160   Rodrigo D, Tittl A, Ait-Bouziad N, John-Herpin A, Limaj O, Kelly C *et al.* Resolving molecule-specific information in dynamic lipid membrane processes with multi-resonant infrared metasurfaces. *Nat Commun* 2018; **9**: 2160.

161   Le THH, Tanaka T. Plasmonics-Nanofluidics Hybrid Metamaterial: An Ultrasensitive Platform for Infrared Absorption Spectroscopy and Quantitative Measurement of Molecules. *ACS Nano* 2017; **11**: 9780–9788.

162   Etezadi D, Warner JB, Lashuel HA, Altug H. Real-Time In Situ Secondary Structure Analysis of Protein Monolayer with Mid-Infrared Plasmonic Nanoantennas. *ACS Sensors* 2018; **3**: 1109–1117.

163   Morichika I, Kusa F, Takegami A, Sakurai A, Ashihara S. Antenna-Enhanced Nonlinear Infrared Spectroscopy in Reflection Geometry. *J Phys Chem C* 2017; **121**: 11643–11649.

164   Vogt J, Huck C, Neubrech F, Pucci A. Plasmonic Light Scattering and Infrared Vibrational Signal Enhancement. In: *Frontiers of Plasmon Enhanced Spectroscopy Volume 2*. American Chemical Society, 2016, pp 1–19.

165   Ciracì C, Hill RT, Mock JJ, Urzhumov Y, Fernández-Domínguez AI, Maier SA *et al.* Probing the Ultimate Limits of Plasmonic Enhancement. *Science (80-)* 2012; **337**: 1072–1074.

166   Ji D, Cheney A, Zhang N, Song H, Gao J, Zeng X *et al.* Efficient Mid-Infrared Light Confinement within Sub-5-nm Gaps for Extreme Field Enhancement. *Adv Opt Mater* 2017; **5**: 1700223.

167   Hoffmann JM, Janssen H, Chigrin DN, Taubner T. Enhanced infrared spectroscopy using small-gap antennas prepared with two-step evaporation nanosphere lithography. *Opt Express* 2014; **22**: 14425.

168   Yang Z, Kollman JM, Pandi L, Doolittle RF. Crystal structure of native chicken fibrinogen at 2.7 Å Resolution,. *Biochemistry* 2001; **40**: 12515–12523.

169   Diebold-Durand ML, Lee H, Avila LBR, Noh H, Shin HC, Im H *et al.* Structure of full-length SMC and rearrangements required for chromosome organization. *Mol Cell* 2017; **67**: 334–347.

170   Chuang CK, Rockel B, Seyit G, Walian PJ, Schönegge AM, Peters J *et al.* Hybrid molecular structure of the giant protease tripeptidyl peptidase II. *Nat Struct Mol Biol* 2010; **17**: 990–996.

171   Vestergaard B, Groenning M, Roessle M, Kastrup JS, Van De Weert M, Flink JM *et al.* A helical

structural nucleus is the primary elongating unit of insulin amyloid fibrils. *PLoS Biol* 2007; **5**: e134.

172 Liberman V, Adato R, Mertiri A, Yanik AA, Chen K, Jeys TH *et al.* Angle-and polarization-dependent collective excitation of plasmonic nanoarrays for surface enhanced infrared spectroscopy. *Opt Express* 2011; **19**: 11202.

173 Helm CA, Knoll W, Israelachvili JN. Measurement of ligand-receptor interactions. *Proc Natl Acad Sci* 1991; **88**: 8169–8173.

174 Reiter R, Motschmann H, Knoll W. Ellipsometric Characterization of Streptavidin Binding to Biotin-Functionalized Lipid Monolayers at the Water/Air Interface. *Langmuir* 1993; **9**: 2430–2435.

175 Keizer HM, Dorvel BR, Andersson M, Fine D, Price RB, Long JR *et al.* Functional ion channels in tethered bilayer membranes - Implications for biosensors. *ChemBioChem* 2007; **8**: 1246–1250.

176 Wittenberg NJ, Johnson TW, Oh SH. High-density arrays of submicron spherical supported lipid bilayers. *Anal Chem* 2012; **84**: 8207–8213.

177 Jackman JA, Rahim Ferhan A, Cho N-J. Nanoplasmonic sensors for biointerfacial science. *Chem Soc Rev* 2017; **46**: 3615–3660.

178 Lansbury PT, Lashuel HA. A century-old debate on protein aggregation and neurodegeneration enters the clinic. *Nature* 2006; **443**: 774–779.

179 Etezadi D, Warner JB, Ruggeri FS, Dietler G, Lashuel HA, Altug H. Nanoplasmonic mid-infrared biosensor for in vitro protein secondary structure detection. *Light Sci Appl* 2017; **6**: e17029.

180 Meskers S, Ruysschaert JM, Goormaghtigh E. Hydrogen- deuterium exchange of streptavidin and its complex with biotin studied by 2D-attenuated total reflection Fourier transform infrared spectroscopy. *J Am Chem Soc* 1999; **121**: 5115–5122.

181 Nabers A, Ollesch J, Schartner J, Kötting C, Genius J, Hafermann H *et al.* Amyloid-β-Secondary Structure Distribution in Cerebrospinal Fluid and Blood Measured by an Immuno-Infrared-Sensor: A Biomarker Candidate for Alzheimer's Disease. *Anal Chem* 2016; **88**: 2755–2762.

182 Huck C, Toma A, Neubrech F, Chirumamilla M, Vogt J, De Angelis F *et al.* Gold nanoantennas on a pedestal for plasmonic enhancement in the infrared. *ACS Photonics* 2015; **2**: 497–505.

183 Olmon RL, Slovick B, Johnson TW, Shelton D, Oh S-H, Boreman GD *et al.* Optical dielectric function of gold. *Phys Rev B* 2012; **86**: 235147.

184 Rakić AD, Djurišić AB, Elazar JM, Majewski ML. Optical properties of metallic films for vertical-cavity optoelectronic devices. *Appl Opt* 1998; **37**: 5271.

185 Li HH. Refracfive Index of Alkali Halides and Its Wavelength and Temperature Derivatives. *J Phys Chem Ref data* 1976; **5**: 329–528.

186 Rodrigo D, Limaj O, Janner D, Etezadi D, Garcia de Abajo FJ, Pruneri V *et al.* SI: Mid-infrared plasmonic biosensing with graphene. *Science (80-)* 2015; **349**: 165–168.

187 Zawisza I, Lachenwitzer A, Zamlynny V, Horswell SL, Goddard JD, Lipkowski J. Electrochemical and photon polarization modulation infrared reflection absorption spectroscopy study of the electric field driven transformations of a phospholipid bilayer supported at a gold electrode surface. *Biophys J* 2003; **85**: 4055–4075.

188 Fan X, White IM, Shopova SI, Zhu H, Suter JD, Sun Y. Sensitive optical biosensors for unlabeled targets: A review. *Anal Chim Acta* 2008; **620**: 8–26.

189 Freudiger CW, Min W, Saar BG, Lu S, Holtom GR, He C *et al.* Label-Free Biomedical Imaging with High

Sensitivity by Stimulated Raman Scattering Microscopy. *Science (80-)* 2008; **322**: 1857 LP – 1861.

190 Braiman MS, Rothschild KJ. Fourier Transform Infrared Techniques for Probing Membrane Protein Structure. *Annu Rev Biophys Biophys Chem* 1988; **17**: 541–570.

191 Fan M, Andrade GFS, Brolo AG. A review on the fabrication of substrates for surface enhanced Raman spectroscopy and their applications in analytical chemistry. *Anal Chim Acta* 2011; **693**: 7–25.

192 Stuart BH. *Infrared Spectroscopy: Fundamentals and Applications*. John Wiley & Sons, Ltd, 2005.

193 Lashuel HA, Hartley D, Petre BM, Walz T, Lansbury PT. Neurodegenerative disease: Amyloid pores from pathogenic mutations. *Nature* 2002; **418**: 291–291.

194 Mahul-Mellier A-L, Vercruysse F, Maco B, Ait-Bouziad N, De Roo M, Muller D *et al.* Fibril growth and seeding capacity play key roles in α-synuclein-mediated apoptotic cell death. *Cell Death Differ* 2015; **22**: 2107–2122.

195 Settembre C, Fraldi A, Medina DL, Ballabio A. Signals from the lysosome: a control centre for cellular clearance and energy metabolism. *Nat Rev Mol Cell Biol* 2013; **14**: 283–296.

196 Alabi AA, Tsien RW. Synaptic Vesicle Pools and Dynamics. *Cold Spring Harb Perspect Biol* 2012; **4**: a013680–a013680.

197 Cho N-J, Frank CW, Kasemo B, Hook F. Quartz crystal microbalance with dissipation monitoring of supported lipid bilayers on various substrates. *Nat Protoc* 2010; **5**: 1096–1106.

198 Kildishev A V, Boltasseva A, Shalaev VM. Planar Photonics with Metasurfaces. *Science (80-)* 2013; **339**.

199 Zheludev NI, Kivshar YS. From metamaterials to metadevices. *Nat Mater* 2012; **11**: 917–924.

200 Smith DR, Pendry JB, Wiltshire MCK. Metamaterials and Negative Refractive Index. *Science (80-)* 2004; **305**: 788 LP – 792.

201 Yu N, Capasso F. Flat optics with designer metasurfaces. *Nat Mater* 2014; **13**: 139–150.

202 Rodrigo D, Limaj O, Janner D, Etezadi D, Garcia de Abajo FJ, Pruneri V *et al.* Mid-infrared plasmonic biosensing with graphene. *Science (80-)* 2015; **349**: 165–168.

203 Aouani H, Rahmani M, Šípová H, Torres V, Hegnerová K, Beruete M *et al.* Plasmonic Nanoantennas for Multispectral Surface-Enhanced Spectroscopies. *J Phys Chem C* 2013; **117**: 18620–18626.

204 Anker JN, Hall WP, Lyandres O, Shah NC, Zhao J, Van Duyne RP. Biosensing with plasmonic nanosensors. *Nat Mater* 2008; **7**: 442–453.

205 Giannini V, Fernández-Domínguez AI, Heck SC, Maier SA. Plasmonic nanoantennas: Fundamentals and their use in controlling the radiative properties of nanoemitters. *Chem Rev* 2011; **111**: 3888–3912.

206 D'Andrea C, Bochterle J, Toma A, Huck C, Neubrech F, Messina E *et al.* Optical Nanoantennas for Multiband Surface-Enhanced Infrared and Raman Spectroscopy. *ACS Nano* 2013; **7**: 3522–3531.

207 Bantz KC, Meyer AF, Wittenberg NJ, Im H, Kurtulus O, Lee SH *et al.* Recent progress in SERS biosensing. *Phys Chem Chem Phys* 2011; **13**: 11551–11567.

208 Kundu J, Levin CS, Halas NJ. Real-time monitoring of lipid transfer between vesicles and hybrid bilayers on Au nanoshells using surface enhanced Raman scattering (SERS). *Nanoscale* 2009; **1**: 114–117.

209 Ataka K, Heberle J. Biochemical applications of surface-enhanced infrared absorption spectroscopy.

Anal Bioanal Chem 2007; **388**: 47–54.

210   Gottheim S, Zhang H, Govorov AO, Halas NJ. Fractal Nanoparticle Plasmonics: The Cayley Tree. *ACS Nano* 2015; **9**: 3284–3292.

211   Wallace GQ, Tabatabaei M, Hou R, Coady MJ, Norton PR, Simpson TS *et al.* Superimposed Arrays of Nanoprisms for Multispectral Molecular Plasmonics. *ACS Photonics* 2016; **3**: 1723–1732.

212   Aslan E, Aslan E, Wang R, Hong MK, Erramilli S, Turkmen M *et al.* Multispectral Cesaro-Type Fractal Plasmonic Nanoantennas. *ACS Photonics* 2016; **3**: 2102–2111.

213   Hale GM, Querry MR. Optical Constants of Water in the 200-nm to 200-μm Wavelength Region. *Appl Opt* 1973; **12**: 555.

214   Castellana ET, Cremer PS. Solid supported lipid bilayers: From biophysical studies to sensor design. *Surf Sci Rep* 2006; **61**: 429–444.

215   Im H, Wittenberg NJ, Lesuffleur A, Lindquist NC, Oh S-H. Membrane protein biosensing with plasmonic nanopore arrays and pore-spanning lipid membranes. *Chem Sci* 2010; **1**: 688–696.

216   Cremer PS, Boxer SG. Formation and Spreading of Lipid Bilayers on Planar Glass Supports. *J Phys Chem B* 1999; **103**: 2554–2559.

217   Keller CA, Kasemo B. Surface Specific Kinetics of Lipid Vesicle Adsorption Measured with a Quartz Crystal Microbalance. *Biophys J* 1998; **75**: 1397–1402.

218   Pfeiffer I, Petronis S, Köper I, Kasemo B, Zäch M. Vesicle Adsorption and Phospholipid Bilayer Formation on Topographically and Chemically Nanostructured Surfaces. *J Phys Chem B* 2010; **114**: 4623–4631.

219   Smith BC. *Quantitative spectroscopy: theory and practice*. Academic Press, 2003.

220   Dempsey CE. The actions of melittin on membranes. *Biochim Biophys Acta - Rev Biomembr* 1990; **1031**: 143–161.

221   van den Bogaart G, Guzmán JV, Mika JT, Poolman B. On the Mechanism of Pore Formation by Melittin. *J Biol Chem* 2008; **283**: 33854–33857.

222   Moreno M, Giralt E. Three Valuable Peptides from Bee and Wasp Venoms for Therapeutic and Biotechnological Use: Melittin, Apamin and Mastoparan. *Toxins (Basel)* 2015; **7**: 1126–1150.

223   Lee M-T, Sun T-L, Hung W-C, Huang HW. Process of inducing pores in membranes by melittin. *Proc Natl Acad Sci* 2013; **110**: 14243–14248.

224   Singh P. SPR Biosensors: Historical Perspectives and Current Challenges. *Sensors Actuators B Chem* 2016; **229**: 110–130.

225   Watanabe M, Maemura K, Kanbara K, Tamayama T, Hayasaki H. GABA and GABA Receptors in the Central Nervous System and Other Organs. In: *International Review of Cytology*. 2002, pp 1–47.

226   Nair PM, Salaita K, Petit RS, Groves JT. Using patterned supported lipid membranes to investigate the role of receptor organization in intercellular signaling. *Nat Protoc* 2011; **6**: 523–539.

227   Kari OK, Rojalin T, Salmaso S, Barattin M, Jarva H, Meri S *et al.* Multi-parametric surface plasmon resonance platform for studying liposome-serum interactions and protein corona formation. *Drug Deliv Transl Res* 2017; **7**: 228–240.

228   Cho N-J, Wang G, Edvardsson M, Glenn JS, Hook F, Frank CW. Alpha-Helical Peptide-Induced Vesicle Rupture Revealing New Insight into the Vesicle Fusion Process As Monitored in Situ by Quartz Crystal

Microbalance-Dissipation and Reflectometry. *Anal Chem* 2009; **81**: 4752–4761.

229 Attwood S, Choi Y, Leonenko Z. Preparation of DOPC and DPPC Supported Planar Lipid Bilayers for Atomic Force Microscopy and Atomic Force Spectroscopy. *Int J Mol Sci* 2013; **14**: 3514–3539.

230 Hill RT. Plasmonic biosensors. *Wiley Interdiscip Rev Nanomedicine Nanobiotechnology* 2015; **7**: 152–168.

231 Soler M, Huertas CS, Lechuga LM. Label-free plasmonic biosensors for point-of-care diagnostics: a review. *Expert Rev Mol Diagn* 2019; **19**: 71–81.

232 Belushkin A, Yesilkoy F, González-López JJ, Ruiz-Rodríguez JC, Ferrer R, Fàbrega A *et al.* Rapid and Digital Detection of Inflammatory Biomarkers Enabled by a Novel Portable Nanoplasmonic Imager. *Small* 2020; **16**: 1906108.

233 Justino C, Duarte A, Rocha-Santos T. Recent Progress in Biosensors for Environmental Monitoring: A Review. *Sensors* 2017; **17**: 2918.

234 Masson J-F. Portable and field-deployed surface plasmon resonance and plasmonic sensors. *Analyst* 2020; **145**: 3776–3800.

235 Polman A. Plasmonics Applied. *Science (80-)* 2008; **322**: 868–869.

236 Couture M, Zhao SS, Masson J-F. Modern surface plasmon resonance for bioanalytics and biophysics. *Phys Chem Chem Phys* 2013; **15**: 11190.

237 Patching SG. Surface plasmon resonance spectroscopy for characterisation of membrane protein–ligand interactions and its potential for drug discovery. *Biochim Biophys Acta - Biomembr* 2014; **1838**: 43–55.

238 Kneipp K, Wang Y, Kneipp H, Perelman LT, Itzkan I, Dasari RR *et al.* Single Molecule Detection Using Surface-Enhanced Raman Scattering (SERS). *Phys Rev Lett* 1997; **78**: 1667.

239 Chen K, Dao TD, Ishii S, Aono M, Nagao T. Infrared Aluminum Metamaterial Perfect Absorbers for Plasmon-Enhanced Infrared Spectroscopy. *Adv Funct Mater* 2015; **25**: 6637–6643.

240 Ye M, Crozier KB. Metasurface with metallic nanoantennas and graphene nanoslits for sensing of protein monolayers and sub-monolayers. *Opt Express* 2020; **28**: 18479.

241 Pfitzner E, Seki H, Schlesinger R, Ataka K, Heberle J. Disc Antenna Enhanced Infrared Spectroscopy: From Self-Assembled Monolayers to Membrane Proteins. *ACS Sensors* 2018; **3**: 984–991.

242 Semenyshyn R, Mörz F, Steinle T, Ubl M, Hentschel M, Neubrech F *et al.* Pushing Down the Limit: In Vitro Detection of a Polypeptide Monolayer on a Single Infrared Resonant Nanoantenna. *ACS Photonics* 2019; **6**: 2636–2642.

243 Wallace GQ, McRae DM, Lagugné-Labarthet F. Probing mid-infrared plasmon resonances in extended radial fractal structures. *Opt Lett* 2019; **44**: 3865.

244 Roubaud G, Bondareff P, Volpe G, Gigan S, Bidault S, Grésillon S. Far-Field Wavefront Control of Nonlinear Luminescence in Disordered Gold Metasurfaces. *Nano Lett* 2020; **20**: 3291–3298.

245 Wiercigroch E, Szafraniec E, Czamara K, Pacia MZ, Majzner K, Kochan K *et al.* Raman and infrared spectroscopy of carbohydrates: A review. *Spectrochim Acta Part A Mol Biomol Spectrosc* 2017; **185**: 317–335.

246 Weber K, Nesterov ML, Weiss T, Scherer M, Hentschel M, Vogt J *et al.* Wavelength Scaling in Antenna-Enhanced Infrared Spectroscopy: Toward the Far-IR and THz Region. *ACS Photonics* 2017; **4**: 45–51.

247 Cao C, Liu F, Tan H, Song D, Shu W, Li W *et al.* Deep Learning and Its Applications in Biomedicine.

Genomics Proteomics Bioinformatics 2018; **16**: 17–32.

248   Ballard ZS, Joung H-A, Goncharov A, Liang J, Nugroho K, Di Carlo D *et al.* Deep learning-enabled point-of-care sensing using multiplexed paper-based sensors. *npj Digit Med* 2020; **3**: 66.

249   Bigdeli S, Honzátko D, Süsstrunk S, Dunbar LA. Image Restoration using Plug-and-Play CNN MAP Denoisers. *arXiv Prepr arXiv191209299* 2019. doi:10.5220/0008990700850092.

250   Knights-Mitchell SS, Romanowski M. Near-Infrared Activated Release of Doxorubicin from Plasmon Resonant Liposomes. *Nanotheranostics* 2018; **2**: 295–305.

251   Rostamabadi H, Falsafi SR, Jafari SM. Nanoencapsulation of carotenoids within lipid-based nanocarriers. *J Control Release* 2019; **298**: 38–67.

252   Pardoux É, Roux A, Mathey R, Boturyn D, Roupioz Y. Antimicrobial peptide arrays for wide spectrum sensing of pathogenic bacteria. *Talanta* 2019; **203**: 322–327.

253   Pardoux É, Boturyn D, Roupioz Y. Antimicrobial Peptides as Probes in Biosensors Detecting Whole Bacteria: A Review. *Molecules* 2020; **25**: 1998.

254   Avella-Oliver M, Puchades R, Wachsmann-Hogiu S, Maquieira A. Label-free SERS analysis of proteins and exosomes with large-scale substrates from recordable compact disks. *Sensors Actuators B Chem* 2017; **252**: 657–662.

255   Zhu S, Li H, Yang M, Pang SW. Highly sensitive detection of exosomes by 3D plasmonic photonic crystal biosensor. *Nanoscale* 2018; **10**: 19927–19936.

256   Swank Z, Laohakunakorn N, Maerkl SJ. Cell-free gene-regulatory network engineering with synthetic transcription factors. *Proc Natl Acad Sci* 2019; **116**: 5892–5901.

257   Goedert M, Jakes R, Spillantini MG, Hasegawa M, Smith MJ, Crowther RA. Assembly of microtubule-associated protein tau into Alzheimer-like filaments induced by sulphated glycosaminoglycans. *Proc Natl Acad Sci USA* 1996; **383**: 550–553.

258   Wang Y, Mandelkow E. Tau in physiology and pathology. *Nat Rev Neurosci* 2015; **17**: 22–35.

259   Tittl A, John-Herpin A, Leitis A, Arvelo ER, Altug H. Metasurface-Based Molecular Biosensing Aided by Artificial Intelligence. *Angew Chemie Int Ed* 2019; **58**: 14810–14822.

260   Aksu S, Yanik AA, Adato R, Artar A, Huang M, Altug H. High-Throughput Nanofabrication of Infrared Plasmonic Nanoantenna Arrays for Vibrational Nanospectroscopy. *Nano Lett* 2010; **10**: 2511–2518.

261   Ding Z, Stubbs JM, McRae D, Blacquiere JM, Lagugné-Labarthet F, Mittler S. A Mass-Producible and Versatile Sensing System: Localized Surface Plasmon Resonance Excited by Individual Waveguide Modes. *ACS Sensors* 2018; **3**: 334–341.

262   Bahk Y-M, Kim D-S, Park H-R. Large-Area Metal Gaps and Their Optical Applications. *Adv Opt Mater* 2019; **7**: 1800426.

263   Chen C, Mohr DA, Choi H-K, Yoo D, Li M, Oh S-H. Waveguide-Integrated Compact Plasmonic Resonators for On-Chip Mid-Infrared Laser Spectroscopy. *Nano Lett* 2018; **18**: 7601–7608.

264   Leitis A, Tittl A, Liu M, Lee BH, Gu MB, Kivshar YS *et al.* Angle-multiplexed all-dielectric metasurfaces for broadband molecular fingerprint retrieval. *Sci Adv* 2019; **5**: eaaw2871.

265   Cerjan B, Halas NJ. Toward a Nanophotonic Nose: A Compressive Sensing-Enhanced, Optoelectronic Mid-Infrared Spectrometer. *ACS Photonics* 2019; **6**: 79–86.

266   Knight MW, Liu L, Wang Y, Brown L, Mukherjee S, King NS *et al.* Aluminum Plasmonic Nanoantennas.

Nano Lett 2012; **12**: 6000–6004.

267   Tütüncü E, Mizaikoff B. Cascade laser sensing concepts for advanced breath diagnostics. *Anal Bioanal Chem* 2019; **411**: 1679–1686.

268   Akhgar CK, Ramer G, Żbik M, Trajnerowicz A, Pawluczyk J, Schwaighofer A *et al.* The Next Generation of IR Spectroscopy: EC-QCL-Based Mid-IR Transmission Spectroscopy of Proteins with Balanced Detection. *Anal Chem* 2020; **92**: 9901–9907.

269   Eilers P, Report HB-LUMC, 2005 U. Baseline correction with asymmetric least squares smoothing. *Leiden Univ Med Cent Rep* 2005; **1**: 5.

270   Kingma DP, Ba J. Adam: A Method for Stochastic Optimization. *arXiv Prepr arXiv14126980* 2014.http://arxiv.org/abs/1412.6980.

271   Bareza NJ, Gopalan KK, Alani R, Paulillo B, Pruneri V. Mid-infrared Gas Sensing Using Graphene Plasmons Tuned by Reversible Chemical Doping. *ACS Photonics* 2020; **7**: 879–884.

272   Kelp G, Li J, Lu J, DiNapoli N, Delgado R, Liu C *et al.* Infrared spectroscopy of live cells from a flowing solution using electrically-biased plasmonic metasurfaces. *Lab Chip* 2020; **20**: 2136–2153.

273   Oh S, Altug H, Jin X, Low T, Koester SJ, Ivanov AP *et al.* Nanophotonic biosensors harnessing van der Waals materials. *Nat Commun* 2021; **12**: 3824.

274   Gérard D, Gray SK. Aluminium plasmonics. *J Phys D Appl Phys* 2015; **48**: 184001.

275   Raja SS, Cheng C-W, Sang Y, Chen C-A, Zhang X-Q, Dubey A *et al.* Epitaxial Aluminum Surface-Enhanced Raman Spectroscopy Substrates for Large-Scale 2D Material Characterization. *ACS Nano* 2020; **14**: 8838–8845.

276   Tseng ML, Jahani Y, Leitis A, Altug H. Dielectric Metasurfaces Enabling Advanced Optical Biosensors. *ACS Photonics* 2021; **8**: 47–60.

277   Mizaikoff B. Waveguide-enhanced mid-infrared chem/bio sensors. *Chem Soc Rev* 2013; **42**: 8683.

278   Schwaighofer A, Brandstetter M, Lendl B. Quantum cascade lasers (QCLs) in biomedical spectroscopy. *Chem Soc Rev* 2017; **46**: 5903–5924.

279   Lins E, Read S, Unni B, Rosendahl SM, Burgess IJ. Microsecond Resolved Infrared Spectroelectrochemistry Using Dual Frequency Comb IR Lasers. *Anal Chem* 2020; **92**: 6241–6244.

280   Sterczewski LA, Westberg J, Yang Y, Burghoff D, Reno J, Hu Q *et al.* Terahertz hyperspectral imaging with dual chip-scale combs. *Optica* 2019; **6**: 766.

AURELIAN JOHN-HERPIN

I am a scientist and engineer with a rich interdisciplinary background ranging from physics and programming to biosensors and data science. My passion and curiosity impart me with a strong drive for exploration and perseverance to deliver solutions. My zeal for continuous learning gives me joy and confidence that I can be an asset to any science and engineering team.
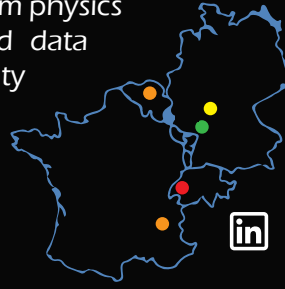
Lavaux, Swiss residence permit C

✉ aurelian@john-herpin.com

in linkedin.com/in/aurelian-john-herpin

🎓 EDUCATION

2016 — 2021   **Ph.D., Photonics**   *Lausanne, Switzerland*
École Polytechnique Fédérale de Lausanne (EPFL)

2014 — 2016   **M.S., Nanoscience**   *Leuven, Belgium*
KU Leuven, *Summa cum laude*

2009 — 2014   **B.S., Physics**   *Karlsruhe, Germany*
Karlsruhe Institute of Technology (KIT)

1996 — 2009   **AbiBac, Scientific**   *Frankfurt, Germany*
Lycée Français Victor Hugo, *French & German Diploma*

🗪 LANGUAGES

Proficiency (C, B, A)
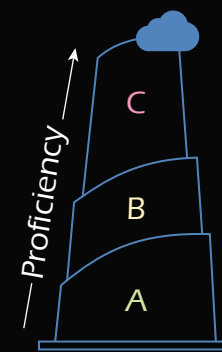
- English
- French
- German
- Spanish
- Dutch
- Japanese

💼 WORK EXPERIENCE

2016 — 2021   **Ph.D. thesis & safety coordinator**   *Institute of Bioengineering, EPFL, Switzerland*
"IR nanoplasmonic metasurfaces augmented by artificial intelligence for universal biosensing"
- Data preparation, machine / deep learning modeling (Matlab, R, Python, Pandas, Keras)
- Real-time, spectrotemporal data collection using optofluidics and macro coding (OPUS)
- Electromagnetic computer simulations of nanoplasmonic antennas (CST, VBA scripts)
- Cleanroom fabrication of plasmonic, photonic and microfluidic micro-/nanochips
- Spectroscopy, fluorescence microscopy, chemical functionalization, biological sample preparation
- Communication & managing experience in teaching and laboratory safety coordination

2015 — 2016   **M.S. thesis**   *French Alternative Energies and Atomic Energy Commission, France*
"Multiplexed Optoelectronic Nose: From Chemistry to Multivariate Statistics"
- Automating data preparation and transformation using VBA programing (Excel)
- Data visualization with R & ggplot2 — principal component & hierachical clustering analysis (PCA, HCA)
- Real-time data collection with surface plasmon resonance imaging of volatile organic compounds
- Chemical functionalization of sensor chip surfaces

2015 — 2016   **Summer internship**   *French Alternative Energies and Atomic Energy Commission, France*
Development of an optoelectronic tongue for sensing bacteria
- Automating data preparation using VBA programing (Excel)
- Real-time data collection with surface plasmon resonance imaging of bacteria

2013 — 2014   **Service jobs**   *Arts center, Offenbach & Airport, Frankfurt*
Experience working and communicating with people in enterprise environments

2012 — 2013   **B.S. thesis**   *Institute of Nanotechnology, KIT, Germany*
"Computer Simulation and Experiments for the Wetting of Hydrophobic Structures"
- Programing physics simulations based on gradient descent (Surface Evolver)
- Experimental physics and analytical calculations for studying biomimetic surfaces

STRENGTHS & SKILLS

- Creativity, perseverance, critical thinking
  - Established experimental and data analysis methods in lab
- Oral, visual and written communication
  - Presentations at several renowned international conferences
  - Science communication to the public via written news stories and engaging visuals as well as TV interviews
- Curiosity, continuous learning
  - Followed countless extracurricalar courses covering diverse subject fields including music, data science, robotics, astronomy, blockchain, neuroscience, languages
- Creation of quality visuals
  - Won several photo competitions (Photography, Adobe Lightroom, Photoshop, Illustrator)
  - Designer & photographer for EPFL's doctoral school of photonics
  - Represented brands on social media (Adobe Premiere Pro, After Effects)
  - Awarded several journal covers (Blender modeling and rendering)

- Teamwork, responsibility, leadership
  - Collaborated on several scientific projects and publications both as first and co-author in multicultural and international environments
  - Successful laboratory safety management
- Teaching
  - Supervised several bachelor and master students
  - Lectured in front of hundreds of master students
  - Set up laboratory practicals and created exams

LANGUAGES

Proficiency
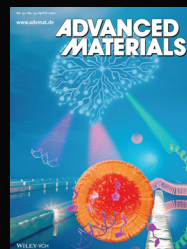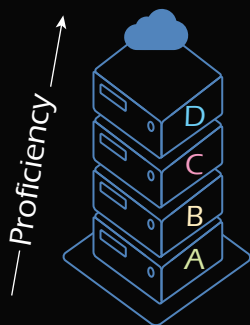
- Python (Pandas, Keras, PyTorch, etc.)
- R, SQL (IBM cloud)
- Matlab, VBA
- HTML, CSS
- ImageJ, Labview
- C++, Surface Evolver
- Mathematica, Root

PUBLICATIONS

- Advanced Materials, invited review, submission November 2021.
- Advanced Materials, 2021, 33, 2006054.
- Advanced Materials, 2021, 33, 2102232.
- Angewandte Chemie Int. Ed., 2019, 58, 14810.
- Angewandte Chemie, 2019, 131, 14952.
- ACS Photonics, 2018, 5, 4117.
- ACS Photonics, 2018, 5, 4903.
- Analytical Chemistry, 2018, 90, 9879.
- Nature Communications, 2018, 9, 2160.
- Nano Letters, 2018, 18, 1930.
- ACS Sensors, 2018, 3, 2286.
- Int. Symp. Olfaction Electron. Nose, IEEE, 2017.
- Conf. Lasers Electro-Optics, OSA, 2018.
- Conf. Lasers Electro-Optics Eur. Quantum Electron. Conf., IEEE, 2021.

CONFERENCE TALKS

- 11th International Conference on Advanced Vibrational Spectroscopy (ICAVS 11)
- CLEO/Europe-EQEC 2021
- 31st Anniversary World Congress on Biosensors
- Photonics North 2021
- 9th International Conference on Surface Plasmon Photonics in Copenhagen (SPP9)
- 45th International Conference on Micro & Nano Engineering (MNE45)
- EPFL Photonics Day 2018

AWARDS & HONORS

- 2021 — EPS-QEOD Award
  - Swiss TV interview, La Télé
  - Journal cover images, Adv. Materials
- 2019 — Carlsberg Foundation Scholarship
- 2018 — Journal cover image, ACS Photonics
  - Journal cover image, ACS Sensors
- 2015 — Predoc program scholarship, LANEF
- 2014 — Erasmus+ scholarship, EU Commission

HOBBIES